

# EXPERIMENTAL AND NUMERICAL STUDY OF RC BEAMS STRENGTHENED IN FLEXURE WITH BOLTED/BONDED AA PLATES

by

Omar Raed Abuodeh

A Thesis Presented to the Faculty of the  
American University of Sharjah  
College of Engineering  
in Partial Fulfillment  
of the Requirements  
for the Degree of  
Master of Science in  
Civil Engineering  
Sharjah, United Arab Emirates  
April 2019

©c 2019 Omar Raed Abuodeh. All rights reserved.

Approval Signatures

We, the undersigned, approve the Master's Thesis of Omar Raed Abuodeh.

Thesis Title: Experimental and Numerical Study of RC Beams Strengthened  
in  
Flexure with Bolted/Bonded AA Plates

Signature                      Date of Signature  
(dd/mm/yyyy)

\_\_\_\_\_  
Dr. Jamal A. Abdalla  
Professor, Department of Civil Engineering  
Thesis Advisor

\_\_\_\_\_  
Dr. Rami Haweeleh  
Professor, Department of Civil Engineering  
Thesis Co-Advisor

\_\_\_\_\_  
Dr. Farid Abed  
Professor, Department of Civil Engineering  
Thesis Committee Member

\_\_\_\_\_  
Dr. Wael Abuzaid  
Assistant Professor, Department of Mechanical Engineering

Thesis Committee Member

---

Dr. Irtishad U. Ahmad  
Head, Department of Civil Engineering

---

Dr. Lotfi Romdhane  
Associate Dean for Graduate Affairs and Research  
College of Engineering

---

Dr. Naif Darwish  
Acting Dean, College of Engineering

---

Dr. Mohamed El-Tarhuni  
Vice Provost for Graduate Studies  
Acknowledgement

I would like to express my sincere gratitude to my supervisors, Dr. Jamal A.

Abdalla and Dr. Rami Hawileh, for their continuous support during my M.Sc. degree

in the American University of Sharjah. Many thanks as well to the College of Engi-

neering, Department of Civil Engineering at AUS for providing me with the teaching

assistantship throughout my graduate studies. I would also like to thank my family and

friends who encouraged me and supported me during my graduate career.

Finally, I

would like to thank Engineer Ansari and Engineer Arshi Faridi for their assistance and

guidance during the experiment.

Abstract

Reinforced Concrete (RC) members are susceptible to deterioration due to many fac-

tors. Externally bonded reinforcement (EBR) such as fiber-reinforced polymers (FRP),

had emerged as one of the proven techniques for flexural strengthening and retrofitting

of RC members. This is due to its practicality and structural effectiveness; however

there are shortcomings that include premature de-bonding/de-lamination failure or brit-

tle FRP rupture failures. The use of mechanically anchored Aluminum Alloy (AA)

plates instead has the potential of overcoming these drawbacks by providing both strength

and ductility while influencing the failure modes. In this project, 16 RC beams were

prepared, one beam was left unstrengthened (CB), one was strengthened with AA plate

using epoxy only (CBE), and 14 beams were strengthened with AA plates with different bolt sizes, spacing, bolt layout and epoxy. The specimens were tested to failure and all specimens with bolted AA plates exhibited approximately 30% increase in strength accompanied with drastic increase in ultimate ductility (56.5%) and failure ductility (84.1%) compared to the control beam with epoxy (CBE). It is concluded that the implementation of a hybrid anchorage system (i.e., bolts with epoxy) in retrofitting applications serves as a viable option for fixing AA plates to RC beams. Furthermore, nonlinear finite element (FE) models for all specimens were developed using validated constitutive laws for capturing the nonlinear properties of the materials. Contour plots and concrete cracking patterns were generated to monitor the stress and cracking propagation for each model. The FE predictions closely resemble that of the experimental results in terms of load-deflection, cracks patterns and failure modes. This validated the use of FE as a simulation tool for further investigating the behavior of RC beams strengthened with externally bonded and bolted AA plates.

Keywords: Aluminum Alloy plates; Mechanical fasteners; Finite element modelling.

5

Table of Contents

Abstract  
..... 5

List of Figures  
..... 9

List of Tables  
..... 13

List of Abbreviations  
..... 14

Chapter 1.  
Introduction..... 15

1.1. Overview  
..... 15

1.2. Problem Statement  
..... 18

1.3. Research Significance	
.....	
.....	18
1.4. Research Objectives	
.....	
.....	19
1.5. Thesis Organization	
.....	
.....	19
Chapter 2. Literature	
Review.....	
.....	22
2.1. Flexural	
Strengthening.....	
.....	22
2.1.1. Steel	
plates.....	
.....	22
2.1.2. FRP	
plates.....	
.....	24
2.1.3. FRP sheets	
.....	
.....	26
2.1.4. Aluminum alloy plates	
.....	26
2.2. Anchorage Techniques	
.....	
.....	27
2.2.1. U-wrap anchorage	
.....	
.....	27
2.2.2. Bolts and mechanical fasteners	
.....	28
2.3. Finite Element	
Simulations.....	
.....	30
Chapter 3. Experimental Program	
.....	
.....	31
3.1. RC Beam	
Details.....	
.....	31
3.1.1. Geometry and	
design.....	
.....	31
3.1.2. Specimen instrumentation	
.....	33
3.1.3. RC specimen preparation	
.....	34
3.2. Material Specification	
.....	
.....	35

3.2.1. Concrete compression test	36
3.2.2. Tensile testing of normal strength reinforcing bars	36
3.2.2.1. Mechanical properties of $\phi 8$ mm bar	36
3.2.2.2. Mechanical properties of $\phi 10$ mm bar	39
3.2.3. Tensile testing for AA plates	40
3.2.4. Mechanical fasteners	40
3.2.5. Epoxy	43
3.3. External Strengthening	44
3.3.1. Surface preparation	44
3.3.1.1. Surface preparation for AA plates	44
3.3.1.2. Surface preparation for concrete specimens	45
3.3.2. Mechanical fastening strategy	45
3.3.3. Setting instructions for HST3 bolts	46
3.3.4. Final specimens	47
Chapter 4. Results and Discussions	50
4.1. Response and Behaviour of Each Specimen	50
4.1.1. CB-Specimens	51
4.1.1.1. CB	51
4.1.1.2. CBE	51
4.1.2. M10-Specimens	52
4.1.2.1. BEM10L	53

4.1.2.2. BEM10H	
.....	
54	
4.1.2.3.	
BM10H.....	
.....	56
4.1.2.4.	
BEM10E.....	
.....	57
4.1.3. M12-	
Specimens.....	
.....	59
4.1.3.1.	
BEM12L.....	
.....	60
4.1.3.2. BEM12H	
.....	
61	
4.1.3.3.	
BM12H.....	
.....	62
4.1.3.4.	
BEM12E.....	
.....	64
4.2. Summary of Results and Remarks	
.....	65
4.2.1. Effect of M10 bolts with/without bonding	
.....	67
4.2.2. Effect of M12 bolts with/without bonding	
.....	71
4.2.3. Effect of different bolt models at low-uniform spacing with bonding	
.....	
.....	73
4.2.4. Effect of different bolt models at high-uniform spacing with bonding	
.....	
.....	75
4.2.5. Effect of different bolt models at high-uniform spacing without bonding	
.....	
.....	78
4.2.6. Effect of different bolt models at the beams' ends with bonding...	
81	
4.3. Failure Modes	
.....	
.....	82
7	
4.3.1. CB-Specimens	
.....	
.....	83
4.3.2. M10-	
Specimens.....	
.....	84

4.3.3. M12-Specimens.....	84
4.4. Ductility Index.....	86
Chapter 5. Nonlinear Finite Element Modelling.....	92
5.1. Geometry of FE Models.....	92
5.2. Element Types and Material Properties.....	92
5.2.1. SOLID65.....	93
5.2.2. LINK180.....	95
5.2.3. SOLID185.....	96
5.2.4. INTER205.....	97
5.2.5. TARGE170 and CONTA174.....	100
5.3. Convergence Criterion.....	101
5.4. Failure Criteria.....	102
5.5. Modelling Techniques.....	102
5.6. Load Versus Deflection Curves.....	105
5.6.1. CB-Specimens.....	108
5.6.2. M10-Specimens.....	108
5.6.3. M12-Specimens.....	109
5.6.4. Summary of results.....	109
5.7. Predicted Contour Plots and Cracking Patterns.....	110

5.7.1.	
CB.....	112
5.7.2.	
BM10H.....	113
5.7.3.	
BEM12E.....	115
5.7.4. Summary of	
results.....	118
Chapter 6. Conclusion	
.....	120
References.....	122
Appendix A: Predicted Nodal Vertical Deflection Plots for FE Models	
.....	128
Appendix B: Predicted Nodal First Principal Stress Plots for FE Models	
.....	133
Appendix C: Predicted Nodal Shear Stress Plots in Bolts.....	138
Appendix D: Predicted Nodal Third Principal Strain for FE Models.....	142
Appendix E: Predicted Crack Pattern for FE Models	
.....	146
Vita.....	149
8	
List of Figures	
Figure 1-1: Debonding failure modes [23].	
.....	17
Figure 1-2: Stress versus strain curve for strengthening materials [20].....	17
Figure 2-3: Load versus deflection curves of steel plated specimens [45].	
.....	23
Figure 2-4: Externally strengthened continuous RC beam [48].	
.....	25
Figure 2-5: Failure mode of splay anchor in [66].	
.....	29
Figure 3-6: Beam geometry	
.....	32
Figure 3-7: Geometry and details of CB-Specimens.	
.....	32
Figure 3-8: Geometry and details of M10-Specimens.	
.....	33
Figure 3-9: Geometry and details of M12-Specimens.	
.....	34
Figure 3-10: Strain gage locations.	
.....	35



Figure 3-11: RC beam specimen preparation.	35
Figure 3-12: Concrete cube tests and preparations.	37
Figure 3-13: Offset Method [77].	37
Figure 3-14: Dimensions of a steel reinforcing $\phi 8$ mm bar in a tensile test.	38
Figure 3-15: Steel tensile test $\phi 8$ mm.	38
Figure 3-16: Stress versus strain curve for each $\phi 8$ mm bar.	38
Figure 3-17: Dimensions of a steel reinforcing $\phi 10$ mm bar in a tensile test.	39
Figure 3-18: Steel tensile test for $\phi 10$ mm.	39
Figure 3-19: Stress versus strain curve for each $\phi 10$ mm bar.	40
Figure 3-20: Dimensions of a dog-bone shaped AA plate [78].	41
Figure 3-21: AA plate tensile test.	41
Figure 3-22: Stress versus strain curve for each AA coupon.	41
Figure 3-23: Diagram depicting HST3 expansion anchors' geometric limitations in concrete.	42
Figure 3-24: Hilti expansion anchor models.	43
Figure 3-25: Two-component epoxy.	43
Figure 3-26: Default and smoothed surface of AA plates.	44
Figure 3-27: Surface preparation of RC beams.	45
Figure 3-28: Bolt location markings on AA plates.	46
Figure 3-29: Bolt location markings on concrete specimens.	46
Figure 3-30: Bolt embedment depth for each model.	47
Figure 3-31: Setting instruction for HST3 expansion anchors [79].	47
Figure 3-32: Final strengthened specimens.	48
Figure 3-33: Loading scheme of specimens.	49
Figure 4-34: Load, deflection and strain for CB at mid-span.	52

Figure 4-35: Load, deflection and strain for CBE at mid-span. .....	53
Figure 4-36: Load, deflection and strain for BEM10L specimens at mid-span. ....	55
Figure 4-37: Load, deflection and strain for BEM10H specimens at mid-span. ....	56
Figure 4-38: Load, deflection and strain of BM10H specimens at mid-span. .....	58
Figure 4-39: Load, deflection and strain for BEM10E at mid-span.....	59
Figure 4-40: Load, deflection and strain of BEM12L specimens at mid-span. .....	61
Figure 4-41: Load, deflection and strain of BEM12H specimens at mid-span.....	63
Figure 4-42: Load, deflection and strain of BM12H specimens at mid-span. .....	65
Figure 4-43: Load, deflection and strain of BEM12E specimen at mid-span.....	66
9	
Figure 4-44: Load versus deflection curves of CB compared to M10-Specimens. .	70
Figure 4-45: Bar plot of load comparisons for the M10-Specimens group. .....	71
Figure 4-46: Load versus deflection curves of CB compared to M12-Specimens. .	73
Figure 4-47: Bar plot of load comparisons for the M12-Specimens group. .....	74
Figure 4-48: Load versus deflection curves for different bolt models at low-uniform spacing.....	75
Figure 4-49: Bar plot of load comparisons. .....	76
Figure 4-50: Load versus deflection curves for different bolt models at high-uniform spacing.....	77
Figure 4-51: Bar plot of load comparisons. .....	78
Figure 4-52: Load versus deflection curves for different bolt models at low-uniform spacing without bonding. .....	80
Figure 4-53: Bar plot of load comparisons for BM10H and BM12H.....	80
Figure 4-54: Load versus deflection curves for different bolt models at edge of beams.....	82
Figure 4-55: Bar plot of load comparisons. .....	83

Figure 4-56: Failure modes of CB-Specimens.....	83
Figure 4-57: Failure modes of BM10H specimens. .....	85
Figure 4-58: Failure modes of BEM10H specimens.....	86
Figure 4-59: Failure modes of BEM10L specimens. .....	87
Figure 4-60: Failure modes of BEM10E.....	87
Figure 4-61: Failure modes of BM12H specimens. .....	88
Figure 4-62: Failure modes of BEM12H specimens.....	89
Figure 4-63: Failure modes of BEM12L specimens. .....	90
Figure 4-64: Failure modes of BEM12E.....	90
Figure 4-65: Bar plot of ductility index for M10-Specimens group. .....	91
Figure 4-66: Bar plot of ductility index for M12-Specimens group .....	91
Figure 5-67: Quarter model of RC beam .....	92
Figure 5-68: Geometry of SOLID65 element [41]. .....	93
Figure 5-69: Idealized stress-strain curves for concrete. .....	95
Figure 5-70: Geometry of LINK180 element [41].....	96
Figure 5-71: ElasticPerfectly plastic stress-strain curve .....	97
Figure 5-72: Geometry of SOLID185 element [41]. .....	98
Figure 5-73: Idealized tensile stress-strain curves. .....	98
Figure 5-74: Geometry of INTER205 element [41]. .....	99
Figure 5-75: Bond stress-slip model at the interface between the aluminum and concrete elements. .....	100
Figure 5-76: TARGE170 and CONTA174 surfaces [41]. .....	101
Figure 5-77: FE meshed geometry of CB specimen. .....	103
Figure 5-78: FE meshed geometry of steel reinforcement.....	103
Figure 5-79: Top and bottom meshed layers of epoxy. .....	104

Figure 5-80: AA Plate Meshed Elements.	105
Figure 5-81: Bolt elements shapes for a strengthened specimen with high number of bolts.	106
Figure 5-82: CONTA174 and TARGE170 element assignments.	106
Figure 5-83: Epoxy and Bolt modelling for Plated Specimens.	107
Figure 5-84: Load versus deflection curves between experimental and FE results for CB-Specimens.	109
Figure 5-85: Load versus deflection curves between experimental and FE results for M10-Specimens.	110
Figure 5-86: Load versus deflection curves between experimental and FE results for M12-Specimens.	111
Figure 5-87: Predicted nodal vertical deflection for CB model.	113
Figure 5-88: Predicted nodal third principal strain for CB model.	113
Figure 5-89: Predicted crack patterns of the CB model.	113
Figure 5-90: Predicted nodal vertical deflection for BM10H model.	114
Figure 5-91: Predicted nodal first principal stress for BM10H model.	114
Figure 5-92: Predicted nodal shear stress for BM10H model.	115
Figure 5-93: Predicted nodal third principal strain for BM10H model.	116
Figure 5-94: Predicted crack patterns of the BM10H model.	116
Figure 5-95: Predicted nodal vertical deflection for BEM12E model.	117
Figure 5-96: Predicted nodal first principal stress for BEM12E model.	117
Figure 5-97: Predicted nodal shear stress for BEM12E model.	118
Figure 5-98: Predicted nodal third principal strain for BEM12E model.	118
Figure 5-99: Predicted crack patterns of the BEM12E model.	118

Figure 6-100: Predicted nodal vertical deflection for CB model. .....	128
Figure 6-101: Nodal vertical deflection and debonding action for CBE model. ....	128
Figure 6-102: Predicted nodal vertical deflection for BEM10H model. .....	129
Figure 6-103: Predicted nodal vertical deflection for BEM10L model. .....	129
Figure 6-104: Predicted nodal vertical deflection for BM10H model. .....	129
Figure 6-105: Predicted nodal vertical deflection for BEM10E model. .....	130
Figure 6-106: Predicted nodal vertical deflection for BEM12H model. .....	130
Figure 6-107: Predicted nodal vertical deflection for BEM12L model. .....	131
Figure 6-108: Predicted nodal vertical deflection for BM12H model. .....	131
Figure 6-109: Predicted nodal vertical deflection for BEM12E model. .....	132
Figure 6-110: Predicted nodal first principal stress for CBE model. .....	133
Figure 6-111: Predicted nodal first principal stress for BEM10H model. .....	133
Figure 6-112: Predicted nodal first principal stress for BEM10L model.....	134
Figure 6-113: Predicted nodal first principal stress for BM10H model.....	134
Figure 6-114: Predicted nodal first principal stress for BEM10E model.....	135
Figure 6-115: Predicted nodal first principal stress for BEM12H model. .....	135
Figure 6-116: Predicted nodal first principal stress for BEM12L model.....	136
Figure 6-117: Predicted nodal first principal stress for BM12H model.....	136
Figure 6-118: Predicted nodal first principal stress for BEM12E model.....	137
Figure 6-119: Predicted nodal shear stress plots in bolts for BEM10H model.....	138
Figure 6-120: Predicted nodal shear stress plots in bolts for BEM10L model. ....	138
Figure 6-121: Predicted nodal shear stress plots in bolts for BM10H model. ....	139
Figure 6-122: Predicted nodal shear stress plots in bolts for BEM10E model. ....	139
Figure 6-123: Predicted nodal shear stress plots in bolts for BEM12H model.....	140
Figure 6-124: Predicted nodal shear stress plots in bolts for BEM12L model. ....	140
Figure 6-125: Predicted nodal shear stress plots in bolts for BM12H model. ....	141
Figure 6-126: Predicted nodal shear stress plots in bolts for BEM12E model. ....	141

Figure 6-127: Predicted nodal third principal strain for CB model.  
..... 142

11

Figure 6-128: Predicted nodal third principal strain for CBE  
model..... 142

Figure 6-129: Predicted nodal third principal strain for BEM10H model.  
..... 143

Figure 6-130: Predicted nodal third principal strain for BEM10L model.  
..... 143

Figure 6-131: Predicted nodal third principal strain for BM10H model.  
..... 143

Figure 6-132: Predicted nodal third principal strain for BEM10E model.  
..... 144

Figure 6-133: Predicted nodal third principal strain for BEM12H model.  
..... 144

Figure 6-134: Predicted nodal third principal strain for BEM12L model.  
..... 144

Figure 6-135: Predicted nodal third principal strain for BM12H model.  
..... 145

Figure 6-136: Predicted nodal third principal strain for BEM12E model.  
..... 145

Figure 6-137: Predicted crack patterns of the CB  
model..... 146

Figure 6-138: Predicted crack patterns of the CBE model.  
..... 146

Figure 6-139: Predicted crack patterns of the BEM10H  
model..... 146

Figure 6-140: Predicted crack patterns of the BEM10L model.  
..... 147

Figure 6-141: Predicted crack patterns of the BM10H model.  
..... 147

Figure 6-142: Predicted crack patterns of the BEM10E model.  
..... 147

Figure 6-143: Predicted crack patterns of the BEM12H  
model..... 147

Figure 6-144: Predicted crack patterns of the BEM12L model.  
..... 147

Figure 6-145: Predicted crack patterns of the BM12H model.  
..... 148

Figure 6-146: Predicted crack patterns of the BEM12E model.  
..... 148

12

List of Tables

Table 2-1: Past investigations of different plating material.  
..... 25

Table 2-2: Past investigations of using different anchorage  
configurations in retrofit  
applications..... 28

Table 3-3: Test matrix of study  
..... 32

Table 3-4: Compressive strength of concrete  
batches..... 36

Table 3-5: Mechanical properties of each $\phi 8$ mm bar. .....	39
Table 3-6: Mechanical properties of each $\phi 10$ mm bar. .....	40
Table 3-7: Mechanical properties of each AA coupon. .....	42
Table 3-8: Expansion anchor properties [79].....	42
Table 4-9: Summary of ultimate and failure limits in all specimens. .....	66
Table 4-10: Summary of mechanical response of each element.....	67
Table 4-11: Strength increase in the ultimate and failure states for M10- Specimens.	70
Table 4-12: Strength increase when concrete crushing occurs and yielding in both steel and AA plate for M12-Specimens. .....	70
Table 4-13: Strength increase in the ultimate and failure states for M12- Specimens.	73
Table 4-14: Strength increase when concrete crushing occurs and yielding in both steel and AA plate for M12-Specimens. .....	74
Table 4-15: Strength increase in the ultimate and failure states for different bolt models at low-uniform spacing. .....	76
Table 4-16: Strength increase at concrete crushing and yielding for different bolt models at low-uniform spacing. .....	76
Table 4-17: Strength increase in the ultimate and failure states for different bolt models at high-uniform spacing. .....	78
Table 4-18: Strength increase at concrete crushing and yielding for different bolt models at high-uniform spacing. .....	78
Table 4-19: Strength increase in the ultimate and failure states for different bolt models at low-uniform spacing without bonding. .....	79
Table 4-20: Strength increase at concrete crushing and yielding for different bolt models at low-uniform spacing without bonding. .....	80
Table 4-21: Strength increase in the ultimate and failure states for different bolt models at high-non-uniform spacing.....	82
Table 4-22: Strength increase at concrete crushing and yielding for different bolt	

models at ends of  
beams..... 82

Table 4-23:Summary of ultimate load and failure  
modes..... 85

Table 4-24:Summary of deflections and ductility indices for each  
specimen. .... 91

Table 5-25:Comparison between the FE predicted and experimental measured  
results..... 111

Table 5-26:Summary of stress contour plots.  
..... 119

13

List of Abbreviations

- AA Aluminum alloy
- CC Concrete crushing
- CS Cover separation
- EBR External bonded retrofit
- ED End-plate debonding
- FE Finite Element
- FRP Fiber-reinforced polymers
- IC Intermediate crack-induced debonding
- PR Plate Rupture
- RC Reinforced Concrete
- SY Steel Yielding

14

Chapter 1. Introduction

In this chapter, a brief explanation of the strengthening techniques and materials,

used to rehabilitate structural members, is provided. Past studies and articles taken

from the literature and websites are used to articulate this section.

Afterwards, the

problem statement and research significance are presented to help construct the research

hypothesis. Finally, the structure of the thesis is briefly summarized.

1.1. Overview

A significant number of high-rise buildings were constructed during the first

half of the 20th century using reinforced concrete, precast and steel materials. Now,

many of these buildings have reached the end of their planned service life, where de-

terioration in the form of steel corrosion, concrete cracking and spalling would have a

detrimental effect on their structural integrity [1]. Moreover, the advancement of several

building standards (i.e. ASCE7-16 [2]) have modified their load factors in which the

structures that were previously designed to withstand a certain factored loading com-

binations are now considered structurally over-loaded [3-5]. Therefore, construction



industries have implemented strengthening strategies to upgrade the structural systems of existing buildings and improve their physical performance under existing or modified loads [6, 7]. This advocated researchers to explore different strengthening techniques [8-13].

The first common method of retrofitting was implemented by bonding steel plates to the soffits of Reinforced Concrete (RC) beams using epoxy as a binding

agent. Researchers observed a significant increase in capacity and ductility when loading steel plated RC beams as opposed to regularly RC beams [14-16].

However, its

high-corrosive properties and large density made steel plates a poor externally bonded

reinforcement (EBR) material [10]. As a result, novel techniques for rehabilitation of

RC structures have been incorporated in which Fiber Reinforced Polymers (FRP), in

the form of paper-thin sheets, have been bonded and wrapped around damaged struc-

tural members to increase or maintain their loading capacity. Owing to their high-

strength, lightweight, non-corrosive properties, speed and ease of installation, strength-

ening using FRP has been a popular technique and research topic over the past two

15

decades [17-22]. These systems have been used extensively in the aerospace, auto-

motive, and ship-building industries, and are becoming a mainstream technology in

the structural retrofit field [1]. But an underlying issue that prevents the member from

utilizing the full capacity (mechanical properties) of the FRP sheets is its anchorage

system. This phenomenon is known as debonding and occurs when the FRP sheet loses

its bond with the adjacent concrete surface, due to a crack initiation from the large

strain in the FRP sheet, and detaches from the concrete substrate. By exhibiting this

premature failure mode, the strengthened section does not have enough ductility to uti-

lize the composite's mechanical properties. Other failure modes that occur in retrofit

applications are shown in Figure 1-1, where the most popular failure mode is the plate

end interfacial debonding, which was discussed earlier. In general, this failure mode

occurs when anchorage techniques like wraps and anchors are not used. Another fail-

ure mode is cover separation when a large volume of the concrete is still bonded to the debonded composite possibly making the beam's internal reinforcement visible. Intermediate crack-induced interfacial debonding is when the composite buckles from the beam's midspan, and shear failure mode is when the beam's section shear deficient whereby it fails predominantly in shear. Therefore, researchers have expanded this topic by implementing other anchorage techniques such as wrapping the FRP in specific orientations [23-27] or mechanically fastening the composite material to the RC member using bolts or FRP splays [26, 28-32]. If anchored correctly, FRP-strengthened sections primarily fail by rupture after the strain in the FRP sheet reaches its ultimate strain. Therefore, ductile strengthening material should be used with an effective anchorage system such that the section exhibits strain hardening followed by strain softening during its loading life. Aluminum Alloy (AA) plates are one of the ductile materials that could be implemented as an alternative to FRP composites, since it is capable of yielding considerably before failing by rupture. The comparisons associated with the previously mentioned composite materials are reflected by observing the stress versus strain curves shown in Figure 1-2. The stress versus strain values of CFRP were obtained from [20] and the steel bar and AA plate values were obtained from the coupon tests conducted in this study. Other drawbacks associated with bonding FRPs to structural members are summarized in [33].

16

Figure 1-1: Debonding failure modes [23].

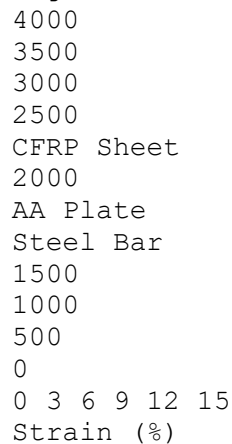


Figure 1-2: Stress versus strain curve for strengthening materials [20].

implementation of AA plates in retrofit applications has been conducted for both shear and flexural deficient RC beams in several studies [10, 11, 34-36]. Mainly, Abdalla et al. and Rasheed et al. [10, 11] have reported that the incorporation of AA plates in retrofit applications have allowed the section to increase in strength, stiffness and ductility when compared to other types of EBR. However, the plated specimens did not reach

17

Stress (MPa)

the ultimate strain of the AA plate due to premature debonding.

Therefore, this study

focused on: (a) preventing premature debonding; (b) increasing stiffness, ductility and

failure modes of AA plated RC beams.

### 1.2. Problem Statement

The method of using EBR materials to strengthen aging and/or deteriorating RC

structures has proven its feasibility and effectiveness in the past studies [8, 14, 37]. The

implementations of steel, FRP and other strengthening materials in retrofitting applica-

tions has shown promising results in terms of increasing the capacity and stiffness in

RC members. The usage of AA plates in retrofit application has proven its viability in

the area of strengthening; however, these studies [10, 11, 34-36] have reported prema-

ture debonding due to the inefficient anchorage systems. Therefore, the incorporation

of bolting and bonding AA plates, which have the capabilities of overcoming some of

the old materials' shortcomings, could physically supplement the RC member with both

strength, stiffness and ductility. In addition, the utilization of bolts in anchoring the AA

plates may overcome the typical failure modes summarized in Figure 1-1 and allow the

loaded section to use the full potential of the AA plate. The

introduction of bolting AA

plates as a strengthening application will be advantageous to engineers and researchers

locally, regionally and internationally.

### 1.3. Research Significance

The susceptibility, of aging and/or deterioration of RC structures has been a

growing issue in the beginning of the 20th century. This resulted in weakening of RC

structures and reduction in their flexural capacity. Moreover, several buildings are being

considered as overloaded due to the changes in load factors given by structural building

standards like the ASCE7-16 [2]. Therefore, engineers remedied these issues by utilizing FRP or steel material as EBR to effectively maintain or increase the loading capacity of the structural member. However, due to their limitations such as: brittle failure and sensitivity to fatigue discussed earlier, its deficiencies were highlighted, and triggered engineers and researchers to propose different solutions. As a result, structural design standards like the American Concrete Institute (ACI-440.2R-08) offer systematic design procedures when evaluating the FRP retrofitted sections [38]. These techniques underestimate the FRP's capacity to avoid premature failure modes, like debonding

18

or delamination. In general, failure modes govern whether the section is utilizing the EBR completely or not. Therefore, both new strengthening material and anchorage techniques need to be identified to mitigate these shortcomings and make a sound contribution to the field of strengthening and retrofitting using EBR. In this research, both materials and anchorage systems were the test parameters that were investigated, where AA plates were used as the strengthening material and bolts with/without epoxy were used as the anchorage technique. These materials were obtained from external manufacturers [39, 40]. The significance of this research is to investigate the feasibility of bolting and/or bonding AA plates, as an alternative EBR, to retrofit flexurally deficient RC beams.

#### 1.4. Research Objectives

This research is conducted to study the flexural behavior of externally strengthened RC beams using AA plates anchored with bolts with/without epoxy. The objectives of this study are:

1. Conduct an experimental investigation to study the strength and ductility of AA plates as EBR material.
2. To study the strength, stiffness and ductility of flexurally deficient RC beams that are externally strengthened using AA plates anchored with bolts and/or bonded with epoxy.
3. Study the effect of bolt size, spacing and embedment depth on the failure mode of the externally strengthened RC section.
4. Perform a parametric study by varying the spacing and embedment depth of the

bolts.

5. Predict the load versus deflection curves of selected specimens with a nonlinear finite element analysis using a commercial software, Ansys Mechanical APDL [41].

### 1.5. Thesis Organization

The work described herein consisted of:

1. Chapter 1: Introduction. Provides an overview on the effects of anchoring composite materials to RC members using different techniques, addresses the significance of this project in the research community, and presents the objectives of this study.

2. Chapter 2: Literature Review. Presents a comprehensive literature review that covers different external retrofit strategies that have been investigated in past experimental and numerical studies.

3. Chapter 3: Experimental Program. Covers the geometric and mechanical properties of the RC beams, AA plates and anchorage techniques used in this study. It describes the procedure for testing the mechanical properties of the EBR system, the preparation steps taken for strengthening the RC beams, and the test setup followed during this project for the RC beam specimens.

4. Chapter 4: Results and Discussions. Provides a detailed discussion of the recorded results taken during testing, where both load versus deflection and load versus strain curves were generated for each beam. The load and deflection values at different states which include: (a) yielding of steel; (b) yielding of AA plate; (c) crushing of concrete; (d) ultimate load; (e) failure of section were identified.

Furthermore, the effects of the various parameters were explored by comparing the stiffness response, load and deflection values for each specimen. Captures of all specimens, at failure, were presented and related to the strain measurements for each material. Finally, the ductility index of each specimen was evaluated to quantify the amount of ductility experienced by each specimen.

5. Chapter 5: Finite Element Modeling. Presents a comprehensive approach on modelling retrofitted sections using a commercial FE software. Previously de-

rived constitutive models were employed within the FE software to simulate the nonlinear properties of specimens. All specimens were successfully modelled in which the results obtained from the FE software correlated very well with the results obtained from the experiment. These validated models were then used to generate contour plots and concrete cracking patterns where the stress and crack propagation were observed and discussed.

20

6. Chapter 6: Conclusion. Summarizes the key findings deduced from the experimental and numerical investigations carried out in this study.

21

Chapter 2. Literature Review

A general increase in high-rise buildings and skyscrapers exist in countries where heavy real estate companies are based, like: United Arab Emirates, Singapore, China, Mexico City, Canada, USA and many more [42]. These immense buildings necessitate government sectors and clients to start developing strategies that would help prolong these structures for a longer period of time. Strengthening and rehabilitation of structures has been an effective solution in repairing deteriorated or damaged members since the beginning of the 20th century [1, 6, 7, 11, 43]. Namely, many investigations were conducted to study the flexural behavior of strengthened RC beams and their failure modes using FRP, steel, and AA plates [4, 10, 14, 16, 37]. This chapter presents an extensive literature review on the implementation of strengthening using various composites that vary based on their mechanical properties and anchorage techniques.

2.1. Flexural Strengthening

Externally bonding materials to the surfaces of structural members is a common retrofitting practice that several researchers have performed using different types of composite materials. Mainly, these applications include fixing materials like steel plates, Glass FRP (GFRP) sheets/plates and CFRP sheets/plates onto the soffits of RC beams to enhance their flexural capacity. Furthermore, the implementation of different FRP material with different textures (plates or sheets) were reviewed and summarized in the following subsections.

2.1.1. Steel plates. The use of bonded steel plates, as an EBR system for RC members, was first reported in 1964 when malleable steel plates with an adhesive compound were applied to load bearing beams in the basement of an apartment building, in Durbin, South Africa [44]. This motivated several researchers to conduct experimental investigations on using steel plates for external strengthening applications. Oh et al. [45] investigated the static and fatigue behavior of RC beams strengthened with steel plates. The experimental program involved 27 RC beams that were divided into two categories: static and fatigue tests. Fourteen specimens were used for the static test, where one of the specimens was reserved as a control specimen and the remaining thirteen specimens were externally strengthened with different steel plates and adhesive thicknesses. Four RC beams were tested against fatigue, where one of the specimens was reserved as a control specimen and the remaining three were strengthened similar to the strengthened specimens in the static test. Furthermore, load versus deflection curves were generated in which all steel plated specimens were not able to fully utilize the steel plates' capacity and ductility due to end-debonding and cover separation failure modes as shown in Figure 2-3. As a result, plate separation was the main contribution to the specimens failure in both tests, where some RC beams failed by shear; due to the enhanced strengthening of their flexural capacities. Figure 2-3: Load versus deflection curves of steel plated specimens [45]. Moreover, Swamy et al. [46] performed an experimental study on the effect of plate thickness in the failure mode of the strengthened RC beams. It was observed that a 3 mm thick steel plate bonded to the soffit of an RC beam exhibited failures that consisted of a combination of flexure and flexure-shear failure modes, with flexure being the most common. However, at ultimate load, the section failed in concrete cover separation due to the initiation of a shear crack at the end of the plate which propagated along the beam. For 6 mm plates, the failure mode consisted of shearing of the concrete along the internal bottom reinforcement, causing a concrete cover separation failure.

As a result, the failure was sudden and brittle. Similarly, Gao et al [18] performed a comparative experimental study where different plating materials, loading cases, and end anchorage techniques were the varying parameters. However, only plating of steel as an EBR material will be discussed here. Furthermore, Gao et al. prepared three

23 out of 17 RC beams where one beam was left un-strengthened (regarded as the control beam) and the other two specimens were bonded with steel plates. After monotonically loading the specimens, it was observed that a drastic increase in capacity was achieved in the plated specimens as compared to that of the control specimen. As a result, the control beam failed in flexure whereas the strengthened specimens failed due to cover separation.

2.1.2. FRP plates. Recently, FRP were integrated with retrofit applications due to their extremely light weight characteristics combined with their superior mechanical properties. This was accomplished by bonding FRP plates to the soffits of RC beams, as shown in Figure 2-4. Rahimi and Hutchinson [47] conducted an experimental study on bonding two types of FRP plates, CFRP and GFRP, to the soffits of RC beams. The test matrix consisted of three beam groups with similar cross-sectional details, where the first two groups were reinforced with the same longitudinal reinforcement and varied with shear reinforcement, and the last group was reinforced with more longitudinal reinforcement than the first two beam groups. Moreover, the strengthening techniques used for all specimens were consistent, in which all RC beams' soffits were externally bonded with FRP plates along the beams' spans. As a result, the strengthened specimens in the first two groups, whether using CFRP or GFRP laminates, have failed prematurely; mainly, in end-debonding/cover separation, shear or a combination of both. However, the FRP strengthened specimens in the last group failed by concrete crushing followed by debonding/cover separation. Therefore, Rahimi and Hutchinson have concluded that despite varying the strengthening material type, longitudinal and vertical reinforcements; the failure modes exhibited by flexurally strengthened RC beams are



governed by end-debonding and cover separation, respectively. Gao et al. [18] prepared five out of 17 RC beams that were plated with CFRP plates in which three preloading conditions were simulated: pre-unloading, sustained load at 5 kN and sustained load at 10 kN. The test setup consisted of a four point bending that followed a displacement protocol whereby all specimens were crushed until the sections' maximum capacity was reached. As a result, the CFRP plated specimens exhibited two failure modes: failure due to debonding of CFRP plates at ends and shear failure of concrete (for pre-unloaded specimens). Table 2-1 summarizes the other in-

24  
 investigations of different plating material, mechanical behavior and failure modes. The failure modes described herein were categorized into two types; sudden and typical. The sudden failure modes were reported as end-debonding (ED), intermediate-crack debonding (IC), or cover separation (CS). The typical failure modes were reported as concrete crushing (CC) and steel yielding (SY), or plate rupture (PR) with the combination of CC and SY.

Figure 2-4: Externally strengthened continuous RC beam [48].

Table 2-1: Past investigations of different plating material.

Reference	CFRP	GFRP	Steel	Ductile	Brittle	Sudden <sup>1</sup>	Typical <sup>2</sup>
[47]	X	X	X				
[18]	X	X	X				
[48]	X	X	X				
[49]	X	X	X				
[50]	X	X	X				
[51]	X	X	X				
[45]	X	X	X				
[46]	X	X	X				
[18]	X	X	X				

1 ED; IC; CS

2 CC; SY; PR

25

2.1.3. FRP sheets. After realizing the drawbacks of using FRP plates in retrofit applications, engineers and researchers have investigated the implementation of using FRP sheets as an alternative. The flexibility of FRP sheets allows engineers to incorporate them in several applications including retrofit. Arduini et al. [52] performed an experimental investigation in which 18 RC beams were prepared and cast; mainly, two

groups of nine beams were divided according to their geometric and reinforcement details. One beam of each group was left un-strengthened while the rest of the beams of each group were strengthened using CFRP sheets by varying the number of sheets used and their orientation. As a result, all the FRP-strengthened specimens exhibited an increase in flexural capacity compared to that of the control beams; however, their failure modes were sudden and involved debonding or cover separation from the concrete surface whereas the control beam typically failed in flexure. Therefore, it was concluded that the implementation of FRP sheets promoted stiffness and impeded ductility. Other researchers arrived at similar conclusions in which the implementations of different strengthening material like CFRP, GFRP, and a hybrid of both were experimentally tested [13, 17, 53-55].

2.1.4. Aluminum alloy plates. Recently, researchers have begun studying high tensile strength AA plate as a strengthening technique [3, 10, 11, 20] due to its high strength and ductility comparable to that of steel, light weight comparable to that of FRP, and high resistance to both corrosion and temperature degradation. An experimental study was conducted by Rasheed et al. [10] where AA plates were used as an EBR retrofit with/without single-layer and double-layer U-wrapped CFRP sheets for RC beams. The program included a group of beams, strengthened and unstrengthened, and loaded monotonically to test the flexural behavior of the beams. It was observed that the strengthened beams, without end anchorage, had an increase in strength from 13% to 40% and an increase in ductility when compared to the un-strengthened specimen. In contrast, the strengthened beams anchored with variable layers of CFRP sheets also exhibited higher ductility but lower strength capacity than the un-strengthened specimens. The failure modes for the strengthened beams without end anchorage was failure by full debonding whereas the strengthened beam with end anchorage failed by localized debonding and flexure. Ultimately, a strain-hardening model was incorporated to

26

capture the stress-strain curves of the AA plates and to predict the strengthened RC

beams' response as an analytical approach, which agreed with the experiment's results. Furthermore, it was shown that the debonding strain formula, adopted by ACI 440.2R-08 [38], was capable of predicting debonding strain of AA strengthened beams without end anchorage.

## 2.2. Anchorage Techniques

Several comparative studies were performed to prevent or postpone the overall failure mode, debonding or delamination, and force the strengthened RC beams to fail due to FRP rupture or shear. Different anchorage techniques were studied such as: FRP sheet U-wraps, FRP splay anchors and steel bolts.

### 2.2.1. U-wrap anchorage.

Plate-end anchorage was studied to verify whether a cover separation failure mode is avoidable as Smith and Tag [56] demonstrated when adding plate-end U-jackets, which was able to shift the failure mode from cover separation or end-interfacial debonding to concrete crushing. As a result, researchers began distributing the U-jackets across the span of the RC beam, with consistent spacing. This method resulted in shifting most of the failure modes to FRP rupture [25, 57-59]. Although Pham and Al-Mahaidi [57] found that the addition of U-jacket, across the span, contributed in limiting end debonding failure mode, the failure mode was shifted to intermediate-span debonding at a higher load. This was often coupled with the rupture of the end U-jacket. Ali et al. [16] concluded that RC beams externally strengthened with CFRP sheets develop higher load capacities and shift debonding when CFRP mechanical anchors are used. In this study, an extensive review on U-wrap anchorage was conducted in which Table 2-2 was developed to summarize the anchorage configuration used to assist the RC sections in utilizing the flexural strengthening material in several studies. It can be observed that a pattern is apparent in which the implementation of end and end-intermediate U-wrap configurations has a higher probability of failing immediately as opposed to using full spanned U-wrap configurations. The benefits of fully wrapping RC beams are: (a) eliminating ED and IC failure modes [60]; (b) reinforcing against shear due to the individual fiber orientations that are lined normal to most of the shear cracks [25]; (c) contributing to the flexural behavior [54].

Table 2-2: Past investigations of using different anchorage configurations in retrofit applications.

Reference	U-wrap	Configuration	Strengthening Material	Failure Modes
End and Full CFRP	CFRP	AA		

Sudden	Typical	plate	Intermediate wrapped	Plates	Sheets	Plate
[56]	X	X	X			
[25]	X	X	X	X	X	
[60]	X	X	X			
[10]	X	X	X	X	X	
[61]	X	X	X			
[62]	X	X	X			
[54]	X	X	X			

[56] X X X

[25] X X X X X

[60] X X X

[10] X X X X X

[61] X X X

[62] X X X

[54] X X X

1 ED; IC; CS

2 CC; SY; PR

2.2.2. Bolts and mechanical fasteners. Several research projects were conducted to study techniques in manipulating the physical structure of FRP sheets and

form bolt-like anchors called Splay Anchors [63-65]. Kalfat et al. [64] conducted an

extensive review on the different anchorage techniques reported to date, where it was

reported that the incorporation of FRP anchors combined with U-wrap configurations

enhanced the performance of the U-wrap. However, the failure modes were shifted

from End-debonding/Intermediate-crack-debonding to FRP pullout. Moreover, Eshwar

et al. [66] studied the effect of a beam's soffit curvature on the performance of FRP

anchors in flexural strengthening applications. The experimental program consisted of

ten RC beams in which three of the beams consisted of flat soffits; one was left un-

strengthened, one was strengthened using a three-ply CFRP wet layup laminate and

one was strengthened with one CFRP precured laminate. Six beams were constructed

with varying soffit-curvatures that were strengthened by bonding CFRP laminates using

wet layup and precured methods, respectively, and the last specimen was strengthened

with CFRP laminates and anchored with GFRP splay anchors. The results indicated

that the incorporation of FRP anchors enhanced the flexural capacity and ductility of

the strengthened beam as opposed to the specimens that were strengthened using the

wet layup and precured method, respectively. However, it was observed that the failure

mode was still sudden since it consisted of the peeling of the CFRP laminates cou-

ple with the pull-out of the FRP anchors as shown in Figure 2-5. Other researchers have studied the effects of implementing FRP anchors in structural engineering applications [21, 67, 68].

28

Figure 2-5: Failure mode of splay anchor in [66].

Furthermore, researchers also investigated the implementation of bolts as a form

of anchorage in flexural strengthening applications. For example, Ebead and Mar-

zouk [69] conducted an experimental investigation to study the behavior of a two-way

slab strengthened on the soffit of the slab around the column. The program was di-

rected at testing the effectiveness of two configurations of steel plates and four different

arrangements of steel bolts. As a result, the slabs showed an increase in stiffness and

energy absorption. Also, the load-carrying capacity of the strengthened slabs was in-

creased by 56.55, 57.76, and 64.56% over that of the control specimen.

Consequently,

another study was conducted by Oehlers [70] to compare the performance of two an-

chorage systems - adhesive bonded and bolted plates for strengthening of RC beams.

The adhesive bond anchorage has a higher stiffness increase than that of the bolted

anchorage, but the failure mode for adhesively bonded plates is brittle as opposed to

bolted plates, which have a more ductile failure. El-Maaddawy [71]

investigated the

effectiveness of different mechanically fastened composite systems for retrofitting rel-

atively large-scale corrosion-damaged reinforced concrete beams. The experimental

program comprised of beams that were retrofitted with composite plates secured with

powder-actuated fasteners (PAF), expansion anchor bolts (EAB), and threaded anchor

bolts (TAB). The results indicated that there was a small increase in strength for plated

RC beams using PAF, but a larger increase in strength for plated RC beams with both

EAB and TAB. In addition, Gao et al. [18] also tested the flexural enhancement of bolt-

29

ing steel plate to RC beams, where it was concluded that the bolted steel plate specimens

were capable of preventing ED/IC failure modes.

### 2.3. Finite Element Simulations

Other numerical studies were conducted to simulate retrofit applications using

finite element (FE) software packages [72-74]. These FE simulations are dependent on the constitutive laws to simulate the nonlinear properties of concrete, FRP and steel. As a result, several of these researchers have reported accurate predictions of the load versus deflection curves when compared to that of the experiment [3,74]. Hawileh et al. [74] conducted a numerical investigation to simulate an RC T-beam shear-strengthened using side-bonded CFRP sheets. This model was subjected to cyclic loading where the load versus displacement hysteresis loops were generated and compared against the experiment.

30

### Chapter 3. Experimental Program

This project aims at investigating the effect of bolting and/or bonding AA plates on the flexural strength of flexurally deficient RC beams. The anchorage techniques and strengthening materials described herein are required to assist the strengthened specimens in exhibiting ductile and controlled failure modes throughout its loading life.

This chapter presents an in-depth review on the details of the RC specimens' geometry, mechanical properties of the materials used, the techniques followed prior and during strengthening applications, and the loading scheme followed during the tests.

#### 3.1. RC Beam Details

A total of 16 RC beams were designed with high shear capacity and low flexural capacity—forcing the beams to fail in flexure. This design approach followed the ACI 318-14 [75] design provisions. The dimensions of each specimen is 1840 mm × 240 mm × 125 mm, the longitudinal reinforcing bar diameters used are 10 mm and 8 mm, and the transverse reinforcement are 8 mm in diameter and they are spaced at 100 mm center-to-center as shown in Figure 3-6.

3.1.1. Geometry and design. The experimental program was divided into three groups: C-Specimens, M10-Specimens, and M12-Specimens. The C-Specimens, shown in Figure 3-7, consist of two RC beams where one beam was un-strengthened and used as a control beam (CB), and the other specimen was strengthened by means of externally bonding an AA plate to its soffit and used as a control beam strengthened an

epoxy-bonded AA plate (CBE). Since all beams are flexurally deficient, the retrofit applications that are conducted during this study are located at the soffits of the beams. Moreover, the M10-Specimens, shown in Figure 3-8, consist of seven RC beams in which two beams are strengthened by mechanically fastening AA plates using a large number of M10 bolts [39] (BM10H), two beams with AA plates that are fastened using a low number of M10 bolts, two beams with AA plates that are bonded and bolted using epoxy and a high number of M10 bolts simultaneously (BEM10H). Finally, the M12-Specimens, shown in Figure 3-9, consist of the same number of beams and retrofit schemes; however, the mechanical fasteners used are M12 bolts (BM12H, BM12L, and BEM12H). A summary of the test matrix is shown in Table 3-3. Further description related to the material's mechanical properties will be discussed in the following sections.

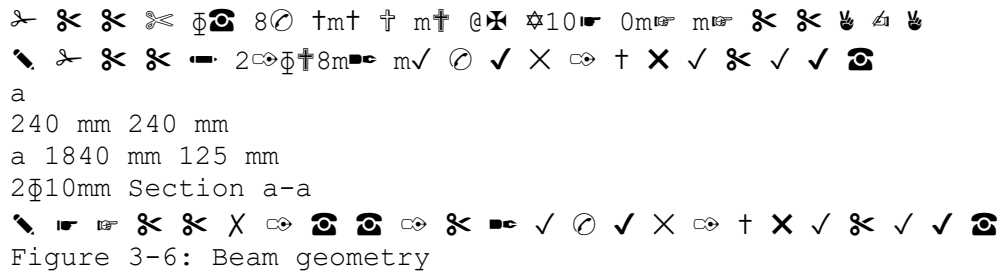


Figure 3-6: Beam geometry

a  
 240 mm 240 mm  
 a 1840 mm 125 mm  
 2φ10mm Section a-a

b  
 240 mm 240 mm  
 a 1840 mm 125 mm  
 Section a-a  
 (a) CB  
 b 1840 mm 125 mm  
 240 mm 240 mm  
 b 3 mm 50 mm  
 1350 mm  
 AA Plate Section b-bEpoxy  
 (b) CBE

Figure 3-7: Geometry and details of CB-Specimens.

Table 3-3: Test matrix of study

Designation	AA Plates	Anchorage	Number of Bolts	Position	Plate Thickness:
CB	-	-	-	-	1
CBE	X	X	-	-	1
BEM10H	X	X	X	-	X - 2
BEM10L	X	X	-	X	X - 2
BEM12H	X	X	X	-	X - 2
BEM12L	X	X	-	X	X - 2
BM10H	X	-	X	-	X - 2

BM12H X - X - X - 2  
BEM10E X X X - - X 1  
BEM12E X X X - - X 1  
32  
1840 mm  
a 1350 mm 125 mm  
240 mm 240 mm  
a 3 mm 50 mm  
Section a-a  
AA Plate HST3 M10 100 mm Epoxy  
(a) BEM10H  
1840 mm  
b 1350 mm 125 mm  
240 mm 240 mm  
b 200 mm 3 mm 50 mm  
Section b-b  
AA Plate HST3 M10 Epoxy  
(b) BEM10L  
1840 mm  
c 1350 mm 125 mm  
240 mm 240 mm  
c 3 mm 50 mm  
100 mm Section c-c  
AA Plate HST3 M10  
(c) BM10H  
1840 mm d  
1350 mm 125 mm  
240 mm 240 mm  
100 mm d 3 mm 50 mm  
Section d-d  
AA Plate HST3 M10 Epoxy  
(d) BEM10E

Figure 3-8: Geometry and details of M10-Specimens.

3.1.2. Specimen instrumentation. The Strain Gages were installed such that the moment-induced compression/tension strains would be measured and recorded during the tests. In this study, all strain gages were placed at the mid-span of each specimen; whereby one strain gage was bonded to the top concrete fiber, one strain gage was bonded to the AA plate, and two strain gages were bonded to the bottom steel bars. Figure 3-10 shows the Strain Gage locations in all the specimens tested in this project.

33

3.1.3. RC specimen preparation. The steel cages were prepared, as shown in Figure 3-11a, whereby the strain gages were bonded to the steel bars as shown in Figure 3-11b. The formwork was prepared for each specimen such that the poured concrete would occupy the designed dimensions as shown in Figure 3-11c and Figure 3-11d.



1840 mm  
a 1350 mm 125 mm  
240 mm 240 mm  
a 3 mm 50 mm  
AA Plate HST3 M12 100 mm

Section a-a

Epoxy

(a) BEM12H

1840 mm  
b 1350 mm 125 mm  
240 mm 240 mm  
b 200 mm 3 mm 50 mm

Section b-b

AA Plate HST3 M12 Epoxy

(b) BEM12L

1840 mm  
c 1350 mm 125 mm  
240 mm 240 mm  
c 3 mm 50 mm

100 mm

Section c-c

AA Plate HST3 M12

(c) BM12H

1840 mm d  
1350 mm 125 mm  
240 mm 240 mm  
100 mm d 3 mm 50 mm

Section d-d

AA Plate HST3 M12

Epoxy

(d) BEM12E

Figure 3-9: Geometry and details of M12-Specimens.

34

Concrete Strain Gage

240 mm

3 mm

1350 mm

1840 mm

2□Steel Strain Gages AA Plate Strain Gage

Figure 3-10: Strain gage locations.

(a) Steel cage (b) Location of strain gages

(c) Steel cage within formwork (d) Finalized Specimens

Figure 3-11: RC beam specimen preparation.

### 3.2. Material Specification

In this section, the mechanical properties of the material were obtained by con-

ducting both compressive and tensile tests; depending on the type of material being

investigated. Concrete cubes, steel coupons, and AA dog-bone shaped plates were pre-

35

pared in the labs and tested according to different ASTM standards [76-78]. Further

details regarding the tests and application will be discussed in the following sections.

3.2.1. Concrete compression test. The 16 specimens were cast using normal weight concrete and were designed to achieve a compressive strength equal to 40 MPa

at 28 days. Since the beams were prepared in four batches, four concrete cubes were obtained from the manufacturer to conduct compressive tests as per ASTM C109/C109m

standard [76]. The dimensions of each cube were 150 mm × 150 mm × 150 mm. Moreover, the cubes were crushed on the same days as the beams were tested, which

provides insight on the exact mechanical properties for each RC beam during the test.

The compressive strength values were used in several classical models that were, then, employed in nonlinear FE software to capture the nonlinear behavior of concrete. Table

3-4 presents the compressive strength of each batch of concrete, and Figure 3-18

shows the concrete cubes during preparation and after testing.

Table 3-4: Compressive strength of concrete batches.

Batch Number 1 2 3 4

Cube Compressive Strength (MPa) 45 45 48 47

Cylinder Compressive Strength (MPa) 36 36 38.4 37.6

3.2.2. Tensile testing of normal strength reinforcing bars. The steel bars

used to reinforce the beams are 8 mm and 10 mm in diameter. Their mechanical prop-

erties were obtained by conducting tensile tests, for both bar diameters, according to

the ASTM 370-18a [77]. Instron Universal Testing was used to perform the tensile

test, where the loading rate for all coupon tests was 1 mm/min [77].

Afterwards, the

offset method was used, as shown in Figure 3-13, where line OM represents the user

specified offset (default value of 0.2%) and line mn should be parallel to line OA. The

intersection at point r was taken as the yield stress of the specimen.

3.2.2.1. Mechanical properties of  $\phi 8$  mm bar. Three  $\phi 8$  mm bars were prepared for tensile testing where the total length, grip, and diameter of each bar is 300

mm, 50 mm, and 8 mm, respectively, as shown in Figure 3-14. The test setup consisted

of 50 mm grip length from both edges of the steel bar and a displacement controlled

36

(a) Un-crushed concrete cubes

(b) Crushed concrete cubes

Figure 3-12: Concrete cube tests and preparations.

Figure 3-13: Offset Method [77].

axial load was applied, with a rate of 1 mm/min [77], as shown in Figure 3-15a. The

steel bars were tested to rupture as shown in Figure 3-15b, and the stress and strain curves were plotted, as shown in Figure 3-16. The offset method was implemented on

37

the stress-strain curve, in Figure 3-16, to calculate the yield strength ( $F_y$ ) and Young's modulus of elasticity ( $E$ ). Finally, these parameters were combined with the elongation and maximum tensile strength ( $F_u$ ) values and tabulated in Table 3-5.

Grip Length 50 mm  
Grip Length 50 mm  
8 mm  
300 mm

Figure 3-14: Dimensions of a steel reinforcing  $\phi 8$  mm bar in a tensile test.

(a) Test setup (b) Ruptured specimens

Figure 3-15: Steel tensile test  $\phi 8$  mm.

700  
600  
500  
400  
300  $\phi 8$  mm(1)  
 $\phi 8$  mm(2)  
 $\phi 8$  mm(3)  
200  
100  
0  
0 0.02 0.04 0.06 0.08 0.1 0.12 0.14

Strain (mm/mm)

Figure 3-16: Stress versus strain curve for each  $\phi 8$  mm bar.

38

Tensile Stress (MPa)

Table 3-5: Mechanical properties of each  $\phi 8$  mm bar.

Specimen ID	E (GPa)	$F_y$ (MPa)	$F_u$ (MPa)	Elongation (%)
$\phi 8(1)$	199.9	554.7	641.4	12.5
$\phi 8(2)$	200	540	627.4	11.4
$\phi 8(3)$	199.8	574.9	651.6	11.4
Average	199.9	556.5	640.1	11.8

3.2.2.2. Mechanical properties of  $\phi 10$  mm bar. Similarly, three  $\phi 10$  mm bars

were prepared for tensile testing where the total length, grip, and diameter of each bar

is 300 mm, 50 mm, and 10 mm, respectively, as shown in Figure 3-17. The test setup

consisted of 50 mm grip length from both edges of the steel bar and a displacement

controlled axial load was applied, with a rate of 1 mm/min [77], as shown in Figure 3-

18a. The steel bars were tested to rupture as shown in Figure 3-18b, and the stress

and strain curves were plotted, as shown in Figure 3-19. The offset method was imple-

mented on the stress-strain curve, in , to calculate the yield strength ( $F_y$ ) and Young's

modulus of elasticity (E). Finally, these parameters were combined with the elongation and maximum tensile strength (Fu) values and tabulated in Table 3-6.

Grip Length 50 mm Grip Length 50 mm  
10 mm  
300 mm

Figure 3-17: Dimensions of a steel reinforcing  $\phi 10$  mm bar in a tensile test.

(a) Test setup (b) Ruptured specimens

Figure 3-18: Steel tensile test for  $\phi 10$  mm.

39

700

600

500

400

300

$\phi 10$  mm(1)

$\phi 10$ mm(2)

200  $\phi 10$ mm(3)

100

0

0 0.02 0.04 0.06 0.08 0.1 0.12 0.14

Strain (mm/mm)

Figure 3-19: Stress versus strain curve for each  $\phi 10$  mm bar.

Table 3-6: Mechanical properties of each  $\phi 10$  mm bar.

Specimen ID E (GPa) Fy (MPa) Fu (MPa) Elongation (%)

$\phi 10$ (1) 200.1 542.0 634.5 13.4

$\phi 10$ (2) 199.8 559.0 658.2 13.0

$\phi 10$ (3) 200.2 545.7 642.7 12.3

Average 200.0 548.9 645.1 12.9

3.2.3. Tensile testing for AA plates. The AA plates used during this study

are from the AA5083-H111 family. Tensile tests using the Instron universal testing

machine (UTM) were conducted. Furthermore, the dog-bone shaped specimens were

prepared, as per ASTM E8 [78]. The total length, gage length and grip length are

385 mm, 225 mm and 75 mm, respectively, as shown in Figure 3-20. The test setup

was carried out by gripping 50 mm from both edges of each AA coupon as shown in

Figure 3-21a. The UTM was programmed to subject each coupon to a displacement

rate of 0.5 mm/min [78]. As a result, the AA specimens ruptured in the gage length

as shown in Figure 3-21b. The stress and strain values were plotted against each other

and are shown in Figure 3-22. Afterwards, the yield strength, ultimate tensile strength,

modulus of elasticity, and elongation were extracted as shown in Table 3-7.

3.2.4. Mechanical fasteners. The mechanical fasteners used to anchor the AA

plates were provided by the manufacturer, Hilti [39]. The anchor models used herein

40

Tensile Stress (MPa)

50 mm

225 mm 75 mm

Figure 3-20: Dimensions of a dog-bone shaped AA plate [78].

(a) Test setup (b) Ruptured samples

Figure 3-21: AA plate tensile test.

350

300

250

200

AA1

AA2

150 AA3

AA4

AA5

100

50

0

0 0.02 0.04 0.06 0.08 0.1 0.12 0.14 0.16 0.18

Strain (mm/mm)

Figure 3-22: Stress versus strain curve for each AA coupon.

were: HST3 M10×90 and HST3 M12×105. Their mechanical properties and geomet-

ric details were obtained from Hilti's HST3 technical datasheet [79] and are presented

in Table 3-8, where  $f_{u,t}$  is the ultimate tensile strength,  $A_{se,V}$  is the gross area of the

sleeves,  $d_o$  is the diameter of the bolts,  $h_{eff}$  is the depth of the bolts,  $s_{min}$  is the min-

41

Tensile Stress (MPa)

Table 3-7: Mechanical properties of each AA coupon.

Specimen ID E (GPa)  $F_y$  (MPa)  $F_u$  (MPa) Elongation (%)

AA1 65936 161.4 329.2 16.6

AA2 64103 152.2 319.1 17.6

AA3 65396 151.7 312.1 16.5

AA4 63690 148 313.5 17.0

AA5 71036 145 309.1 18.0

Average 66032.2 151.6 316.6 17.1

Manufacturer - 163.9 301.5 21.05

imum center-to-center spacing between the bolts based on bolt shear strength, pry-out

and pull-out action,  $C_{min}$  is the minimum distance from the bolt to the edge of the

concrete, and  $T$  is the torque required to fix the bolts. For brevity, a simple diagram

is presented to clarify the details including the geometric limitations imposed by [79],

as shown in Figure 3-23. The expansion anchor models, used in this project, consisted

of sleeves in the bottom such that once they are settled within the concrete element, any normal force that is aimed to jack the bolt out is resisted due to the expansion of its sleeves. Figure 3-24 shows both models used in this project, where each bolt consisted of a knut, a washer, and a sleeve. The knut was responsible for subjecting the bolt into a pretension loading configuration such that with every turn of the knut, load is transferred to the washer which then bears on the object required to be fixed.

Table 3-8: Expansion anchor properties [79].

Anchor Type	HST3 M10×90	HST3 M12×105
futa (MPa)	800	800
Ase,V (mm <sup>2</sup> )	58	84.3
do (mm)	10	12
heff (mm)	90	105
Smin (mm)	70	80
Cmin (mm)	70	80
T (N-m)	45	60

Smin

Cmin

Cmin

Figure 3-23: Diagram depicting HST3 expansion anchors' geometric limitations in concrete.

42

(a) HST3 M10×90 (b) HST3 M12×105

Figure 3-24: Hilti expansion anchor models.

3.2.5. Epoxy. Epoxy resin is a popular adhesive that is used to anchor different

retrofit systems and provide them with structural homogeneity throughout their loading

life [40]. In this project, a two-component thixotropic epoxy adhesive was provided by

the manufacturer, MAPEI [40], in which the adhesive consisted of two parts; mainly,

the Adesilex PG2 SP (part A) and the hardener (part B), shown in Figure 3-25. Gen-

erally, these two parts are mixed together according to a specific ratio imposed by the

technical datasheet [80]. In this project, the ratio of part A-to-part B was 3:1 where the

compound's mechanical properties, provided by the manufacturer [40], are 80 MPa, 40

MPa, 8000 MPa, 4000 MPa and 30 MPa for Compressive strength (ASTM D-695)

, flexural strength (ISO-178), Modulus of elasticity under compression (ASTM D-695),

Modulus of elasticity in flexural (ISO- 178), and tensile strength (ASTM D-638), re-

spectively [80]. Mainly, the flexural modulus of elasticity will be employed within the

numerical software explained in the following chapters.

(a) Part A (b) Part B

Figure 3-25: Two-component epoxy.

43

### 3.3. External Strengthening

The content described herein describes the steps that were taken during the

strengthening application. In this project, two anchorage tools were used; Adesilex

PG2 SP epoxy and HST3 M10/M12 expansion anchors. Moreover, the strengthening

material anchored were AA5083-H111 plates.

3.3.1. Surface preparation. Prior to external strengthening, the surfaces of the

concrete specimens and the AA plates were roughened using an electrical grinder. This

enhanced the bond behavior between the epoxy and the retrofit system; yielding an ideal

surface profile that helps ensure the design load transfer [38]. The following sections

will briefly explain the different types of surface preparations conducted during this

project.

3.3.1.1. Surface preparation for AA plates. Achieving a rough surface, when

conducting retrofit applications, is important for maintaining a homogeneous anchorage

system and a strong bond between the strengthening material and the RC host. In

this project, the plates were abraded using an electrical grinder similar to past studies

[10, 11]. This was performed on one side of the AA plate; the side facing the concrete

specimen as shown Figure 3-26. According to the test matrix shown in Table 3-3, a

total of 15 plates were grinded for strengthening applications.

Default surface Grinded surface

Figure 3-26: Default and smoothed surface of AA plates.

44

3.3.1.2. Surface preparation for concrete specimens. Similarly, the concrete

specimens were grinded in order to ensure ideal design load transfer as specified in the

ACI 440.2R-08 [38]. Since the RC members will be subjected to flexural loading, the

concrete surface preparation was classified as a bond-critical application. The bond-

critical application should follow the abrasion steps found in ACI-546 [81], where thin

layers of concrete were abraded, using electrical grinders, from the soffit of each RC

specimen. Figure 3-27a and Figure 3-32b show the default and grinded surfaces of the

beams, respectively, and the electrical grinder is shown in Figure 3-32e.

(a) Default surface (b) Grinded surface (c) Electrical grinder

Figure 3-27: Surface preparation of RC beams.

3.3.2. Mechanical fastening strategy. Before fixing the AA plates to the RC

specimens, the spacing and diameter of each hole was marked on the concrete specimen

and AA plate according to the dimensions shown in both Figure 3-8 and Figure 3-9.

Each AA plate was drilled with holes spaced at different lengths as shown in Figure 3-

28 where the diameter of each hole was dependent on the diameter of the anchors;

mainly, to avoid uneven fixtures and achieve ideal load transfer within the anchorage

system [79]. Therefore, an HST3 M10 anchor required a 12 mm diameter hole and an

HST3 M12 required a 14 mm hole as shown in Figure 3-28. Similarly, the concrete

specimens were marked with the same spacing and diameters as shown in Figure 3-29

in which the embedment depths used were 65 mm and 80 mm for the HST3 M10 and

HST3 M12 bolts, respectively, as shown in Figure 3-30.

45

75 mm 100 mm D12/D14 mm

50 mm

1350 mm

(a) BEM10H/BEM12H and BM10H/BM12H specimens

200 mm D12/D14 mm 75 mm

50 mm

1350 mm

(b) BEM10L/BEM12L specimens

100 mm

75 mm D12/D14 mm

50 mm

1350 mm

(c) BEM10E/BEM12E specimens

Figure 3-28: Bolt location markings on AA plates.

RC Beam Soffit

1840 mm

320 mm 100 mm

125 mm

1350 mm

D12/D14 mm

AA Plate Location

(a) BEM10H/BEM12H and BM10H/BM12H specimens

RC Beam Soffit

1840 mm

320 mm 200 mm

125 mm

1350 mm

D12/D14 mm

AA Plate Location

(b) BEM10L/BEM12L specimens



RC Beam Soffit

1840 mm

320 mm 100 mm

125 mm

1350 mm

AA Plate Location D12/D14 mm

(c) BEM10E/BEM12E specimens

Figure 3-29: Bolt location markings on concrete specimens.

3.3.3. Setting instructions for HST3 bolts. Hilti's technical datasheet [79]

offers instructions on how to mechanically fasten HST3 expansion anchors.

Figure 3-

31 shows these steps during the strengthening application.

46

Side View of RC Specimen

240 mm

65 mm

AA Plate HST3 M10 Bolt

(a) HST3 M10

Side View of RC Specimen

240 mm

80 mm

AA Plate HST3 M12 Bolt

(b) HST3 M12

Figure 3-30: Bolt embedment depth for each model.

Setting instructions

\*For detailed information on installation see instruction for use given with the package of the product

Setting instruction for HST3, HST3-BW, HST3-R, HST3-R-BW

Hammer drilling (M8, M10, M12, M16, M20, M24)

1. Drill the hole 2. Clean the hole

3a. Insert the anchor with hammer 3a. Insert the anchor with setting tool HS-SC

4. Check 5a. Torque with calibrated torque wrench (M8-M24)

5b. Torque with impact wrench with Adaptive torque module (M8-M12)

Figure 3-31: Setting instruction for HST3 expansion anchors [79].

3.3.4. Final specimens. The aforementioned preparation techniques were in-

corporated on the RC beams whereby 15 specimens were strengthened using differ-

Hollow Drill Bit (M16, M20, M24), no cleaning required

ent anchor. r agDreill tshye shtoelem wisth. Tthhe Heoslelows dpreillc

biitmens wer2ea. cInasetert gthoe rainzcehodr wiintht oham3mgerr oups;

namely, CB-

Specimens, M10-Specimens, and M12-Specimens. The tested parameters were

depth

47

2b. Insert the anchor with setting tool HS-SC 3. Check

9 Updated: Apr-18

and spacing of bolts with the presence or absence of adhesive resin

(epoxy) as shown in

Figure 3-32. For brevity, a picture of each specimen, depending on its anchorage sys-

tem, is shown. For example, Figure 3-32a shows BEM10E specimen, which consists of the same bolt arrangement as the BEM12E, but with HST3 M12 anchors. Ultimately, these specimens were subjected to a displacement controlled test in which a displacement rate of 2mm/min was employed using a four-point bending configuration, as shown in Figure 3-33, using the Universal Test Machine (UTM).  
(a) BEM10E/BEM12E (b) BEM10H/BEM12H (c) BEM10L/BEM12L  
(d) BM10H/BM12H (e) CBE

Figure 3-32: Final strengthened specimens.

48

Load

Loading plates

a = 600 mm a = 600 mm

240 mm

1740 mm

1840 mm

Support Plates

Figure 3-33: Loading scheme of specimens.

49

#### Chapter 4. Results and Discussions

The work presented in this chapter aims at studying the structural and mechanical behavior of all the specimens tested in this project. Several curves like the load versus deflection and load versus strain curves were generated to graphically simulate each specimen's stiffness, ductility, and capacity during testing. Furthermore, the failure mode of each specimen was captured and presented by means of a photograph in which each photograph was supported by monitoring strain measurements during each experiment.

##### 4.1. Response and Behaviour of Each Specimen

The load versus deflection and load versus strain curves were highlighted during this section, whereby an in-depth exploration of the specimens' structural and mechanical responses was graphically captured. For brevity, the strain gauge of each element was abbreviated as SG followed by the element of interest. For instance, the strain gauge of concrete was abbreviated as SG Concrete. Moreover, the parameters reported herein were: load at yielding of bottom reinforcement ( $P_{steel,y}$ ), load at yielding of AA plate ( $P_{AA,y}$ ), load at crushing of concrete ( $P_{conc,cr}$ ), ultimate load of each specimen ( $P_{ult}$ ), load at failure of section ( $P_{fail}$ ), deflection at yielding of bottom reinforcement

( $\delta_{steel,y}$ ), deflection at yielding of AA plate ( $\delta_{AA,y}$ ), deflection at crushing of concrete ( $\delta_{conc,cr}$ ), deflection corresponding to ultimate load ( $\delta_{ult}$ ), and deflection at failure of section ( $\delta_{fail}$ ).

Owing to the vast amount of points obtained from both the strain gauge and

UTM loading machine, the strain measurements of each element corresponding to the ultimate load were drawn adjacent to the section of interest. This granted insight into the mechanical contribution of each element to the flexural capacity of the specimen. In general, structural engineers would try to achieve crushing of concrete with the yielding of steel to fully utilize the mechanical properties of the reinforcement. In this project, the yield strains of both the AA plates and the steel reinforcement were taken from the average experimental results shown in Table 3-5, Table 3-6, and Table 3-7. Therefore, the yield strains of the AA plates ( $\epsilon_{ya}$ ) and steel reinforcement ( $\epsilon_{ys}$ ) were taken as 0.0034 and 0.0027, respectively, while the strain at which concrete crushes ( $\epsilon_{cc}$ ) was

50

taken as -0.003. The signs in the strain values correspond to the type of stress whereby a positive strain indicates tension and negative strain indicates compression.

4.1.1. CB-Specimens. As previously mentioned, this project consisted of two reference RC specimens, mainly: CB and CBE. CB is the unstrengthened RC beam and CBE is the RC beam externally bonded with an AA plate. Both of these beams were tested under a four-point bending configuration in which a displacement rate of 2mm/min was subjected until both concrete sections reached failure. It is worth mentioning that failure, in the scope of this project, is defined as a 10-15% drop in the ultimate load demonstrated in the load versus deflection curves.

4.1.1.1. CB. The unstrengthened RC specimen (CB) failed in flexure in which both steel yielding and concrete crushing occurred during the test. Figure 4-34 shows the load versus deflection and load versus strain curves whereby the UTM machine and strain gauges were able to capture an extensive amount of points during the testing phase. As a result, the ultimate loading capacity of CB achieved a value of 64.2 kN

at 17.4 mm whereby the test was stopped when a 10% drop in the ultimate load was noticed, 57.7 kN at 30.51 mm. Using both curves in Figure 4-34a and Figure 4-34b, the loads at both yielding of steel and crushing of concrete were recorded as 53.2 kN at 6.77 mm and 63.6 kN at 17.8 mm, respectively. Figure 4-34c shows the strain measurements corresponding to the ultimate load where the strain in steel reached a value of 0.0136 and the strain in concrete reach -0.0023. It is worth mentioning that the strain in concrete should, theoretically, reach a value -0.003 to visibly exhibit crushing. However, the strain gauge was damaged due to spalling of concrete.

4.1.1.2. CBE. The RC specimen epoxy-bonded with an AA plate (CBE) failed by cover separation in which the epoxy-bonded AA plate ripped some of the concrete cover, exposing the steel reinforcement. It was observed, from the strain measurements, that yielding occurred in both steel reinforcement and AA plate, and crushing occurred in the top concrete fibers of the beam during the test. Figure 4-35 shows the load versus deflection and load versus strain curves whereby the UTM machine and strain gauges were able to capture an extensive amount of points during the testing phase. As a result,

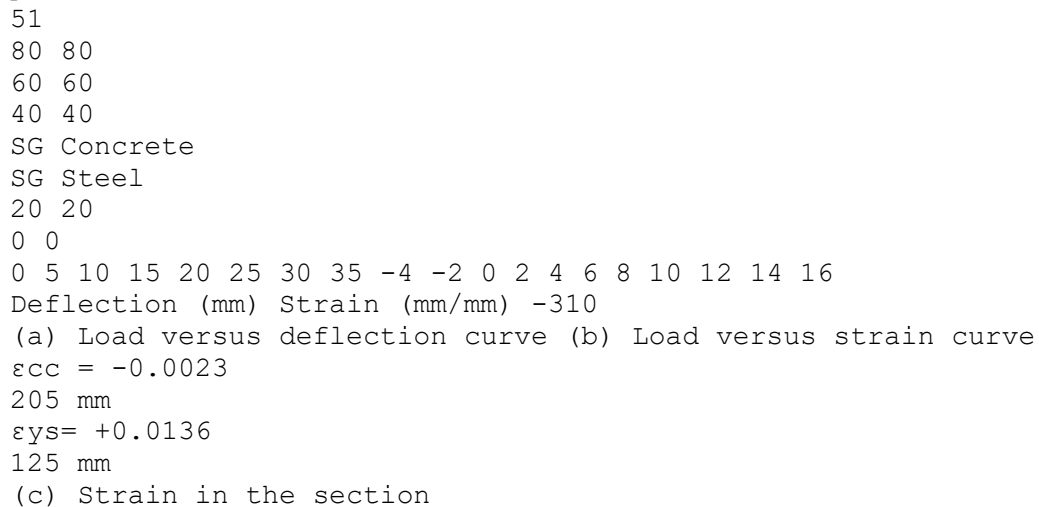


Figure 4-34: Load, deflection and strain for CB at mid-span. CBE achieved a peak load value of 84.4 kN at 14.3 mm followed by a large drop in loading capacity at 19.94 mm, due to cover separation. Using both curves in Figure 4-35a and Figure 4-35b, the loads at which yielding occurred in both the steel reinforcement and the AA Plate were 65.1 kN at 6.62 mm and 72.2 kN at 7.56 mm, respectively,

whereas the load at the crushing of concrete was 83.9 kN at 14.1 mm. Figure 4-35c shows the strain measurements corresponding to the ultimate load where the strain values in both the steel reinforcement and the AA plate reached 0.00431 and 0.00495, respectively, and the strain in concrete reached -0.00301. The close proximity of the strain values in both the steel and the plate indicate that the test immediately failed, approximately, around the ultimate loading capacity of the section.

4.1.2. M10-Specimens. Seven RC specimens externally strengthened with AA plates by means of bolting, using HST3 M10 expansion anchors, with/without adhesive bonding were loaded until failure. Each specimen included a replica of itself except

52

Load (kN)

Load (kN)

100 100

80 80

60 60

40 40

SG Concrete

20 20 SG AA Plate

SG Steel

0 0

0 5 10 15 20 -4 -2 0 2 4 6

Deflection (mm) Strain (mm/mm) -310

(a) Load versus deflection curve (b) Load versus strain curve

125 mm  $\epsilon_{cc} = -0.00301$

205 mm

$\epsilon_{ys} = +0.00431$

50 mm  $\epsilon_{ya} = +0.00495$

(c) Strain distribution in section

Figure 4-35: Load, deflection and strain for CBE at mid-span. for specimen BEM10E, which granted the author insight into the consistency of the

results corresponding to each strengthened specimen's unique anchorage system. Fur-

thermore, these beams were tested under a four-point bending configuration in which a

displacement rate of 2mm/min was subjected until failure by means of plate rupture or

IC debonding occurred.

4.1.2.1. BEM10L. The first two RC specimens that were bolted at 200 mm, center-to-center spacing, and bonded with AA plates (BEM10L-1 and BEM10L-2)

failed by rupture of the plates. Their sections' ultimate loading capacities were achieved

as a result of the yielding in both steel reinforcement and AA plates, and crushing in the

top concrete fibers. Figure 4-36 shows the load versus deflection and load versus strain

curves, whereby the UTM machine and strain gauges were able to capture an extensive amount of points during the testing phase. It is worth noting that the load versus strain curve for BEM10L-1 was unable to record the strain measurements within the steel

53

Load (kN)

Load (kN)

reinforcement due to the damage of the strain gauge during testing. As a result, the ultimate loading capacities of BEM10L-1 and BEM10L-2 were 80 kN at 16 mm and

85.8 kN and 17.1 mm, respectively. The loading, then, experienced a slight but negli-

ble drop where it plateaued until both specimens, BEM10L-1 and BEM10L-2, reached

failure loads of 76.2 kN at 25 mm and 78 kN at 24.4 mm, respectively.

Afterwards, both

specimens experienced a large drop in their ultimate loading capacities due to rupture

of their AA plates. Using the curves in Figure 4-36a and Figure 4-36b, the mechani-

cal behavior of BEM10L-1 was studied in which the loads at yielding of AA plate and

crushing of concrete were 69.6 kN at 7.6 mm and 79.8 kN at 14.8 mm, respectively.

However, BEM10L-2 exhibited yielding in both its steel reinforcement and the its AA

plate at 67.5 kN at 7.06 mm and 80.1 kN at 10.4 mm, respectively, and experienced

concrete crushing at 85 kN at 17.5 mm as shown in Figure 4-36a and Figure 4-36c.

Figure 4-36d shows the strain measurements corresponding to the ultimate load where

the strain values in both the steel reinforcement and the AA plate reached 0.00413 and

0.00803, respectively, and the strain in concrete reach -0.00301. A diagram pertaining

the strain distribution of BEM10L-1's section was not drawn due to the loss of strain

gauge data its steel reinforcement.

4.1.2.2. BEM10H. Similarly, the two plated RC specimens that were anchored

with the same bolt model, but spaced at 100 mm and bonded using the same adhe-

sive (BEM10H-1 and BEM10H-2) also failed by rupture of the plates. Their sections'

ultimate loading capacities were achieved as a result of the yielding in both steel re-

inforcement and AA plates, and crushing occurred in the top concrete fibers of both

beams during the test. Figure 4-37 shows the load versus deflection and load versus

strain curves, whereby the UTM machine and strain gauges were able to capture an extensive amount of points during the testing phase. As a result, the ultimate load-carrying capacities of BEM10H-1 and BEM10H-2 were 80.5 kN at 15.6 mm and 86.5 kN at 18.5 mm, respectively. The loading, then, experienced a slight but negligible drop where it plateaued until both strengthened specimens, BEM10H-1 and BEM10H-2, reached failure loads of 76.5 kN at 29.4 mm and 80 kN at 26.9 mm, respectively. Afterwards, both specimens experienced a large drop in their ultimate loading capacities

54

100 100

80 80

60 60

BEM10L-1

40 BEM10L-2 40 SG Concrete

SG AA Plate

20 20

0 0

0 10 20 30 -4 -2 0 2 4 6 8

Deflection (mm) Strain (mm/mm)  $-3 \times 10$

(a) Load versus deflection curve (b) Load versus strain curve for BEM10L-1

100

80

60

SG Concrete

40 SG AA Plate

SG Steel 125 mm  $\epsilon_{cc} = -0.00298$

20

205 mm

0  $\epsilon_{ys} = +0.00413$

-4 -2 0 2 4 6 8

Strain (mm/mm)  $-3 \times 10$  50 mm  $\epsilon_{ya} = +0.00803$

(c) Load versus strain curve for BEM10L-2 (d) Strain in Section BEM10L-2

Figure 4-36: Load, deflection and strain for BEM10L specimens at mid-span.

due to rupture of their AA plates. Using the curves in Figure 4-37a and Figure 4-37b,

the mechanical behavior of BEM10H-1 was studied in which the loads at yielding of

both the steel reinforcement and the AA plate were 72.8 kN at 8.23 mm and 80.3 kN

at 16.5 mm, respectively, and the load at crushing of concrete was 80.32 kN at 16.2

mm. However, BEM10H-2 exhibited yielding in both its steel reinforcement and the its

AA plate at 67.5 kN at 7.1 mm and 80.1 kN at 10.4 mm, respectively, and experienced

concrete crushing at 84.7 kN at 19 mm as shown in Figure 4-37a and Figure 4-37c.

Figure 4-37d shows the strain distribution in BEM10H-1 where the strain values corresponding to the ultimate load in both the steel reinforcement and the AA plate reached

0.00598 and 0.00623, respectively, and the strain in concrete reached -0.00403. This indicated that yielding occurred in both the steel reinforcement and the plate, and crushing occurred in concrete. Similarly, yielding in both internal and external reinforcements

55

Load (kN) Load (kN)

Load (kN)

occurred whereby their strain values corresponding to the ultimate load were 0.00501

and 0.00695, respectively, and concrete crushing occurred at a strain of -0.00358.

100 100

80 80

60 BEM10H-1 60

BEM10H-2

40 40 SG Concrete

SG AA Plate

SG Steel

20 20

0 0

0 10 20 30 -4 -2 0 2 4 6 8

Deflection (mm) Strain (mm/mm)  $-3 \times 10$

(a) Load versus deflection curve (b) Load versus strain curves for BEM10H-1

100

80

60

SG Concrete

40 SG AA Plate

SG Steel 125 mm  $\epsilon_{cc} = -0.00403$

20

205 mm

0

-4 -2 0 2 4 6 8  $\epsilon_{ys} = +0.00598$

Strain (mm/mm)  $-3 \times 10$  50 mm  $\epsilon_{ya} = +0.00623$

(c) Load versus strain curves for BEM10H-2 (d) Strain in section BEM10H-1 125 mm  $\epsilon_{cc} = -0.00358$

205 mm

$\epsilon_{ys} = +0.00501$

50 mm  $\epsilon_{ya} = +0.00695$

(e) Strain in section BEM10H-2

Figure 4-37: Load, deflection and strain for BEM10H specimens at mid-span.

4.1.2.3. BM10H. The two RC specimens that were only bolted at a spacing of 100 mm center-to-center (BM10H-1 and BM10H-2) also failed by rupture of the



plates; however, only BM10H-1's ultimate loading capacities was achieved as a result

56

Load (kN) Load (kN)

Load (kN)

of the yielding in both the steel reinforcement and AA plates, and crushing in concrete,

whereas BM10H-2 only exhibited yielding in steel and crushing in concrete. Figure 4-

38 shows the load versus deflection and load versus strain curves, whereby the UTM

machine and strain gauges were able to capture an extensive amount of points during the

testing phase. As a result, the ultimate loading capacities of BM10H-1 and BM10H-2

were 74.4 kN at 16.4 mm and 79.5 kN and 22 mm, respectively. The load versus de-

flection curve for BM10H-1 experienced a slight drop and exhibited a linear increase

until it reached a failure load of 73.5 kN at 32.7 mm followed by a substantial drop in

the load; indicating plate rupture as shown in Figure 4-38a. Similarly, the load versus

deflection curve of BM10H-2 experienced a slight drop until a load value of 74.1 kN

at 25.9 mm as shown in Figure 4-38a. However, the curve suddenly dropped due to

rupture of the plate. Using the curves in Figure 4-38a and Figure 4-38b, the mechani-

cal behavior of BM10H-1 was studied in which the loads at yielding of both the steel

reinforcement and the AA plate were 56.5 kN at 6.9 mm and 72.7 kN at 14 mm, respec-

tively, and the load at crushing of concrete was 74.1 kN at 22.2 mm. On the other hand,

BM10H-2 exhibited yielding only in the steel reinforcement at a load of 59.9 kN at

7.45 mm and crushing of concrete at 79 kN at 22.3 mm, whereas the AA plate's did not

undergo yielding where the strain at ultimate load was 0.00224 as shown in Figure 4-

38a and Figure 4-38c. Figure 4-38d shows the strain distribution in BM10H-1 where the

strain values corresponding to the ultimate load in both the steel reinforcement and the

AA plate reached 0.00596 and 0.00651, respectively, and the strain in concrete reach

-0.00322. This indicated that yielding occurred in both the steel reinforcement and the

plate, and crushing occurred in concrete. However, as mentioned previously, BM10H-2

did not experience AA plate yielding at its ultimate load; mainly, only the steel yielding

occurred, +0.00318, accompanied with slight crushing in concrete crushing, -0.00278, as shown in Figure 4-38e.

4.1.2.4. BEM10E. The last RC specimen that was bolted with a spacing of 100 mm, at its ends, and bonded with epoxy (BEM10E) failed by intermediate debonding, whereby its ultimate loading capacity was achieved as a result of the yielding in both its steel reinforcement and its AA plate, and crushing occurred in the top concrete fibers

57

80 80

60 60

BM10H-1

40 BM10H-2 40 SG Concrete

SG AA Plate

SG Steel

20 20

0 0

0 10 20 30 40 -4 -2 0 2 4 6 8

Deflection (mm) Strain (mm/mm)  $\times 10^{-3}$

(a) Load versus deflection curve (b) Load versus strain curve for BM10H-1

80

60

40

SG Concrete

SG AA Plate 125 mm  $\epsilon_{cc} = -0.00322$

20 SG Steel

205 mm

0  $\epsilon_{ys} = +0.00596$

-4 -2 0 2 4

Strain (mm/mm)  $\times 10^{-3}$  50 mm  $\epsilon_{ya} = +0.00651$

(c) Load versus strain curve for BM10H-2 (d) Strain in section BM10H-1

125 mm  $\epsilon_{cc} = -0.00278$

205 mm

$\epsilon_{ys} = +0.00318$

50 mm  $\epsilon_{ya} = +0.00224$

(e) Strain in section BM10H-2

Figure 4-38: Load, deflection and strain of BM10H specimens at mid-span. during the test. Figure 4-39 shows the load versus deflection and load versus strain

curves, whereby the UTM machine and strain gauges were able to capture an extensive

amount of points during the testing phase. As a result, the ultimate loading capacity of

BEM10E was 82.6 kN at 14.9 mm, as shown in Figure 4-39a. Moreover, the load versus

deflection curve experienced a slight drop where it plateaued until it reached a failure

load of 74.3 kN at 24.8 mm, as shown in Figure 4-39a. Using the curves in Figure 4-

39a and Figure 4-39b, the mechanical behavior of BEM10H-1 was studied in which the

58

Load (kN) Load (kN)

Load (kN)

loads at yielding of both the steel reinforcement and the AA plate were 68.3 kN at 7.09

mm and 80.2 kN at 10.81 mm, respectively, and the load at crushing of concrete was

80.1 kN at 17.1 mm. Figure 4-39c shows the strain distribution in BEM10E where the

strain values corresponding to the ultimate load in both the steel reinforcement and the

AA plate reached 0.00398 and 0.00676, respectively, and the strain in concrete reach

-0.00308. This indicated that yielding occurred in both the steel reinforcement and the

plate, and crushing occurred in concrete.

100 100

80 80

60 60

40 40 SG Concrete

SG AA Plate

20 20 SG Steel

0 0

0 5 10 15 20 25 -4 -2 0 2 4 6 8

Deflection (mm) Strain (mm/mm) -310

(a) Load versus deflection curve (b) Load versus strain curve

125 mm  $\epsilon_{cc} = -0.00308$

205 mm

$\epsilon_{ys} = +0.00398$

50 mm  $\epsilon_{ya} = +0.00676$

(c) Strain in the section

Figure 4-39: Load, deflection and strain for BEM10E at mid-span.

4.1.3. M12-Specimens. The last seven RC specimens externally strengthened with AA plates by means of bolting, using HST3 M12 expansion anchors, with/without

adhesive bonding were loaded until failure. Each specimen included a replica of it-

self except for BEM12E, which granted the author insight on the consistency of the

results corresponding to each strengthened specimen's unique anchorage system. Fur-

thermore, these beams were tested under a four-point bending configuration in which a

59

Load (kN)

Load (kN)

displacement rate of 2mm/min was subjected until failure by means of plate rupture or

IC debonding occurred.

4.1.3.1. BEM12L. The first two RC specimens that were bolted at a spacing of

200 mm and bonded with AA plates (BEM12L-1 and BEM12L-2) failed by rupture of

plates, whereby their sections' ultimate loading capacities were achieved as a result of the yielding in both the steel reinforcement and AA plates, and crushing occurred in the top concrete fibers of both beams during the test. Figure 4-40 shows the load versus deflection and load versus strain curves, whereby the UTM machine and strain gauges were able to capture an extensive amount of points during the testing phase. As a result, the ultimate loading capacities of BEM12L-1 and BEM12L-2 were 78.1 kN at 16.1 mm and 86.4 kN and 16.5 mm, respectively. The loading, then, experienced a slight but negligible drop where it plateaued until both specimens, BEM12L-1 and BEM12L-2, reached failure loads of 72.7 kN at 24.6 mm and 79.6 kN at 25. mm, respectively. Afterwards, both specimens experienced a large drop in their ultimate loading capacities due to the rupture of the AA plates. Using the curves in Figure 4-40a and Figure 4-40b, the mechanical behavior of BEM12L-1 was studied in which the loads at yielding of both the steel reinforcement and the AA plate were 61.3 kN at 6.81 mm and 75.7 kN at 12.65 mm, respectively, and experienced concrete at a load of 77.4 kN at 16.3 mm. Similarly, BEM12L-2 exhibited yielding in both its steel reinforcement and the its AA plate at 68.8 kN at 6.69 mm and 81.8 kN at 10.9 mm, respectively, and demonstrated concrete crushing at 85.4 kN at 16.8 mm as shown in Figure 4-40a and Figure 4-40c. Figure 4-40d shows the strain measurements corresponding to the ultimate load where the strain values in both the steel reinforcement and the AA plate indicated yielding by reaching values of 0.00427 and 0.00484, respectively, and the strain in concrete showed crushing with a value of -0.00298. Similarly, Figure 4-40e shows the strain measurements corresponding to the ultimate load where the strain values in both the steel reinforcement and the AA plate indicated yielding by reaching values of 0.00594 and 0.00649, respectively, and the strain in concrete showed crushing with a value of -0.00367.

60

100 100

80 80

60 60

BEM12L-1 SG Concrete

BEM12L-2  
 40 40 SG AA Plate  
 SG Steel  
 20 20  
 0 0  
 0 10 20 30 -4 -2 0 2 4 6 8  
 Deflection (mm) Strain (mm/mm)  $-3 \times 10$   
 (a) Load versus deflection curve (b) Load versus strain curve for BEM12L-1  
 100  
 80  
 60  
 SG Concrete  
 40 SG AA Plate  
 SG Steel 125 mm cc = -0.00298  
 20  
 205 mm  
 0 ys= +0.00427  
 -4 -2 0 2 4 6 8  
 Strain (mm/mm) -310 50 mm ya= +0.00484  
 (c) Load versus strain curve for BEM12L-2 (d) Strain in section BEM12L-1  
 125 mm cc = -0.00367  
 205 mm  
 ys= +0.00594  
 50 mm ya= +0.00649  
 (e) Strain in section BEM12L-2

Figure 4-40: Load, deflection and strain of BEM12L specimens at mid-span. 4.1.3.2. BEM12H. Similarly, the two plated RC specimens that were bolted at

a spacing of 100 mm and bonded using the same adhesive (BEM12H-1 and BEM12H-2) also failed by rupture of plates, whereby their sections' ultimate loading capacities were achieved as a result of the yielding in both the steel reinforcement and AA plates, and crushing occurred in the top concrete fibers of both beams during the test. Figure 4-41 shows the load versus deflection and load versus strain curves, whereby the UTM machine and strain gauges were able to capture an extensive amount of points

61  
 Load (kN) Load (kN)  
 Load (kN)  
 during the testing phase. As a result, the ultimate loading capacities of BEM12H-1 and BEM12H-2 were 82.2 kN at 18.3 mm and 86.2 kN and 19.1 mm, respectively. The loading, then, experienced a slight but negligible drop where it plateaued until both specimens, BEM12H-1 and BEM12H-2, reached failure loads of 78.3 kN at 23.6 mm and 80.3 kN at 31.1 mm, respectively. Afterwards, both specimens experienced a large

drop in their ultimate loading capacities due to the rupture of the AA plates. Using the curves in Figure 4-41a and Figure 4-41b, the mechanical behavior of BEM12H-1 was studied in which the loads at yielding of both the steel reinforcement and the AA plate were 74.9 kN at 8.96 mm and 81.2 kN at 16.5 mm, respectively, and the load at crushing of concrete was 82.1 kN at 16.4 mm. Similarly, BEM12H-2 exhibited yielding in both its steel reinforcement and the its AA plate at 65.9 kN at 6.9 mm and 80.6 kN at 11.7 mm, respectively, and experienced concrete crushing at 86.1 kN at 19.3 mm as shown in Figure 4-41a and Figure 4-41c. Figure 4-41d shows the strain distribution in BEM12H-1 where the strain values corresponding to the ultimate load in both the steel reinforcement and the AA plate reached 0.00368 and 0.00584, respectively, and the strain in concrete reach -0.00326. This indicated that yielding occurred in both the steel reinforcement and the plate, and crushing occurred in concrete. Similarly, yielding in both internal and external reinforcements occurred whereby their strain values corresponding to the ultimate load were 0.00407 and 0.00586, respectively, and concrete crushing occurred at a strain of -0.00299.

4.1.3.3. BM12H. The two RC specimens that were only bolted at a spacing of 100 mm (BM12H-1 and BM12H-2) also failed by rupture of plates, whereby their sections' ultimate loading capacities were achieved as a result of the yielding in both the steel reinforcement and AA plates, and crushing in the concrete of both beams during the test. Figure 4-42 shows the load versus deflection and load versus strain curves, in which the UTM machine and strain gauges were able to capture an extensive amount of points during the testing phase. As a result, the ultimate loading capacities of BM12H-1 and BM12H-2 were 83.5 kN at 19.5 mm and 83.8 kN and 20.1 mm, respectively, followed by slight drops in the loading until their failure loads reached 79.5 kN at 26.1 mm and 78.9 kN at 28.7 mm, respectively, indicating plate rupture

62

100 100

80 80

60 60

SG Concrete

40 40 SG AA Plate

BEM12H-1 SG Steel  
 20 BEM12H-2 20  
 0 0  
 0 10 20 30 -4 -2 0 2 4 6 8  
 Deflection (mm) Strain (mm/mm)  $-3 \times 10$   
 (a) Load versus deflection curve (b) Load versus strain curve for BEM12H-1  
 100  
 80  
 60  
 40  
 SG Concrete 125 mm cc = -0.00326  
 SG AA Plate  
 20  
 SG Steel 205 mm  
 0 ys = +0.00368  
 -4 -2 0 2 4 6  
 Strain (mm/mm)  $-3 \times 10$  50 mm ya = +0.00584  
 (c) Load versus strain curve for BEM12H-2 (d) Strain in section BEM12H-1  
 125 mm  $\&$  cc = -0.00299  
 205 mm  
 $\&$  ys = +0.00407

50 mm  $\&$  ya = +0.00586

(e) Strain in section BEM12H-2

Figure 4-41: Load, deflection and strain of BEM12H specimens at mid-span. in both specimens, as shown in Figure 4-42a. Using the curves in Figure 4-42a and

Figure 4-42b, the mechanical behavior of BM12H-1 was studied in which the loads at

yielding of both the steel reinforcement and the AA plate were 64.9 kN at 7.17 mm and

81.7 kN at 16.7 mm, respectively, and the load at crushing of concrete was 83.2 kN at

20.1 mm. Similarly, BM12H-2 exhibited yielding in both the steel reinforcement and

the AA plate at loads of 57.8 kN at 5.95 mm and 83 kN at 18 mm, respectively, and

crushing of concrete occurred at a load of 83.4 kN at 20.3 mm as shown in Figure 4-

63

Load (kN) Load (kN)

Load (kN)

42a and Figure 4-42c. Figure 4-42d shows the strain distribution in BM12H-1 where the

strain values corresponding to the ultimate load in both the steel reinforcement and the

AA plate reached 0.00587 and 0.00545, respectively, and the strain in concrete reach

-0.00298. This indicated that yielding occurred in both the steel reinforcement and the

plate; however, it was observed that the strain in the plate was less than that of the re-

inforcement. An observation can be made in which the bolt holes were subjected to a concentrated flexural stress; thereby increasing the size of the hole and causing the bolt to demonstrate a rigid body rotation. This rigid body rotation was responsible for slightly damping the strain-effect in the AA plate. Moreover, BM12H-2 also experienced yielding in both the steel reinforcement and the AA plate at values of +0.00473 and +0.00424, respectively, and crushing in concrete at a strain of -0.00365. But owing to the large stress concentration in the holes, the bolt in BM12H-2 also experienced rigid body rotation in which the AA plate's strain-effect was slight damped as shown in Figure 4-42e.

4.1.3.4. BEM12E. The last RC specimen that was bolted with a spacing of 100 mm center-to-center, at its ends, and bonded with epoxy (BEM12E) failed by intermediate debonding, whereby its ultimate loading capacity was achieved as a result of the yielding in both its steel reinforcement and its AA plate, and crushing occurred in the top concrete fibers during the test. Figure 4-43 shows the load versus deflection and load versus strain curves, whereby the UTM machine and strain gauges were able to capture an extensive amount of points during the testing phase. As a result, the ultimate loading capacity of BEM12E was 86.1 kN at 21 mm, as shown in Figure 4-43a, followed by a slight drop in the load where it plateaued until it reached a failure load of 72.1 kN at 41 mm, as shown in Figure 4-43a. Using the curves in Figure 4-43a and Figure 4-39b, the mechanical behavior of BEM12E was studied in which the loads at yielding of both the steel reinforcement and the AA plate were 67.4 kN at 7.4 mm and 78.9 kN at 9.62 mm, respectively, and the load at crushing of concrete was 85.7 kN at 21.3 mm. Figure 4-43c shows the strain distribution in BEM12E where the strain values corresponding to the ultimate load in both the steel reinforcement and the AA plate reached 0.00559 and 0.00593, respectively, and the strain in concrete reach -0.00270.

64  
100 100  
80 80  
60 60  
40 40



BM12H-1 SG Concrete

BM12H-2

20 SG AA Plate

20 SG Steel

0 0

0 10 20 30 -4 -2 0 2 4 6

Deflection (mm) Strain (mm/mm)  $-3 \times 10$

(a) Load versus deflection curve (b) Load versus strain curve for BM12H-1

100

80

60

40

125 mm  $\curvearrowright$

SG Concrete  $cc = -0.00298$

20 SG AA Plate

SG Steel 205 mm

0

$\curvearrowright$   $ys = +0.00587$

-4 -2 0 2 4 6

Strain (mm/mm)  $-3$

$\curvearrowright$   $ya = +0.00545$

$\times 10$  50 mm

(c) Load versus strain curve for BM12H-2 (d) Strain in section BM12H-1

125 mm  $\curvearrowright$   $cc = -0.00365$

205 mm

$\curvearrowright$   $ys = +0.00473$

50 mm  $\curvearrowright$   $ya = +0.00424$

(e) Strain in section BM12H-2

Figure 4-42: Load, deflection and strain of BM12H specimens at mid-span.

This indicated that yielding occurred in both the steel reinforcement and

the plate, and

slight crushing occurred in concrete.

#### 4.2. Summary of Results and Remarks

The measured loads and deflections at different limit states were

tabulated in two

tables as shown in Table 4-9 and Table 4-10. It can be concluded that all

the strength-

ened specimens, despite the type of anchorage system, sustained a larger

load capacity

65

Load (kN) Load (kN)

Load (kN)

100 100

80 80

60 60

40 40

SG Concrete

20 20 SG AA Plate

SG Steel

0 0

0 10 20 30 40 -4 -2 0 2 4 6

Deflection (mm) Strain (mm/mm)  $-310$

(a) Load versus deflection curve (b) Load versus strain curve

125 mm

$\delta_c c = -0.00270$

205 mm

$\delta y s = +0.00559$

50 mm  $\delta y a = +0.00593$

(c) Strain in the section

Figure 4-43: Load, deflection and strain of BEM12E specimen at mid-span. than that of the reference specimens (CB). In addition, the degree of deformation, ductility, was also an underlying parameter that distinguished the bonded specimen (CBE)

with the specimens that are bolted with/without bonding (M10-Specimens and M12-

Specimens). This gave room to calculate the ductility index to monitor the effectiveness

of each anchorage system. Table 4-9: Summary of ultimate and failure limits in all specimens.

Table 4-9: Summary of ultimate and failure limits in all specimens.

Beam ID Pult(kN)  $\delta_{ult}$ (mm) Pfail(kN)  $\delta_{fail}$ (mm)

CB	64.2	17.4	57.7	30.5
CBE	84.4	14.3	84.4	19.94
BEM10L-1	80	16	76.2	25
BEM10L-2	85.8	17.1	78	24.4
BEM10H-1	80.5	15.6	76.5	29.4
BEM10H-2	86.5	18.5	80	26.5
BM10H-1	74.4	16.4	73.5	32.7
BM10H-2	79.5	22	74.1	25.9
BEM10E	82.6	14.9	74.3	24.8
BEM12L-1	78.1	16.1	72.7	24.6
BEM12L-2	86.4	16.5	79.6	25
BEM12H-1	82.2	18.3	78.3	23.6
BEM12H-2	86.2	19.1	80.3	31.3
BM12H-1	83.5	19.5	79.5	26.1
BM12H-2	83.8	20.1	78.9	28.7
BEM12E	86.1	21	72.1	41

66

Load (kN)

Load (kN)

Table 4-10: Summary of mechanical response of each element.

Beam ID P 1 1 2 2steel,y(kN)  $\delta_{steel,y}$ (mm) PAA,y(kN)  $\delta_{AA,y}$ (mm)

Pconc,cr(kN)  $\delta_{conc,cr}$ (mm)

CB	53.2	6.77	-	-	63.6	17.8
CBE	65.1	6.62	72.2	7.56	83.9	14.1
BEM10L-1	N.A	N.A	69.6	7.6	79.8	14.8
BEM10L-2	67.5	7.06	80.1	10.4	85	17.5
BEM10H-1	72.8	8.23	80.3	16.5	80.32	16.2
BEM10H-2	67.5	7.1	80.1	10.4	84.7	19
BM10H-1	56.5	6.9	72.7	14	74.1	22.2
BM10H-2	59.9	7.45	N.Y	N.Y	79	22.3
BEM10E	68.3	7.09	80.2	10.8	80.1	17.1
BEM12L-1	61.3	6.81	75.7	12.6	77.4	16.3
BEM12L-2	68.8	6.69	81.8	10.9	85.4	16.8
BEM12H-1	74.9	8.96	81.2	16.5	82.1	16.4

BEM12H-2 65.9 6.9 80.6 11.7 86.1 19.3

BM12H-1 64.9 7.17 81.7 16.7 83.2 20.1

BM12H-2 57.8 5.95 83 18 83.4 20.3

BEM12E 67.4 7.4 78.9 9.62 85.7 21.3

1 N.A: Strain gauge was damaged

2 N.Y: No yielding occurred

4.2.1. Effect of M10 bolts with/without bonding. The M10-Specimens were composed of RC beams that were strengthened, using AA plates, by implementing four unique anchorage configurations; namely, HST3 M10 bolts at 100 mm center-to-center

plus bonding (BEM10H), HST3 M10 bolts at 200 mm center-to-center plus bonding

(BEM10H), only HST3 M10 bolts at 100 mm center-to-center (BM10H), and HST3

M10 bolts at 100 mm center-to-center on the edges plus bonding (BEM10E). Their re-

sults were compared to the unstrengthened specimen (CB-Specimens) based on the load

versus deflection curves shown in Figure 4-44. As a result, it was observed that the im-

plementation of bolting HST3 M10 bolts and/or bonding AA plates to the soffits of RC

beams enhanced their flexural capacities when compared to an unstrengthened beam.

Moreover, the M10-Specimens group's load versus deflection curves demonstrated sim-

ilar profiles to the CB specimens, in terms of ductility, indicating a flexural response

rather than an immediate failure (i.e., debonding/delamination of the plate). The varying

parameters that impacted the flexural behavior of the specimens in the M10-Specimens

group were: the process of alternating between incorporating bolts with epoxy and in-

corporating epoxy alone. In this section, BM10H specimens showed a delay in strength

gain, roughly at 8 mm deflection, due to the plate-slip that occurred between the bolts

and their surrounding holes. Afterwards, the BM10H specimens' plates were bearing

on the bolts such that the beams' flexural stresses were transferred to the plates; re-

sulting in a lag in strain that is graphically emphasized in the load versus strain curves

67

shown in the previous sections. The BEM10E specimen continued to resist loads until

the deflection surpassed that of the CB specimens by, approximately, 3 mm followed

by intermediate debonding. This indicated that the un-bolted and bonded length, in

the maximum moment zone, demonstrated better stress transfer when compared to a

uniformly bolted plate; whereby the stresses were acting on the segmented plate length between each bolt. Ultimately, the M10-Specimens group's curves demonstrated load drops as a result of plate rupture or intermediate debonding, which will be discussed later in this report.

Furthermore, Figure 4-44 shows a bi-linear profile just before the sections begin to exhibit inelastic nature. This helped conclude the simultaneous contribution between the AA plate and steel reinforcement, despite the presence of the epoxy, in the load capacity of the RC beams. Afterwards, the curves reach the plastic stage in which both hardening and softening occur at the ultimate and failure loads, respectively. To quantify these observations, a table was developed in which the percentage increase in the load, at different stages, were calculated based on the results obtained from the CB-Specimens. These stages include the load at: (a) the ultimate state; (b) the failure state; (c) concrete crushing state; (d) steel yielding state; (e) AA plate yielding state. Table 4-11 shows the load increase, in the ultimate and failure states, of the M10-Specimens.

It is worth noting that the loads at failure were extracted based on the final point prior to immediate failure (rupture of plate). Furthermore, the maximum percentage increase in the ultimate and failure state took place with BEM10H-2 at 35% and 25% respectively, as shown in Table 4-11. This indicated that the incorporation of the AA plate contributed to a large increase in the specimen's flexural capacity. Moreover, the coefficient of variation (CV) was calculated to understand the degree of variation in the experimental results as a means to observe the pattern the strengthening configuration.

Equation 1 was used; where CV,  $\sigma$  and  $\mu$  are the coefficient of variation, standard deviation and mean of the dataset. As a result, the computed CV for the load increase in the ultimate and failure states were 22.3% and 18.3%; hence, degree of variation of the flexural capacity of each section are almost similar.

68

$$= \sigma CV \quad (1)$$

$\mu$

Table 4-12 shows the percentage load increase when crushing and yielding of

both steel reinforcement and AA plate occurred. Unlike the percentage increase shown in Table 4-11, the maximum percentage increase shown in Table 4-12 occurred for different specimens. For example, the maximum load increase at which crushing occurred was for BEM10L-2 at 34%, while the maximum load increase at which yielding in the steel reinforcement and the AA plate occurred was for BEM10H-1 at 37% and 11%, respectively. However, for M10-Specimens, the maximum load increase at which the AA plate yielded occurred for most of the specimens, which indicated ideal and consistent load transfer throughout the anchorage system imposed onto the external reinforcement. Figure 4-45 graphically summarizes the load percentage increase for each limit state; whereby ULS, FLS, CC, YS and YA stand for the load percentage increase during the ultimate load state, failure load state, concrete crushing, yielding of steel and yielding of AA plates, respectively. The bar chart demonstrated major improvements in the specimens' strength enhancements when HST3 M12 expansion anchors were used with epoxy, rather than using mechanical anchors alone. This helped conclude that the torque magnitudes, imposed by the manufacturer, combined with the shear stress distribution, between the surface area of the bolts and the concrete holes, formed a pre-tension loading-layout in the bolts; whereby the degree at which the AA plates settled into the epoxy was greater than that of the BM10H specimens without any adhesives. This controlled settlement subjected the epoxy with a normal stress and provided confinement in the cohesive layer (between the epoxy particles) such that the epoxy required larger shear stress to fail. This type of loading was maintained throughout the AA plates' span, due to the uniform bolting scheme, and helped enhance the epoxy's bond; thereby suppressing any internal cracks within the epoxy. Figure 4-44 shows this phenomenon when observing the gain in stiffness for the epoxy-filled beams in the M10-Specimens demonstrated a larger shift in the loading capacity before reaching the plastic stage, whereas the specimens that were bolted without using epoxy (BM10H) reached the plastic stage at a lower load. Another observation can be

69

made; whereby the spacing of bolts did not contribute to the strength enhancements when viewing BEM10L and BEM10H specimens in both Figure 4-44 and Figure 4-45.

100

80

60

CB

BEM10L-1

40 BEM10L-2

BEM10H-1

BEM10H-2

20 BM10H-1

BM10H-2

BEM10E

0

0 10 20 30 40

Deflection (mm)

Figure 4-44: Load versus deflection curves of CB compared to M10-Specimens.

Table 4-11: Strength increase in the ultimate and failure states for M10-Specimens.

Beam ID	Ultimate State Pult(kN)	State Increase (%)	Failure State Pfail(kN)	State Increase (%)
CB	64.2	-	57.7	-
BEM10L-1	80	25	76.2	19
BEM10L-2	85.8	34	78	21
BEM10H-1	80.5	25	76.5	19
BEM10H-2	86.5	35	80	25
BM10H-1	74.4	16	73.5	14
BM10H-2	79.5	24	74.1	15
BEM10E	82.6	29	74.3	16

Table 4-12: Strength increase when concrete crushing occurs and yielding in both steel

and AA plate for M12-Specimens.

Beam ID	P (kN)	Increase (%)	P (kN) <sup>1</sup>	Increase (%) <sup>1</sup>	P (kN) <sup>2</sup>	concr, steel, y
CB	63.6	-	53.2	-	72.2	-
BEM10L-1	79.8	25	N.A	N.A	69.6	-4
BEM10L-2	85	34	67.5	27	80.1	11
BEM10H-1	80.32	26	72.8	37	80.3	11
BEM10H-2	84.7	33	67.5	27	80.1	11
BM10H-1	74.1	17	56.5	6	72.7	1
BM10H-2	79	24	59.9	13	N.Y	N.Y
BEM10E	80.1	26	68.3	28	80.2	11

1 N.A: Strain gauge was damaged

2 N.Y: No yielding occurred

70

Load (kN)

140

120 ULS

FLS

CC

```

100 YS
YAA
80
60
40
20
0
L-
1
L-
2 -1 -2H H H-
1 -2 OE
10 10 10 10 0 0
H 1
EM
M
EM EM M M
1 M1 BEB B B BE B B
Beam ID

```

Figure 4-45: Bar plot of load comparisons for the M10-Specimens group.

4.2.2. Effect of M12 bolts with/without bonding. The M12-Specimens were composed of RC beams that were strengthened using four anchorage configurations; namely, HST3 M12 bolts at 100 mm center-to-center plus bonding (BEM12H), HST3 M12 bolts at 200 mm center-to-center plus bonding (BEM12H), only HST3 M12 bolts at 100 mm center-to-center (BM12H), and HST3 M12 bolts at 100 mm center-to-center on the edges plus bonding (BEM12E). Their results were compared to the unstrengthened specimens (CB-Specimens) based on the load versus deflection curves shown in Figure 4-46. As a result, it was observed that the implementation of bolting HST3 M12 bolts and/or bonding AA plates to the soffits of RC beams also enhanced their flexural capacities when compared to an unstrengthened beam. Moreover, the M12-Specimens group's load versus deflection followed a flexural loading profile, similar to the M10-Specimens group. Unlike the BM10H specimens, the BM12H specimens exhibited better interaction between the RC section and the plate; whereby the curves approximately resembled the flexural behaviour of the BEM12L and BEM12H specimens. Afterwards, the BM10H specimens' plates were bearing on the bolts such that the beams' flexural stresses were transferred to the plates; resulting in a lag in strain that is graphically emphasized in the load versus strain curves shown in the previous sections.

The BEM12E specimen continued to resist loads until the deflection surpassed that of

71

Percentage Increase in Load (%)

the CB specimens by, approximately, 10 mm followed by intermediate debonding. This

indicated that the un-bolted and bonded length, in the maximum moment zone, demon-

strated better stress transfer when compared to a uniformly bolted plate; whereby the

stresses were acting on the segmented plate length between each bolt.

Ultimately, the

M12-Specimens group's curves demonstrated load drops as a result of plate rupture or

intermediate debonding, which will be discussed later in this report.

Figure 4-46 also shows a bi-linear profile, before the beginning of the inelas-

tic stage, representing the contribution of both the internal and external reinforcements

during loading. Afterwards, the curves reached the plastic stage in which both hard-

ening and softening occurred at the ultimate and failure loads, respectively. To quan-

tify these observations, a table was developed in which the percentage increase in the

load, at different stages, were calculated based on the results obtained from the CB-

Specimens. Table 4-13 shows the load increase, in the ultimate and failure states, of the

M12-Specimens. The maximum percentage increase in the ultimate state took place for

BEM12L-2 at 35%, whereas the maximum percentage increase in the failure state took

place for BEM12H-2 at 39%, as shown in Table 4-13. Therefore, the CV was evalu-

ated for the load increase in the ultimate and failure states, and were reported as 14.1%

and 16.2%; hence, degree of variation of the flexural capacity of each section are much

closer than that of the M10-Specimens.

Table 4-14 shows the percentage load increase when crushing and yielding of

both steel reinforcement and AA plate took place in the M12-Specimens.

For exam-

ple, the maximum load increase at which crushing occurred was for both BEM12H-2

and BEM12E at 35%, while the maximum load increase at which yielding in the steel

reinforcement and the AA plate occurred was for BEM12H-1 and BM12H-2 at 41%

and 15%, respectively. Similar to the M12-Specimens, the variation of percentage load

increase when AA plate yielding took place is negligible. Figure 4-47 graphically sum-



marizes the load percentage increase for each limit state. Similar to Figure 4-45, the bar chart shows that most of the specimens, consisting of epoxy and bolts, have helped the RC section utilize its material's mechanical properties more than the specimens that consisted of anchors alone. However, the variation in strength enhancement is negligible since the change from HST3 M10 bolts to HST3 M12 bolts was accompa-

72  
 nied by an increase in the torque used to fix the plate. This increased the pre-tension force throughout the bolts, which caused the BM12H specimens' anchorage system to achieve the same shear strength capacity as the hybrid anchorage system in BEM12H, BEM12L and BEM12E specimens. It was, then, concluded that the shear stress required to overcome the friction between the plate and concrete, in the BM12H specimens, almost reached the shear stress required to overcome the epoxy's shear strength within the BEM12 specimens. Similar to the previous section, the spacing of bolts did not have an effect on the strength enhancements when viewing the BEM12L and BEM12H specimens.

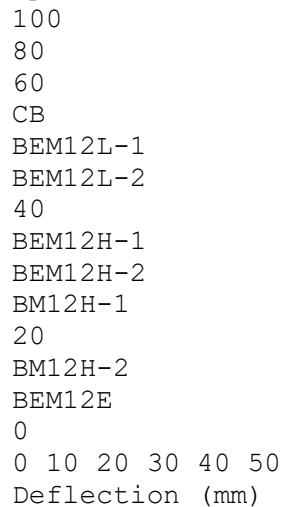


Figure 4-46: Load versus deflection curves of CB compared to M12-Specimens.

Table 4-13: Strength increase in the ultimate and failure states for M12-Specimens.

Beam ID	Ultimate State Pult(kN)	Ultimate State Increase (%)	Failure State Pfail(kN)	Failure State Increase (%)
CB	64.2	-	57.7	-
BEM12L-1	78.1	22	72.7	26
BEM12L-2	86.4	35	79.6	38
BEM12H-1	82.2	28	78.3	36

BEM12H-2 86.2 34 80.3 39  
 BM12H-1 83.5 30 79.5 38  
 BM12H-2 83.8 31 78.9 37  
 BEM12E 86.1 34 72.1 25

4.2.3. Effect of different bolt models at low-uniform spacing with bonding. This section aims at describing the effect of varying the torque magnitudes, at low

73

Load (kN)

Table 4-14: Strength increase when concrete crushing occurs and yielding in both steel

and AA plate for M12-Specimens.

Beam ID Pconc,cr(kN) Increase (%) Psteel,y(kN) Increase (%) PAA,y(kN) Increase (%)

CB 63.6 - 53.2 - 72.2 -  
 BEM12L-1 77.4 22 61.3 15 75.7 5  
 BEM12L-2 85.4 34 68.8 29 81.8 13  
 BEM12H-1 82.1 29 74.9 41 81.2 12  
 BEM12H-2 86.1 35 65.9 24 80.6 12  
 BM12H-1 83.2 31 64.9 22 81.7 13  
 BM12H-2 83.4 31 57.8 9 83 15  
 BEM12E 85.7 35 67.4 27 78.9 9

150

ULS

FLS

CC

YS

YAA

100

50

0

-1 -2 -1 -2 -1 -2L L 2E

12 12 H H H H 1M M M1

2

M1

2 12 12 MM M E

BE BE BBE BE B B

Beam ID

Figure 4-47: Bar plot of load comparisons for the M12-Specimens group. spacing, in the structural response of strengthened RC beams using different bolt mod-

els with adhesive bonding configurations. The results obtained were compared to the

unstrengthened specimens (CB-Specimens) based on the load versus deflection curves

shown in Figure 4-48. It was observed that the curves approximately demonstrate sim-

ilar profiles in which both BEM10H and BEM12H specimens exhibited higher load

capacities with relatively similar ductility when compared to CB. This was quantified

by computing the percentage increase for different states, similar to the previous sec-

tions. Table 4-15 shows the load increase, in the ultimate and failure states, between the BEM10H and BEM12H specimens. The maximum percentage increase in the ultimate state took place for BEM10H-2 at 35%, whereas the maximum percentage increase in the failure state took place for BEM10H-2 and BEM12H-2 at 39%, as shown in Table 4-74

Percentage Increase in Load (%)

15. Due to the small variation in the values, it is difficult to pinpoint which anchorage technique is superior. Therefore, the CV was evaluated for the load increase in the ultimate and failure states, and were reported as 7.21% and 13.1%, which reinforces this conclusion.

Table 4-16 shows the percentage load increase when crushing and yielding of both steel reinforcement and AA plate took place in both BEM10H and BEM12H.

For example, the maximum load increase at which crushing occurred was for both BEM12H-2 at 35%, while the maximum load increase at which yielding in the steel reinforcement and the AA plate occurred was for BEM12H-1 at 41% and 15%, respectively. Although the maximum percentage increase in terms of mechanical response occurred for the BEM12H specimens, it is still not sufficient enough to conclude whether BEM12H specimens are superior to the BEM10H ones. Figure 4-51 graphically summarizes the load percentage increase for each limit state, where maintaining the same spacing while changing from HST3 M10 bolts to HST3 M12 bolts, regardless of the presence of epoxy, slightly affected the strength enhancement in the RC beams.

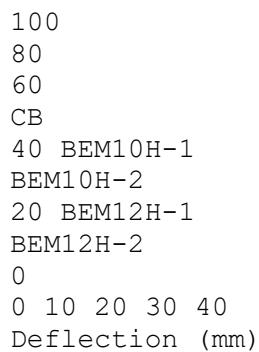


Figure 4-48: Load versus deflection curves for different bolt models at low-uniform spacing.

#### 4.2.4. Effect of different bolt models at high-uniform spacing with bond-

ing. This section aims at describing the effect of varying the torque magnitudes, at high spacing, on the structural response of strengthened RC beams using different bolt mod-  
75

Load (kN)

Table 4-15: Strength increase in the ultimate and failure states for different bolt models at low-uniform spacing.

Beam ID	Ultimate State	Failure State
Pult(kN)	Increase (%)	Pfail(kN) Increase (%)
CB	64.2 - 57.7 -	
BEM10H-1	80.5 25	76.5 33
BEM10H-2	86.5 35	80 39
BEM12H-1	82.2 28	78.3 36
BEM12H-2	86.2 34	80.3 39

Table 4-16: Strength increase at concrete crushing and yielding for different bolt models at low-uniform spacing.

Beam ID	Pconc,cr(kN)	Increase (%)	Psteel,y(kN)	Increase (%)	PAA,y(kN)
		Increase (%)			
CB	63.6 - 53.2 -	- - -			
BEM10H-1	80.32 26	72.8 37	80.3 11		
BEM10H-2	84.7 33	67.5 27	80.1 11		
BEM12H-1	82.1 29	74.9 41	81.2 12		
BEM12H-2	86.1 35	65.9 24	80.6 12		

150

100

ULS

FLS

CC

YS

50 YAA

0

H-

1 -2 1 2

0 0H H

- H-

M1 M1 M1

2 12

BE BE

M

BE BE

Beam ID

Figure 4-49: Bar plot of load comparisons.

els with adhesive bonding configurations. The results obtained were compared to the unstrengthened specimens (CB-Specimens) based on the load versus deflection curve

shown in Figure 4-50. It was observed that, in terms of strength performance, the

curves approximately demonstrate similar profiles; in which BEM10L and BEM12L

specimens exhibited higher load capacities with relatively similar ductility when compared to CB. This was quantified by computing the percentage increase for different states, similar to the previous sections. Table 4-17 shows the load increase, in the ultimate and failure states, between the BEM10H and BEM12H specimens. The maximum percentage increase in the ultimate and failure state took place for BEM12L-2 at 35% and 38%, respectively, as shown in Table 4-17. However, due to the small variation in the values, it is difficult to pinpoint which anchorage technique is superior. Therefore the CV was evaluated for the load increase in the ultimate and failure states, and were reported as 19.5% and 13.3%, which reinforces the consistency of the results.

Table 4-18 shows the percentage load increase when crushing and yielding of both steel reinforcement and AA plate took place in both BEM10H and BEM12H. For example, the maximum load increase at which crushing occurred was for both BEM12L-2 and BEM12L-2 at 34%, while the maximum load increase at which yielding in the steel reinforcement and the AA plate occurred was for BEM12L-2 at 29% and 13%, respectively. In general, it is observed that the maximum load increase in which crushing of concrete and yielding of both internal and external reinforcements occurred in the specimen. However, this does not warrant a sufficient conclusion about which anchorage configuration is superior to the other. Figure 4-51 graphically summarizes the load percentage increase for each limit state, where it can be observed that the BEM10L and BEM12L specimens, regardless of the presence of epoxy, did not impact the strength enhancements as much as the torque magnitudes.

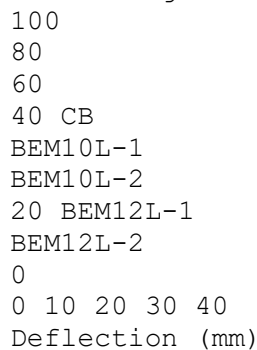


Figure 4-50: Load versus deflection curves for different bolt models at high-uniform spacing.

77

Load (kN)

Table 4-17: Strength increase in the ultimate and failure states for different bolt models at high-uniform spacing.

Beam ID	Ultimate State Pult(kN)	State Increase (%)	Failure State Pfail(kN)	State Increase (%)
CB	64.2	-	57.7	-
BEM10L-1	80	25	76.2	32
BEM10L-2	85.8	34	78	35
BEM12L-1	78.1	22	72.7	26
BEM12L-2	86.4	35	79.6	38

Table 4-18: Strength increase at concrete crushing and yielding for different bolt models at high-uniform spacing.

Beam ID	Pconc,cr(kN)	Increase (%)	Psteel,y(kN)	Increase (%)	PAA,y(kN)
CB	63.6	-	53.2	-	-
BEM10L-1	79.8	25	N.A	N.A	69.6 -4
BEM10L-2	85	34	67.5	27	80.1 11
BEM12L-1	77.4	22	61.3	15	75.7 5
BEM12L-2	85.4	34	68.8	29	81.8 13

150

ULS

FLS

CC

YS

100

YAA

50

0

-1 -2 -1L -

2

10 10

L 2L1 12

L

EM EM EM MB B B BE

Beam ID

Figure 4-51: Bar plot of load comparisons.

4.2.5. Effect of different bolt models at high-uniform spacing without bond-

ing. This section aims at describing the effect of varying the torque magnitudes, at high-uniform spacing, on the structural response of strengthened RC beams by means of alternating between two bolt models (HST3 M10 and HST3 M12) without using epoxy.

The results obtained were compared to the unstrengthened specimens (CB-Specimens)

based on the load versus deflection curve shown in Figure 4-52. It was observed that, in

## Percentage Increase in Load (%)

terms of strength performance, the curves approximately demonstrated similar profiles; in which BM10H and BEM12H specimens exhibited higher load capacities with relatively similar or larger ductility when compared to CB. This was quantified by computing the percentage increase for different states, similar to the previous sections. Table 4-19 shows the load increase, in the ultimate and failure states, between the BEM10E and BEM12E specimens. The maximum percentage increase in the ultimate state took place for BM12H-2 at 34%, whereas the failure state took place for BM12H-1 at 24%, as shown in Table 4-19. However, due to the small variation in the values, it is difficult to pinpoint which anchorage technique is superior. Therefore, the CV was evaluated for the load increase in the ultimate and failure states, and were reported as 2.33% and 2.34%, which reinforces the consistency of the results. Table 4-20 shows the percentage load increase when crushing and yielding of both steel reinforcement and AA plate took place in both BM10H and BM12H. For example, the maximum load increase at which crushing occurred was for both BM12H-1 and BM12H-2 at 31%, while the maximum load increase at which yielding, in the steel reinforcement and the AA plate, occurred was for BM12H-1 and BM12H-2 at 22% and 11%, respectively. In general, it is observed that the maximum load increase in which crushing of concrete and yielding of both internal and external reinforcements occurred in the specimen. However, this does not warrant a sufficient conclusion about which anchorage configuration is superior to the other. Figure 4-53 graphically summarizes the load percentage increase for each limit state, where it can be observed that the BM12H specimens demonstrated higher strength enhancements than the BM10H specimens. This supports the phenomenon that describes the effect large torque magnitudes possess in utilizing the high frictional shear strength between the concrete and plates.

Table 4-19: Strength increase in the ultimate and failure states for different bolt models at low-uniform spacing without bonding.

Beam ID	Ultimate State	Failure State
Pult(kN)	Increase (%)	Pfail(kN)
		Increase (%)

CB 64.2 - 57.7 -  
 BM10H-1 74.4 16 73.5 14  
 BM10H-2 79.5 24 74.1 15  
 BM12H-1 83.5 30 79.5 24  
 BM12H-2 83.8 31 78.9 23

79  
 100  
 80  
 60

CB  
 40 CBE  
 BM10H-1  
 BM10H-2  
 20  
 BM12H-1  
 BM12H-2

0  
 0 10 20 30 40  
 Deflection (mm)

Figure 4-52: Load versus deflection curves for different bolt models at low-uniform spacing without bonding.

Table 4-20: Strength increase at concrete crushing and yielding for different bolt models at low-uniform spacing without bonding.

Beam ID Pconc,cr(kN) Increase (%) Psteel,y(kN) Increase (%) PAA,y(kN) Increase (%)

CB 63.6 - 53.2 - - -  
 BM10H-1 74.1 17% 56.5 6% 72.7 1%  
 BM10H-2 79 24% 59.9 13% N.A N.A  
 BM12H-1 83.2 31% 64.9 22% 81.7 13%  
 BM12H-2 83.4 31% 57.8 9% 83 15%

120  
 ULS  
 100 FLS  
 CC  
 80 YS  
 YA  
 60  
 40  
 20  
 0

-1H H-  
 2 -1H H-  
 2  
 M1  
 0 0 2 2  
 B BM  
 1  
 BM  
 1 1  
 BM  
 Beam ID

Figure 4-53: Bar plot of load comparisons for BM10H and BM12H.



Ductility Index

Load (kN)

#### 4.2.6. Effect of different bolt models at the beams' ends with bonding.

This

section aims at describing the effect of varying the torque magnitudes, at the ends of

the beams, on the structural response of strengthened RC beams using different bolt

models with adhesive bonding configurations. The results obtained were compared

to the unstrengthened specimens (CB-Specimens) based on the load versus deflection

curve shown in Figure 4-54. It was observed that, in terms of strength performance, the

curves approximately demonstrate similar profiles; in which BEM10E and BEM12E

specimens exhibited higher load capacities with relatively similar or larger ductility

when compared to CB. This was quantified by computing the percentage increase for

different states, similar to the previous sections. Table 4-21 shows the load increase,

in the ultimate and failure states, between the BEM10E and BEM12E specimens. The

maximum percentage increase in the ultimate state took place for BEM12E at 34%,

whereas the failure state took place for BEM10E at 29%, as shown in Table 4-21.

However, due to the small variation in the values, it is difficult to pinpoint which an-

chorage technique is superior. In this section, the CV was not calculated due to the

small number of specimens for this comparison.

Table 4-22 shows the percentage load increase when crushing and yielding of

both steel reinforcement and AA plate took place in both BEM10E and BEM12E. For

example, the maximum load increase at which crushing occurred was for both BEM12E

at 34%, while the maximum load increase at which yielding in the steel reinforcement

and the AA plate occurred was for BEM10E at 28% and 11%, respectively. In general,

it is observed that the maximum load increase in which crushing of concrete and yield-

ing of both internal and external reinforcements occurred in the specimen. However,

this does not warrant a sufficient conclusion about which anchorage configuration is

superior to the other. Figure 4-55 graphically summarizes the load percentage increase

for each limit state, where it can be observed that the incorporation of HST3 M12, at

the beam's ends, performed slightly better than the beam with HST3 M10 bolted at its ends (BEM10E).

81  
100  
80  
60  
40 CB  
CBE  
20 BEM10E  
BEM12E  
0  
0 10 20 30 40 50

Deflection (mm)

Figure 4-54: Load versus deflection curves for different bolt models at edge of beams.

Table 4-21: Strength increase in the ultimate and failure states for different bolt models at high-non-uniform spacing.

Beam ID	Ultimate State Pult(kN)	State Failure Increase (%)	State Failure Pfail(kN)	State Failure Increase (%)
CB	64.2	-	57.7	-
BEM10E	82.6	29	74.3	29
BEM12E	86.1	34	72.1	25

Table 4-22: Strength increase at concrete crushing and yielding for different bolt models at ends of beams.

Beam ID	Pconc,cr(kN)	Increase (%)	Psteel,y(kN)	Increase (%)	PAA,y(kN)	Increase (%)
CB	63.6	-	53.2	-	-	-
BEM10E	80.1	26	68.3	28	80.2	11
BEM12E	85.7	35	67.4	27	78.9	9

#### 4.3. Failure Modes

Another characteristic structural engineers observe is the failure mode of the structural member after ultimate load conditions were achieved. In this project, the failure modes were characterized as: (a) end-debonding/delamination (ED); (b) intermediate debonding/delamination (ID); (c) Plate Rupture (PR); (d) Flexural Failure (FF). In the previous sections, these failure modes were addressed by analyzing the strain measurements in the elements of interest by means of load versus strain curves. However, in this section, the failure modes were identified by means of observing the crack patterns at failure or at a 15% drop in the ultimate load, in cases of FF.

82  
Load (kN)  
140  
120  
100  
ULS

FLS  
80 CC  
YS  
60 YAA  
40  
20  
0  
E E  
10 12  
BE  
M EMB  
Beam ID

Figure 4-55: Bar plot of load comparisons.

4.3.1. CB-Specimens. The CB-Specimens group was used as a benchmark to measure the differences between EBR systems versus retrofit systems that are anchored

using expansion anchors with/without adhesive bonding (epoxy). The group consisted

of an unstrengthened RC beam (CB), which was designed to fail in flexure, and a

strengthened RC beam by externally bonding an AA plate to its soffit (CBE), which

was designed to fail by debonding/delamination. Figure 4-56 shows the failure modes

after the CB-Specimens group failed; whereby CB failed typically in FF, as shown in

Figure 4-56a, and CBE failed by ED, as shown in Figure 4-56b.

(a) FF for CB (b) ED failure for CBE

Figure 4-56: Failure modes of CB-Specimens.

83

Percentage Increase in Load (%)

4.3.2. M10-Specimens. The M10-Specimens group was composed of strengthened RC beams that were varied by alternating between the spacing and position of

HST3 M10 bolts with/without the addition of epoxy. Both BM10H specimens (BM10H-

1 and BM10H-2) failed by PR while demonstrating obvious cracking patterns, as shown

in Figure 4-57; indicating concrete crushing combined with steel yielding. Similarly,

the BEM10H and BEM10L specimens also failed by PR while exhibiting crack patterns,

as shown in Figure 4-58 and Figure 4-59, whereas BEM10E failed by ID, as shown in

Figure 4-60. As a result, all of the strengthened specimens in M10-Specimens group ex-

hibited obvious cracking behavior, which indicated the large deflection imposed on the

specimen. These physical evidences are in close agreement with the mechanical prop-

erties provided by the strain measurements, in the previous sections; whereby the order

at which the elements reached their own capacities were expressed based on the time

recorded by the element's strain gauge. All M10-Specimens exhibited steel yielding followed by concrete crushing until failure was reached.

4.3.3. M12-Specimens. The M12-Specimens group was also composed of strength-ened RC beams that were varied by alternating between the spacing and position. However, these specimens were bolted using HST3 M10 bolts with/without the addition of epoxy. Both BM12H specimens (BM12H-1 and BM12H-2) failed by PR while demonstrating obvious cracking patterns, as shown in Figure 4-61; indicating concrete crushing combined with steel yielding. Similarly, the BEM12H and BEM12L specimens also failed by PR while exhibiting crack patterns, as shown in Figure 4-62 and Figure 4-63, whereas BEM12E failed by ID, as shown in Figure 4-64. As a result, all of the strength-ened specimens in M10-Specimens group exhibited obvious cracking behavior, which indicated the large deflection imposed on the specimen. These physical evidences are in close agreement with the mechanical properties provided by the strain measurements, in the previous sections; whereby the order at which the elements reached their own capacities were expressed based on the time recorded by the element's strain gauge. All M12-Specimens exhibited steel yielding followed by concrete crushing until failure was reached. Table 4-23 summarizes the failure modes presented in this section where the failure modes were listed in order of.

84

(a) Side view of BM10H-1's crack pattern (b) PR failure for BM10H-1  
(c) Side view of BM10H-2's crack pattern (d) PR failure for BM10H-2  
Figure 4-57: Failure modes of BM10H specimens.

Table 4-23: Summary of ultimate load and failure modes.

Beam ID PP (kN) ultult Failure Modes1Pult,CB

CB 64.2 - SY, CC

CBE 84.4 1.31 SY, CC, ED

BEM10L-1 80 1.25 SY, CC, PR

BEM10L-2 85.8 1.34 SY, CC, PR

BEM10H-1 80.5 1.25 SY, CC, PR

BEM10H-2 86.5 1.35 SY, CC, PR

BM10H-1 74.4 1.16 SY, CC, PR

BM10H-2 79.5 1.24 SY, CC, PR

BEM10E 82.6 1.29 SY, CC, ID

BEM12L-1 78.1 1.22 SY, CC, PR

BEM12L-2 86.4 1.35 SY, CC, PR

BEM12H-1 82.2 1.28 SY, CC, PR

BEM12H-2 86.2 1.34 SY, CC, PR

BM12H-1 83.5 1.30 SY, CC, PR

BM12H-2 83.8 1.31 SY, CC, PR  
BEM12E 86.1 1.34 SY, CC, ID  
1 S.Y: Steel yielding; C.C: Concrete Crushing

85

(a) Side view of BEM10H-1's crack pattern (b) PR failure for BEM10H-1  
(c) Side view of BEM10H-2's crack pattern (d) PR failure for BEM10H-2  
Figure 4-58: Failure modes of BEM10H specimens.

#### 4.4. Ductility Index

In addition to monitoring the ultimate loading capacity of each specimen, the

strength enhancement was characterized by measuring the ductility of each beam. This

was performed by evaluating the ductility index of each specimen in which two equa-

tions were used for this purpose; namely, the ratio of the deflection at ultimate load to

the deflection at yield and the deflection at failure load to the deflection at yield. How-

ever, in this project, there are two yield points experienced by the strengthened beams -

mainly deflection in which steel yielded and deflection at which the AA plate yielded.

The modulus of elasticity in the AA plate is far less than the modulus of elasticity in

the steel reinforcement; whereby, the flexural stiffness of the RC beams' is mainly orig-

inating from their steel reinforcements. Therefore, the deflection at steel yielding was

used when computing ductility index. Equation 2 and Equation 3 were used to compute

86

(a) Side view of BEM10L-1's crack pattern (b) PR failure for BEM10L-1  
(c) Side view of BEM10L-2's crack pattern (d) PR failure for BEM10L-2

Figure 4-59: Failure modes of BEM10L specimens.

(a) Side view of BEM10E's crack pattern (b) ID failure for BEM10E

Figure 4-60: Failure modes of BEM10E.

87

(a) Side view of BM12H-1's crack pattern (b) PR failure for BM12H-1

(c) Side view of BM12H-2's crack pattern (d) PR failure for BM12H-2

Figure 4-61: Failure modes of BM12H specimens.

the ductility indices, where  $\mu_{\Delta,ult}$  and  $\mu_{\Delta,fail}$  represent the ductility index at ultimate

and failure conditions, respectively. Table 4-24 summarizes the ductility index at failure

and ultimate conditions, respectively, for each specimen. It can be observed that most

of the specimens exhibited positive increase in ductility in which the negative values

are almost within a 10% margin.

The ductility achieved by the M10-Specimens surpassed the ductility of the CBE

specimen; whereby the CBE exhibited the lowest ductility index as shown in Figure 4-

65. Furthermore, the BEM10H specimens experienced larger ductility index values during failure than both the BEM10L and BEM10E specimens. This extra deformation allowed the specimens in the M10-Specimens group to delay the loading process and distribute the internal forces to each element; concrete, steel and AA plate. Similarly,

88

(a) Side view of BEM12H-1's crack pattern (b) PR failure for BEM12H-1  
 (c) Side view of BEM12H-2's crack pattern (d) PR failure for BEM12H-2  
 Figure 4-62: Failure modes of BEM12H specimens.

the ductility index values for strengthened specimens in the M12-Specimens group surpassed that of the CBE specimen, as shown in Figure 4-66. Some of the specimens in the M12-Specimens group managed to exhibit more ductility than the unstrengthened RC beam (CB); like BEM12H-2 and BEM12E. This extra deformation could be the result of the larger magnitude imposed by the HST3 M12 bolts; however, further testing is required to warrant such a conclusion.

$\delta_{ult}$

$$\mu\Delta_{ult} = (2)\delta_{steel,y} \\ = \delta_{fail}\mu\Delta_{fail} (3)\delta_{steel,y}$$

89

(a) Side view of BEM12L-1's crack pattern (b) PR failure for BEM12L-1  
 (c) Side view of BEM12L-2's crack pattern (d) PR failure for BEM12L-2  
 Figure 4-63: Failure modes of BEM12L specimens.

(a) Side view of BEM12E's crack pattern (b) ID failure for BEM12E  
 Figure 4-64: Failure modes of BEM12E.

90

Table 4-24: Summary of deflections and ductility indices for each specimen.

$\delta \quad \delta \quad \delta \quad \mu \quad \mu$

Beam ID ult fail steel,y  $\Delta_{ult}$   $\Delta_{fail}$ (mm) (mm) (mm)1  $\mu\Delta_{ult}$  % Change CBE  
 (%)  $\mu\Delta_{fail}$  % Change CBE (%)

CB	17.4	30.5	6.77	2.57	-	4.51	-
CBE	14.3	19.94	6.62	2.16	0	3.01	0
BEM10L-1	16	25	N.A	N.A	N.A	N.A	N.A
BEM10L-2	17.1	24.4	7.06	2.42	12.04	3.46	15
BEM10H-1	15.6	29.4	8.23	1.9	-12.04	3.57	18.6
BEM10H-2	18.5	26.5	7.1	2.61	20.8	3.73	23.9
BM10H-1	16.4	32.7	6.9	2.38	10.2	4.74	57.5
BM10H-2	22	25.9	7.45	2.95	36.6	3.48	15.6
BEM10E	14.9	24.8	7.09	2.1	-2.78	3.5	16.3
BEM12L-1	16.1	24.6	6.81	2.36	9.26	3.61	19.9
BEM12L-2	16.5	25	6.69	2.47	14.4	3.74	24.3
BEM12H-1	18.3	23.6	8.96	2.04	-5.56	2.63	-12.6
BEM12H-2	19.1	31.3	6.9	2.77	28.2	4.54	50.8
BM12H-1	19.5	26.1	7.17	2.72	25.9	3.64	20.9
BM12H-2	20.1	28.7	5.95	3.38	56.5	4.82	60.1
BEM12E	21	41	7.4	2.84	31.5	5.54	84.1

1 N.A: Not available due to damage in equipment

8

,ult

,fail

6

4

2

0

CB BE -2 1 2 1 2C 0L H

- H- - - 0

E

1 10 10 10

H

10

H 1

EM E

M

B BE

M EMB B

M BM B

Beam ID

Figure 4-65: Bar plot of ductility index for M10-Specimens group.

8 ,ult

,fail

6

4

2

0

CB BE -1L L-

2

H-

1 -2 1 2 E

C 12 12 H H

- H- 12

M M M1

2

M1

2 12 12 EM

BE BE BE BE B

M BM B

Beam ID

Figure 4-66: Bar plot of ductility index for M12-Specimens group

91

Ductility Index Ductility Index

Chapter 5. Nonlinear Finite Element Modelling

An important step required to gain a stronger understanding on how structural

members behave, is to reproduce the experimental results using a commercial finite

element (FE) software. This chapter aims at developing 3D nonlinear FE models using

Mechanical ANSYS APDL [41]. By adopting approaches conducted in previous studies

[82,83], an accurate model can be developed with the nonlinear properties of the tested specimens coupled with a simplified geometry. Afterwards, the load-stiffness response plots were extracted from the FE models and compared with the experimental results to help validate the FE models. These validated FE models were used to generate contour plots that express the stress and strain propagation in each individual element. Finally, a comprehensive summary of the results was developed to conclude this approach.

#### 5.1. Geometry of FE Models

The FE models were developed to accurately resemble the geometric configuration and dimensions of the tested specimens. Owing to the symmetry in the cross section and span, as shown in Figure 3-7 - Figure 3-9, a quarter of the model was created by restraining longitudinal and transverse translations of the beams, as shown in Figure 5-67. This helped simplify the analysis and reduce excessive computation time periods. The steel reinforcing bars were modelled using 3D spar elements, whereas the rest of the elements were modelled using 3D solid elements. Further emphasis regarding the element description will be discussed in the following sections.

#### Axis of Symmetry

Rollers Rollers

240 mm

920 mm 62.5 mm

Figure 5-67: Quarter model of RC beam

#### 5.2. Element Types and Material Properties

In general, a total of six elements were used to model the specimens in this

project: (a) SOLID65 for concrete; (b) SOLID185 for loading and supporting plates,

92

epoxy and AA plates; (c) LINK180 for steel reinforcements; (d) INTER205 for interfa-

cial cohesive bond between AA plate and concrete; (E) CONTA174 and TARGE170 for

simulating hard contact between AA plate and concrete without epoxy. The properties

and characteristics of each element will be discussed in the following subsections.

5.2.1. SOLID65. The concrete beam was modelled using SOLID65 elements to simulate cracking and compression when subjected to bending [84, 85]. The SOLID65

element, shown in Figure 5-68, consists of eight nodes having three degrees of freedom,

per node, in which translations are permitted in the nodal x, y, and z directions. The



assumptions and restrictions of the element are listed below [41]:

- Cracking is enabled in each orthogonal directions at the element's integration points.
- Upon the occurrence of concrete cracks, the elements are re-structured such that the material properties are tweaked to simulate hardening and softening behaviors in concrete.
- The concrete material is assumed to be initially isotropic.
- The reinforcements embedded within the concrete are assumed to be smeared throughout its elements.

Figure 5-68: Geometry of SOLID65 element [41].

93

In order to simulate the nonlinear effect of concrete, the tensile stresses and compressive stresses, in concrete, were incorporated using previously derived constitutive models. This granted the concrete model the capabilities of exhibiting both strain hardening and softening during each loading frame; thereby allowing the concrete elements to dissipate energy and experience stiffness decay after reaching their maximum tensile and compressive stresses [41]. In this study, the Hognestad Parabola was implemented to incorporate concrete compression and the William and Wanke model was implemented to simulate tensile cracking [84, 85]. Equation 4 was used to build the compressive stress-strain profile of the concrete elements, where  $f_c$  is the compressive stress,  $f'_{cc}$  is the average cylinder compressive

strength from Table 3-4 (taken as 37 MPa),  $\epsilon_c$  is the concrete strain ratio,  $\epsilon = 2f_{cc}/E$  is the strain corresponding to  $f'_{cc}$ ,  $\epsilon_{cu}$  is the crushing strain (taken as 0.0038 [82]) and  $E_c$  is the modulus of elasticity in concrete. The Young's Modulus of Elasticity in concrete ( $E_c$ ) was evaluated using the ACI 318-14 standard [75] as shown in Equation 5.

Figure 5-

69a shows the compressive stress response that was employed within the SOLID65 elements.

[ ( )<sup>2</sup>]

$f_c =$

$2f'_{cc} \epsilon_c$

$f'_{cc} - , \text{ for } 0 < \epsilon_c \leq \epsilon_{cu} \quad (4) \quad \epsilon_{co} \quad \epsilon_{co}$

$\sqrt$

$E_c = 4700 f'_{cc} \quad (5)$

The tensile behavior of concrete was modelled using five strength parameters )

imposed by the William and Wranke model [85]: uniaxial tensile strength  $f_t = 0.62 f'_{cc}$ , uniaxial compressive strength ( $f'_{cc}$ ), biaxial compressive strength ( $f_{cb}$ ), compressive strength for a state of biaxial compression superimposed on hydrostatic stress state ( $f_1$ ), and uniaxial compression superimposed on hydrostatic stress state ( $f_2$ ). The uniaxial compressive strength was obtained from experimental testing, and the last three parameters ( $f_{cb}$ ,  $f_1$  and  $f_2$ ) were taken as their default values,  $1.2f'$ ,  $1.45f'$  and  $1.725f'_{cc}$ , respectively. In addition, the open and closed shear coefficients were employed to suc-

94  
 cessfully measure the amount of energy dissipated when the SOLID65 elements begin to crack. Their values were taken as 0.2 and 0.5, respectively [82, 83, 86].

The tensile stress-strain relationship was constructed using Equation 6, where

Figure 5-69b shows the tensile stress response of the SOLID65 elements. The tensile

response in concrete was modeled as linear-elastic until the concrete tensile strength

( $f_t$ ) was reached. Afterwards, a relaxation in the tensile stress is exhibited by a 40%

drop in the concrete tensile stress, followed by an inversely linear decay until a tensile

stress value of zero was reached at a strain value greater than or equal equal to 6 times

the strain value corresponding to maximum concrete's tensile strength ( $\epsilon_{to}$ ) [41, 83].

Both constitutive models represent an idealized form of concrete, in both compression

and tension, such that these adopted models were capable of approximating the non-

linearity of concrete while accelerating convergence during the analysis.

$$\begin{aligned}
 & \sigma = f_t, \text{ if } 0 < \epsilon < \epsilon_{to} \\
 & \sigma = 0.6f_t, \text{ if } \epsilon_{to} = \epsilon \\
 & \sigma = -0.6f_t \left( \frac{\epsilon - \epsilon_{to}}{\epsilon_{to}} \right), \text{ if } \epsilon_{to} < \epsilon \leq 6\epsilon_{to}
 \end{aligned}
 \tag{6}$$

40 4  
 $f'_{c} f_t$

30 3  
 40% Sudden Relaxation

20 2

$\sigma$   
 $\epsilon$   
 0 0  
 0 1 2  $\epsilon_{co}$  3  $\epsilon_{cu}$  4 0 2 4 6 8  
 Strain (mm/mm)  $\times 10^{-3}$  Strain (mm/mm)  $10^{-4}$   
 (a) Compressive stress strain curve (b) Tensile stress-strain curve

Figure 5-69: Idealized stress-strain curves for concrete.

5.2.2. LINK180. The steel reinforcing bars were modelled as LINK180 3D spar elements to simulate the flexural response of the internal reinforcement. The LINK180

95

Stress (MPa)

Stress (MPa)

element functions as a two-node uniaxial tension/compression member with three degrees of freedom, per node, in which translations are permitted in the three directions (x, y, and z). The limitation and restrictions imposed by LINK180 element are [41]:

1. The spar element resembles a truss bar that is axially loaded, at its ends, and consists of both section and material property definitions.
2. The displacement shape function implies a uniform stress in the spar. The material definitions that were used to model the mechanical behavior of the steel reinforcements were linear and nonlinear definitions. The linear properties were defined an isotropic definition with a Young's Modulus of 200 GPa and a poisson ratio of 0.3. The nonlinear properties were defined using a Kinematic Hardening Plasticity definition that incorporated a Bilinear approximation of the tensile stress-strain curve of the steel reinforcement; thus, yielding an elastic perfectly plastic curve, based on the von misses yield criteria [41], as shown in Figure 5-71. The yield stress was obtained from the tensile test in which an average value of 550 MPa was used. Figure 5-70: Geometry of LINK180 element [41].

5.2.3. SOLID185. The loading and supporting plates, AA plates, bolts and epoxy were modelled as SOLID185 due to its plasticity and stress stiffening capabilities. The SOLID185 element is defined as an 8 node solid with three degrees of freedom, per node, in which translation is permitted in all three directions (x, y, and z), as shown in Figure 5-72. The loading and supporting plates were modelled using only an elastic-isotropic properties in which the Young's modulus of elasticity was 200 GPa

and the poisson ratio was 0.3. This allowed the plates to demonstrate rigidity during

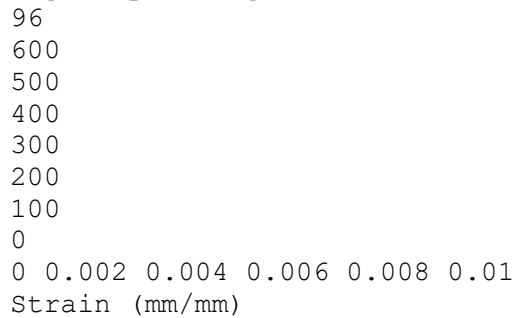
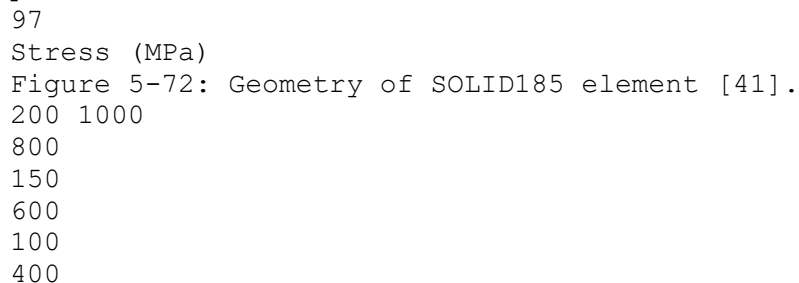


Figure 5-71: ElasticPerfectly plastic stress-strain curve loading. However, the AA plate and bolts were modelled using both an elastic-isotropic property and a Kinematic Hardening Plasticity with a Bi-linear definition. The Young's modulus of elasticity and poisson ratio for the AA plate was 50000 MPa and 0.33, respectively, whereas the modulus of elasticity and poisson ratio for the bolts were 200 GPa and 0.3, respectively. In addition, the yield stresses of the AA plates and bolts were 150 and 800 MPa, respectively, as shown in Figure 5-73. Finally, the Young's modulus of elasticity and poisson ratio of the epoxy was taken as 10000 MPa and 0.35, similar to a study conducted by Abu-Obeidah et. al [82].

5.2.4. INTER205. One of the difficulties researchers face, when modelling strengthened RC members, is the simulation of the adhesive interface that links the composite material and its adjacent host during the analysis. Several numerical studies were conducted in FE applications focused primarily on retrofit applications [82, 86] in which fracture or delamination, along the composite material, played a major role in limiting the stiffness and ductility of the strengthened structure. In this study, the epoxy was modelled using INTER205 elements where a cohesive zone material (CZM) model was employed to incorporate this interfacial bond [41]. INTER205 is a shell element consisting of eight nodes defined with three degrees of freedom, per node, in



50 200  
 0  
 0  
 0 0.002 0.004 0.006 0.008 0.01 0 0.005 0.01  
 Strain (mm/mm) Strain (mm/mm)

(a) AA plate (b) Bolts

Figure 5-73: Idealized tensile stress-strain curves.

which translation is permitted in all three directions (x, y, and z directions), as shown in

Figure 5-74.

The CZM model is a function of the traction and the slip between the strength-ening material and its host. It requires a bond stress-slip model which induces fracture mechanisms, within the INTER205 elements, leading to softening followed by a release

98

Stress (MPa)  
 Stress (MPa)

Figure 5-74: Geometry of INTER205 element [41].

of fracture energy release from within these elements. In this project, the bond stress-slip relationship presented by Lu et al. [87] was adopted using Equation 7, in which a

curve was generated, as shown in Figure 5-75. The curve demonstrates an increase in

shear stress with the increase in slip, whereby hardening is exhibited until a maximum

shear stress is reached,  $s_0$ . Afterwards, the curve shows an exponential decay simulat-

ing the instantaneous loss in shear strength combined with simultaneous debonding of

the elements until a failure slip is reached. The failure slip was assumed to equal four

times the value of  $s_0$ .

$\tau = \tau_{max} \left( \frac{s}{s_0} \right)^{\alpha}$  if  $s \leq s_0$

$\tau = 0$

0

(7)

$\tau = \tau_{max} \left( \frac{s}{s_0} \right)^{-\alpha}$

if  $s > s_0$

where

$\tau_{max} = \beta \sqrt{b}$

$\tau_{max} = 1.25 \beta \sqrt{b}$

$\tau_{max} = 1.25 \beta \sqrt{b}$

$\tau_{max} = 1.25 \beta \sqrt{b}$

$\tau_{max} = 1.25 \beta \sqrt{b}$

$\tau_{max} = 1.25 \beta \sqrt{b}$

$\tau_{max} = 1.25 \beta \sqrt{b}$

99

$s_0 = 0.0195 \beta^2 w f t$

$\sqrt{G_f}$

$G_f = 0.308 \beta^2 w f t$

$\alpha = 1 G_f^2$

$\tau_{maxS}$

-

0 3

where  $\beta_w$  is the width ratio factor,  $b_f$  = width of aluminum,  $b_c$  = is the width of the concrete (mm),  $\tau_{max}$  is the maximum local bond shear stress (MPa),  $s$  is the local slip corresponding to  $\tau_{max}$  (mm),  $G_f$  is the interfacial fracture energy (MPa),  $s$  is the local slip within the interface (mm),  $\alpha$  is a factor that depends on interfacial fracture energy, shear stress, and slip at  $\tau_{max}$  plate (mm).

6

$\tau_{max}$

5

4

3

2

1

S0 4S0

0

0 0.05 0.1 0.15 0.2 0.25 0.3 0.35 0.40

Slip (mm)

Figure 5-75: Bond stress-slip model at the interface between the aluminum and concrete elements.

5.2.5. TARGE170 and CONTA174. The BM10H and BM12H specimens were plated by fixing AA plates to RC members using different bolt models; thereby, mechanically fastening the plate onto a hard surface without the presence of any additional adhesive compound. This type of interaction was assumed to be in the form of a hard-contact with the presence of friction between the two surfaces of the adjacent structural solid elements. In ANSYS, this was simulated by assigning CONTA174 elements to the surfaces of the concrete elements and TARGE170 elements to the surfaces of the Aluminum elements. The CONTA174 elements are responsible for simulating both contact

100

Shear Stress (MPa)

and sliding interactions between the TARGE170 elements, as shown in Figure 5-76.

The target-contact interface was defined using a pair-base contact argument in which

both elements were assumed to behave in a flexible-flexible contact with a coefficient

of friction value of 0.3.

Figure 5-76: TARGE170 and CONTA174 surfaces [41].

### 5.3. Convergence Criterion

During displacement controlled loading, ANSYS automatically treats each user-defined displacement as a unit-step to evaluate the nodal stresses and strains within the element. The numerical solver used to help the model achieve convergence was the Newton-Raphson method where the solver iteratively reduces the time-step until a solution is found. Afterwards, it iterates to the next step where the numerical solver begins evaluating the problem until convergence is achieved. However, ANSYS requires a user-defined convergence tolerance to abide by; typically, this value would range between 0.05-0.2 [83]. Therefore, in this study, the force convergence tolerance limit value was 0.1.

101

### 5.4. Failure Criteria

The analysis of each model was stopped based on the type of failure exhibited.

In this study, the failure modes demonstrated during testing were: concrete crushing

(CC), plate rupture (PR), end-debonding (ED), and intermediate-crack debonding (IC).

These failure modes can be numerically distinguished by monitoring the stress and

strain propagation of each element. During the tests, all of the beams exhibited crushing

prior their unique failure modes. This helped define a criteria for which the analysis

should stop until crushing and one of the three latter imposed failure modes. These

three failure modes were detected based on:

1. Third principal strain contour in the concrete in which the range of crushing was

between 0.003-0.0043.

2. First principal stress contour in the AA plates at 150 MPa, as defined in Figure 5-

71.

3. Shear stress contour in the epoxy in which debonding occurred at shear stress

values of 5.8-6.1 MPa.

### 5.5. Modelling Techniques

As mentioned previously, the FE models were simulated by taking a quarter of the model and restraining any translation normal to the longitudinal and transverse

symmetry plane. All elements were meshed such that the nodes between each unique

element coincides with one another. This granted ideal load transfer across the nodes

and greatly reduced computation complexity. An FE model of the unstrengthened specimen, CB, was modelled such that the concrete, steel reinforcement, and plates were meshed and merged together as shown in Figure 5-77 and Figure 5-78. The mesh size was selected based on the aspect ratio of the element ( $\leq 2$ ) while satisfying the nodal coincidence between each adjacent elements. Therefore, the longitudinal and vertical lengths were meshed at 10 mm per segment while the transverse length was meshed at 5 mm per segment, as shown in Figure 5-77. The structural integrity of the FE model resembles that of a statically determinant beam; such that the external load coming from the plate will induce an equal and opposite reaction force on the support. Afterwards,

102

the simulation of the other strengthened beams consisted of this particular FE model combined with other 3D solid elements, some of which included: the epoxy, bolt and contact-target elements.

Transverse Restraints  
 Longitudinal Restraints  
 Supporting Plate with  
 Vertical Restraints  
 Concrete Beam

Figure 5-77: FE meshed geometry of CB specimen.

Top Steel Bar (†8 mm)  
 Stirrups (†8 mm)  
 Bottom Steel Bar (†10 mm)

Figure 5-78: FE meshed geometry of steel reinforcement.

103

The block volume command was used to model the epoxy, with a thickness of 2 mm, and the AA plate, with a thickness of 3 mm, whereby careful steps were taken to successfully simulate debonding/delamination between the AA plate and the concrete surface. This was accomplished by meshing the epoxy into PLATE185 elements while splitting the elements into top and bottom epoxy layers, as shown in Figure 6-146. INTER205 shell elements were assigned between the two adjacent layers using the CZMESH command whereby the CZM model, discussed in the previous section,



was incorporated within the assigned elements as shown in Figure 6-146. It is worth mentioning that the addition of INTER205 shell elements, between the epoxy layers, did not provide any additional stiffness or contribute to an increase in the moment-arm within the section, due to having no definite thickness.

Top Epoxy Layer Bottom Epoxy Layer  
INTER205 Shell Elements

Figure 5-79: Top and bottom meshed layers of epoxy. Since the thickness of the AA plate is relatively small compared to the size of the elements, the elements were segmented in the longitudinal and transverse directions, as shown in Figure 5-80. Afterwards the nodes residing on the top epoxy layer was merged onto the nodes of the bottom concrete surface, while the the nodes residing on the bottom epoxy layer was merged onto the nodes on the top surface of the AA plate. This helped relieve any computation issues regarding the adhesive interaction between the epoxy layers and their adjacent solid elements while focusing mainly on the cohesive definitions in the center of the epoxy layers.

104

(a) Front view (b) 3D Isometric view

Figure 5-80: AA Plate Meshed Elements.

On the other hand, the M10-Specimens and M12-Specimens groups were modelled differently due to the presence of bolts with/without epoxy. The bolts were modelled as semi-circular cylinders, for the bolts away from the center of the beam, and quarter-circular cylinder, for the bolts exactly in the middle of the beam span, because of the symmetry in the longitudinal and transverse planes, as shown in Figure 5-81. For the specimens that were composed of bolts without epoxy (BM10H and BM12H), they were modelled using contact-target elements such that the shear strength induced by the friction between the surfaces of the AA plate and concrete would contribute to the analysis of the FE models. Figure 5-82 shows the CONTA174 and TARGE170 assignments on the adjacent 3-D solid elements. Since the INTER205 elements require a certain type of mesh, involving the CZM argument, the remaining specimens that were plated using both bolts and epoxy were unable to be simulated due to the presence of

the PLATE185 elements (bolts) within the zone of the INTER205 elements. Therefore, a 20 mm gap was left such that the bolts were able to be merged within the concrete and AA plate while not interfering with the CZM command assigned within the INTER205 shell elements. Figure 5-83 shows the different modelling approaches taken when constructing the plated specimens; whereby the epoxy (shown in purple), the AA plate (shown in blue) and the bolts (shown in red) were created such that the locations of the bolts and the epoxy-gaps resembled the geometry of the tested specimens.

#### 5.6. Load Versus Deflection Curves

Several studies were focused on developing FE models, consisting of idealized material model definitions, whereby load versus deflection curves were generated to be compared and validated with those of the experiment [60, 83, 86]. In this section, the

105

Semi-Circular Cylinders  
Quarter-Circular Cylinder

Figure 5-81: Bolt elements shapes for a strengthened specimen with high number of bolts.

TARGE170 Elements (AA Plate)  
CONTA174 Elements (Concrete)

Figure 5-82: CONTA174 and TARGE170 element assignments. load versus deflection curves produced by ANSYS were plotted with the experimental results to gain insight on how accurate the FE models are in simulating the flexural be-

106

Bolt Locations  
Epoxy  
AA Plate

(a) BEM10H/BEM12H  
Bolt Locations  
Epoxy  
AA Plate

(b) BEM10L/BEM12L

Bolt Locations  
Epoxy  
AA Plate

(c) BEM10E/BEM12E

Figure 5-83: Epoxy and Bolt modelling for Plated Specimens.

107

havior of the tested specimens. It is worth mentioning that the softening stage of the

experimental results were cropped out due to the nonlinear elastic definition imposed

on the SOLID65 elements. Therefore, the predicted and experimental load versus de-

flexion curves, for each specimen, were plotted until the maximum load was achieved.

5.6.1. CB-Specimens. The load and deflection values were obtained from the

FE models, which resembled the beams in the CB-Specimens group, and were com-

pared to the results obtained from the experiment. Figure 5-84 shows the load versus de-

flexion curves of the unstrengthened RC beam, CB, and the strengthened beam that was

externally bonded with an AA plate, CBE. In general, both curves demonstrate small

deviations between curves of the FE models and the curves of the experiments. How-

ever, it was observed that both of the FE-produced curves demonstrated higher stiffness,

slopes, than that of the experiment; whereby the cause of this phenomenon originated

from the idealized assumption that the internal reinforcements are completely bonded

to the nodes of the concrete elements. This prevented any bond-slip action between

the bars and the concrete; thus, forcing the steel bars to fully dissipate energy in the

form of axial deformations coupled with bending rather than the combination of both

with the induced shear action resulting from the bar-slip. Moreover, the peak load and

corresponding deflection values demonstrated by the FE models for the CB and CBE

specimens were 60.2 kN at 17 mm and 84 kN at 13.8 mm, respectively, whereas peak

load and deflection values obtained from the experiment for the CB and CBE specimens

were 64.2 kN at 17.4 mm and 84.4 kN at 14.3 mm, respectively.

5.6.2. M10-Specimens. Similarly, the load versus deflection curves were gen-

erated using the FE models, resembling the beams in the M10-Specimens group, and

were plotted against the curves measured during the test. Figure 5-85 shows the load

versus deflection curves for the plated specimens fixed with HST3 M10 bolts in which the varying parameters were the addition of epoxy, the bolt spacing and layout. As a result, the FE models termed BEM10H, BEM10L, BM10H and BEM10E were capable of predicting peak load and corresponding deflection values of 80.9 kN at 15.1 mm, 82.7 kN at 16 mm, 72.8 kN at 16.2 mm and 83.8 kN at 13.9 mm, respectively, while the same experimental specimens yielded peak load and deflection values of 83.5 kN at 15.5 mm,

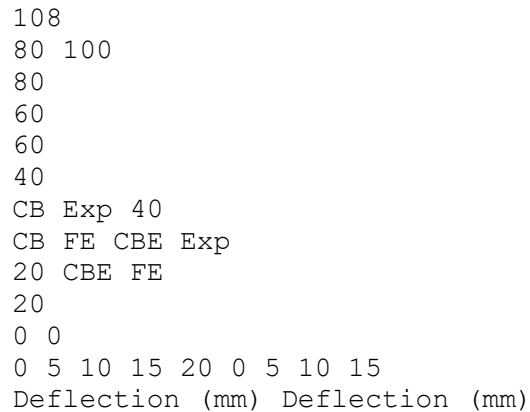


Figure 5-84: Load versus deflection curves between experimental and FE results for CB-Specimens.

82.9 kN at 16.5 mm, 76.9 kN at 17.1 mm and 82.6 kN at 14.9 mm, respectively. It is worth mentioning that most of the plated specimens within the M10-Specimens group were replicated twice; therefore, the load and deflection values were averaged and used

as a benchmark to compare against the results predicted by the FE model. 5.6.3. M12-Specimens. Finally, the load versus deflection curves were generated using the FE models, resembling the beams in the M12-Specimens group, and

were plotted against the curves measured during the test. Figure 5-86 shows the load versus deflection curves for the plated specimens fixed with HST3 M12 bolts in which

the varying parameters were the addition of epoxy, the bolt spacing and layout. As a result, the FE models termed BEM12H, BEM12L, BM12H and BEM12E were capable of predicting peak load and corresponding deflection values of 82.2 kN at 17.7 mm,

82.6 kN at 15.6 mm, 79.6 kN at 19.9 mm and 88.9 kN at 19.7 mm, respectively, while the same experimental specimens yielded peak load and deflection values of 84.2 kN at

18.7 mm, 82.2 kN at 16.3 mm, 83.6 kN at 19.9 mm and 86.1 kN at 21 mm, respectively.

Similar to the previous section, the mean values of the load and deflection results used as a benchmark to compare against the results predicted by the FE model.

5.6.4. Summary of results. The FE models were capable of predicting the load and deflection values within a reasonable range of the experiment. Table 5-25 shows a table that outlines the peak load and corresponding deflection values for the specimen

109

Load (kN)

Load (kN)

100 100

80 80

60 60

BEM10H-1 Exp BEM10L-1 Exp

40 BEM10H-2 Exp 40 BEM10L-2 Exp

BEM10H FE BEM10L FE

20 20

0 0

0 5 10 15 20 25 0 5 10 15 20 25

Deflection (mm) Deflection (mm)

(a) BEM10H (b) BEM10L

100 100

80 80

60 60

BM10H-1 Exp BEM10E Exp

40 BM10H-2 Exp 40 BEM10E FE

BM10H FE

20 20

0 0

0 5 10 15 20 25 0 5 10 15 20 25

Deflection (mm) Deflection (mm)

(c) BM10H (d) BEM10E

Figure 5-85: Load versus deflection curves between experimental and FE results for

M10-Specimens.

and corresponding FE model. It was observed that the FE software was capable of esti-

imating load and deflection for most of the specimens, of which, the absolute percentage

difference in the predictions were below 5%.

5.7. Predicted Contour Plots and Cracking Patterns

After validating the stiffness response of the previous FE models, contour plots

demonstrating the stress, strain and concrete crack propagation were generated and dis-

cussed during this section. The contour plots that were selected were the 1st Principal

stress, 3rd Principal strain, shear stress on the X-Z plane, and deflection plots. These

contour plots were used to assess the flexural behavior and ductility of each beam. The

110  
 Load (kN) Load (kN)  
 Load (kN) Load (kN)  
 100 100  
 80 80  
 60 60  
 BEM12H-1 Exp  
 BEM12L-1 Exp  
 BEM12H-2 Exp  
 40 BEM12H FE 40 BEM12L-2 Exp  
 BEM12L FE  
 20 20  
 0 0  
 0 5 10 15 20 25 0 5 10 15 20 25  
 Deflection (mm) Deflection (mm)  
 (a) BEM12H (b) BEM12L  
 100 100  
 80 80  
 60 60  
 BM12H-1 Exp BEM12E Exp  
 40 BM12H-2 Exp 40 BEM12E FE  
 BM12H FE  
 20 20  
 0 0  
 0 5 10 15 20 25 0 5 10 15 20 25  
 Deflection (mm) Deflection (mm)  
 (c) BM12H (d) BEM12E

Figure 5-86: Load versus deflection curves between experimental and FE results for M12-Specimens.

Table 5-25: Comparison between the FE predicted and experimental measured results

Failure Load (kN)	Maximum Deflection (mm)	Specimen	FE Model	% Difference		
CB FE	CB 64.2	60.2	6.23	17.4	17	2.30
CBE FE	CBE 84.4	84	0.47	14.3	13.8	3.50
BEM10H FE	BEM10H 83.5	80.9	3.11	15.5	15.1	2.58
BEM10L FE	BEM10L 82.9	82.7	0.24	16.5	16	3.03
BM10H FE	BM10H 76.9	72.8	5.33	17.1	16.2	5.26
BEM10E FE	BEM10E 82.6	83.8	1.45	14.9	13.9	6.71
BEM12H FE	BEM12H 84.2	82.2	2.38	18.7	17.7	5.35
BEM12L FE	BEM12L 82.2	82.6	0.49	16.3	15.6	4.29
BM12H FE	BM12H 83.6	79.6	4.78	19.9	19.9	0.00
BEM12E FE	BEM12E 86.1	88.9	3.25	21	19.7	6.19

111  
 Load (kN) Load (kN)  
 Load (kN) Load (kN)

concrete crack patterns were reproduced by switching on the cracking capabilities of the SOLID65 elements and allowing the concrete elements to exhibit crack/crushing in

the form of colored outlines. In general, ANSYS is capable of demonstrating the first, second and third cracks such that the order in which the cracks were induced followed a certain color scheme. The predicted cracks are located at the elements' integration points; whereby the first crack was denoted with a red circle outline, the second crack with a green outline, and the third crack with a blue outline [41]. Owing to the large number of figures that were generated during this analysis, three of the presented FE models were selected within this section, whereas the rest of the contour plots were appended at the end of the paper—labelled Appendix A through Appendix E.

5.7.1. CB. The un-strengthened RC beam model, CB, was selected as a reference model—to study the effects of implementing bolts and epoxy on the stress propagation and crack patterns. Figure 6-100 shows the predicted nodal deflection contour plots where it can be observed that the boundary conditions and loads, imposed on the model, are helping the model simulate bending. Moreover, the compression behavior of the concrete elements was assessed using the 3rd principal strain contour plot, as shown in Figure 5-88, in which the FE model roughly achieved the ultimate cylindrical compressive strength at an average strain of  $-0.00335$  at only the top 10-15 mm concrete layer, whereas the rest of the layers exhibited minimum tensile strains. The observed maximum compressive and minimum tensile stress values justify the constitutive models used during model development [84,85]. Refer to Appendix A through Appendix D to view the contour plots for specimen CBE. Figure 5-89 shows the predicted crack pattern of CB where the beam exhibited sequential cracking during the FE analysis. It was observed that most of the initiated cracks were represented as first cracks, colored red, where shear and flexural cracks coupled with crushing were plotted. This phenomenon is typical for RC beams that are designed against shear; hence, fail in flexure. Afterwards, the second crack, colored green, developed but less frequently followed by a third crack, colored blue. Refer to Appendix E to view the crack pattern of specimen CBE.

112

1NODAL SOLUTION

-17.0011

-14.9724  
-12.9437  
-10.9151  
-8.88638  
-6.85771  
MX  
-4.82904  
MN  
-2.80037  
-.771696  
1.25698

Figure 5-87: Predicted nodal vertical deflection for CB model.

-.006034  
-.005363  
-.004693  
-.004023  
MX  
-.003352  
-.002682  
MN  
-.002011  
-.001341

1 -.670E-03  
CRACKS AND CRUSHING  
STEP=.12492E-09  
SUB =24  
TIME=14.1988

Figure 5-88: Predicted nodal third principal strain for CB model.

Figure 5-89: Predicted crack patterns of the CB model.

5.7.2. BM10H. One of the specimens from the M10-Specimens group was se-

lected, BM10H, to observe the effect of using only bolts to fix the AA plate to the RC

beam. Figure 5-90 shows the predicted nodal deflection contour plots.

Figure 5-91

shows the 1st principal stress contour plot of the bolted AA plate, where the maximum

tensile stress occurred on the bolt at the end of the plate, 571.8 MPa, in which the bolt

was resisting the tendency of the AA plate from shearing and debonding/delaminating

off the concrete surface. In addition, the portion of the plate that is between the first 3

bolts, at mid-span of the beam, was subjected to a tensile stress concentration of 175.7

113

MPa. This gave room to support the justification mentioned in the experimental results

section in which the implementation of a large number of bolts, without using epoxy,



limited the contribution of the plate to only 200 mm, which is the distance between the first and third bolt located at mid-span of the model. Afterwards, a 37.5% stress decay was exhibited at the rest of the bolts until the plate began resisting compressive stress values of -22.3 MPa, near the last three bolts.

-21.536  
-18.9711  
-16.4062  
-13.8414  
-11.2765  
-8.71159  
MX  
-6.14671  
-3.58183 MN  
-1.01695  
1.54794

Figure 5-90: Predicted nodal vertical deflection for BM10H model.

1

-22.301  
43.7075 MMNX  
109.716  
175.725  
241.733  
307.742  
373.75  
439.759  
505.767

Stress Concentration at Bolt Locations (Leff). 571.776

Figure 5-91: Predicted nodal first principal stress for BM10H model.

114

Figure 5-92 shows the shear stress contour plot in the X-Z plane for the bolts

at the end of the plate. The reason for monitoring the shear stress propagation of the bolts located at the end of the plate is due to shearing-effect induced by the debonding/delamination phenomenon. It was observed that large shear stress was subjected

at the last three bolts in which the maximum shear stress, 87.04 MPa, occurred at the

third bolt from the edge of the plate, as shown in Figure 5-92. Since premature fail-

ure was avoided, the ultimate cylindrical compressive strength of the concrete elements

was achieved by reaching an average strain value of 0.00466, as shown in Figure 5-93.

Figure 5-94 shows the predicted crack pattern of BM10H where the beam exhibited

sequential cracking, similar to the CB model. Therefore, the incorporation of bolts as

an anchorage system allowed the beam to gain stiffness and ductility while still demonstrating crushing, similar to a typical RC beam. Refer to Appendix A through Appendix E to view the contour plots and crack patterns of the rest of the plated specimens in the M10-Specimens group.

```
1
-188.647
-158.015
-127.382 End of Plate.
-96.7499
-66.1175
-35.485 MX
-4.85258
25.7799
56.4123
87.0447 MN
```

Figure 5-92: Predicted nodal shear stress for BM10H model.

5.7.3. BEM12E. The last FE model selected was the BEM12E model from the M12-Specimens group. Figure 5-95 shows the predicted nodal deflection contour plots where it can be observed that the model demonstrated an intermediate debonding

```
115
1
-.041943
-.037283
-.032622
-.027962
-.023302
-.018641
MX
-.013981
MN
-.009321
1 -.00466
```

```
CRACKS AND CRUSHING
STEP=.23705E-08 MAR 23 2019
SUB =24 20:06:29
TIME=32.757
```

Figure 5-93: Predicted nodal third principal strain for BM10H model.

Figure 5-94: Predicted crack patterns of the BM10H model. failure, similar to the experimental failure mode. Furthermore, the 1st principal stress

contour plot of the bolted AA plate was extracted as shown in Figure 5-96 where the

maximum tensile stress occurred throughout most of the moment region, approximately 425 mm from the mid-span of the beam, followed by a decay in the tensile stress until the edge of the plate. Moreover, the bolts in this model were subjected to less tensile stress than that of the BM10H model due to the tensile stress distribution along the surface area of both the epoxy and the bolts, respectively. Figure 5-97 shows the shear stress in the X-Z plane of the bolts where the maximum shear stress also took place in the bolt at a value of 54.5 MPa, 37.4% less than the shear stress in the bolts of the BM10H model. Also, the maximum shear stress only occurred at the first bolt from the edge of the plate, unlike the BM10H model. Therefore, the presence of epoxy reduced the shearing effect in the bolts. The concrete elements also reached the ultimate cylindrical compressive stress in which the average strain reached a value of -0.00596 when observing the 3rd principal strain contour plot shown in Figure 5-98. Finally, the crack pattern of the BEM12E model was generated, as shown in Figure 5-94, where the beam exhibited sequential cracking, similar to the

116

1

-19.2328

-16.9347

-14.6366

-12.3385

-10.0404

-7.74233

MX

-5.44423

-3.14613 MN

-.848037 End-Debonding action

1.45006 1

-19.2328

-16.9347

-14.6366

-12.3385

-1 0. 04 04

-7.74233

MN

-5.44423

-3.14613

1 -.848037

Figure 5-95: Predicted nodal vertical deflection for BEM12E model.

.198047

17.804

35.41  
53.0159  
MN  
70.6219  
MX  
88.2278  
105.834  
123.44  
141.046  
Tensile Stress Contribution (L  
158.652 eff).

Figure 5-96: Predicted nodal first principal stress for BEM12E model.  
CB model. Refer to Appendix A through Appendix E to view the contour  
plots and crack patterns for the rest of the specimens in the M12-Specimens group.

117  
1  
-108.484  
-90.3735  
MXMN End of Plate.  
-72.2628  
-54.152  
-36.0413  
-17.9306  
.18011  
18.2908  
36.4015  
54.5123

1 Figure 5-97: Predicted nodal shear stress for BEM12E model.

-.026808  
-.023829  
-.020851  
-.017872  
-.014893  
-.011915 MX  
-.008936

MN  
-.005957  
1 -.002979  
.172E-10

Figure 5-98: Predicted nodal third principal strain for BEM12E model.

Figure 5-99: Predicted crack patterns of the BEM12E model.

5.7.4. Summary of results. A general summary that includes the  
contribution

of the plates (L), shear stress  
in bolt eff, Tts ( $\tau$  max, bolts) and failure  
modes, as shown in

118

Table 5-26. It can be observed, from the presented cases, that the specimens with edge anchors have proven to utilize most of their AA plate's length during bending by treating their anchors as longitudinal restraints and preventing the plate from buckling. This phenomenon granted the specimens the ability to maintain a constant lever arm throughout the beams' spans and resist the large and constant moment regions. The maximum shear stress concentration occurring within the bolts were mitigated by increasing diameter and number of the bolts while bonding by means of using adhesives, epoxy, when anchoring the plate. However, it was observed that the bonding agent has proven to be more effective in reducing the shear stress accumulation in the bolts than alternating the size and number of the bolts. This was observed when viewing specimens BM10H and BM12H where the maximum shear stress occurring within the bolts were 87 MPa, respectively. Therefore, by combining both bolts and epoxy, the structural engineer can make use of the AA plates' mechanical properties when performing external strengthening applications and obtain a section that is stiffer and more ductile than its previous state. In addition, the failure modes were reproduced by observing the predicted stress and strain contour plots provided by ANSYS. CBE, BEM10E and BEM12E exhibited CC plus ED and ID by reaching the third principal and shear stresses within the previously established range. The rest of the models exhibited CC and PR failure modes since the first principal stress and third principal strain were within the range discussed the failure criteria section.

Table 5-26: Summary of stress contour plots.

Model	Length (mm)	Maximum Shear Stress (MPa)	Third Principal Stress (MPa)	FE Effect	Strain (mm/mm)	Failure Mode
CBE	250	N/A	123.8	-0.00244	5.95	ED
BEM10H	100	15.2	242.5	0.00391	3.45	CC+PR
BEM10L	200	18.8	261.5	-0.00430	3.31	CC+PR
BM10H	200	87.04	241.3	-0.00466	-	CC+PR
BEM10E	425	17.2	141.3	-0.00432	6.1	CC+ID
BEM12H	100	10.4	229.8	-0.00444	4.12	CC+PR
BEM12L	200	16.13	259.4	-0.00423	4.36	CC+PR
BM12H	200	87	188	-0.00439	-	CC+PR
BEM12E	425	36	158.6	-0.00465	6.04	CC+ID

119

This study investigated the effect of bolting and/or bonding of AA plates to the soffits of RC beams on their stiffness, ductility and failure modes. Several experimental parameters were considered; namely, bolt size, embedment depth and spacing. Test results which include: strain in concrete, steel and AA plate with load and deflection values that were recorded during testing. In addition, failure modes were captured. The study was divided into two phases; namely, the experimental part, which was conducted on the prepared specimens, and the FE part, which primarily focused on developing and validating FE models using the experimental results. From the experimental investigation, the following conclusions can be drawn:

1. A bi-linear profile was observed in the plated specimens—due to the presence of two different reinforcing materials; steel and the AA plate.
2. The incorporation of AA plates in flexural strengthening applications has proven to increase the loading capacity when compared to the un-strengthened beam.
3. Using bolts has effectively negated any premature failure modes and promoted ductility, of which, some specimens demonstrated larger ductility than that of a typical RC beam.
4. The effect of increasing torque magnitudes when fixing epoxy-bonded plates to RC beams granted the beams ideal load transfer such that the plated specimens exhibited stiffer behavior during the test.
5. Larger strength enhancements were demonstrated for the specimens which included both epoxy and bolts.
6. End-plate anchorage granted the plated specimens larger ductility than plated specimens that were uniformly anchored along the span of the beams.
7. The plated specimens that were anchored uniformly, despite the presence of epoxy, have exhibited plate rupture, whereas end-plated specimens demonstrated intermediate plate-debonding.

120

From the FE models, the following conclusions can be drawn:

1. The FE models produced results that correlated well with the results obtained from the experiment.
2. FE modelling could be executed as an alternative to experimental work in which unique and complicated strengthening configurations can be designed and pro-

posed to the clients.

3. The peak load and deflection value predicted by the FE models showed minimal percentage differences, less than 10%, when compared to the peak load and deflection values obtained from the experiment.

4. Bond-slip models can be employed into the FE environment such that debonding-related failures can be reproduced and simulated for externally strengthened specimens.

5. The number and size of anchors is inversely proportional to the shear stress concentration within the bolts.

6. The implementation of bolting uniformly along the length of the plate reduces the effective length in which the tensile stress acts along.

7. End-plate bolting combined with epoxy-bonding demonstrated the most efficient

section in terms of both stiffness and ductility.

121

## References

[1] STRUCTURES+BUILDINGS. "Keys to Success: Structural Repair and Strengthening Techniques for Concrete Facilities". Internet. [Online]. Available:

<https://csengineermag.com> [Accessed: May 15, 2018].

[2] American Society of Civil Engineers, Minimum Design Loads and Associated

Criteria for Buildings and Other Structures (7-16). ASCE, 2017.

[3] A. M. Mirghani, J. A. Abdalla, and R. A. Hawileh, "Modeling and Simulation of

Bond-Slip Behavior of Aluminum Alloy plates Adhesively Bonded to Concrete,"

in 2017 7th Int. Conf. Modeling, Simulation, and Applied Optimization (ICMSAO),

April 2017, pp. 1-5.

[4] H. Saadatmanesh and M. R. Ehsani, "RC Beams Strengthened with GFRP Plates

I: Experimental Study," Journal of Structural Engineering, vol. 117, no. 11, pp.

3417-3433, 1991.

[5] K. M. Mohamed, J. A. Abdalla, R. A. Hawileh, and W. Nawaz, "Using bore-

epoxy anchorage to delay debonding of cfrp plates strengthened concrete beams,"

in 2018 Advances in Science and Engineering Technology Int. Conf. (ASET), Feb

2018, pp. 1-5.

[6] BASF. "Master Builders Solutions". Internet. [Online]. Available:

<https://www.master-builders-solutions.basf.ae/en-mne> [Accessed: May 18, 2018].

- [7] Structural. "A Structural Group Company". Internet. [Online]. Available: <https://www.structural-me.com/about-structural-middle-east> [Accessed: May 24, 2018].
- [8] R. Kalfat and S. T. Smith, "Anchorage Devices Used to Improve the Performance of Reinforced Concrete Beams Retrofitted with FRP Composites : State-of-the-Art Review," *Journal of Composites for Construction*, vol. 17, no. 1, pp. 14-33, 2013.
- [9] G. M. Chen, J. G. Teng, and J. F. Chen, "Shear Strength Model for FRP-Strengthened RC Beams with Adverse FRP-Steel Interaction," *Journal of Composites for Construction*, vol. 17, no. 1, pp. 50-66, 2013.
- [10] H. A. Rasheed, J. Abdalla, R. Hawileh, and A. K. Al-Tamimi, "Flexural behavior of reinforced concrete beams strengthened with externally bonded aluminum alloy plates," *Engineering Structures*, vol. 147, no. 15, pp. 473-485, 2017.
- [11] J. A. Abdalla, A. S. Abu-Obeidah, R. A. Hawileh, and H. A. Rasheed, "Shear Strengthening of Reinforced Concrete Beams using Externally-bonded Aluminum Alloy Plates: An Experimental Study," *Construction and Building Materials*, vol. 128, no. 15, pp. 24-37, 2016.
- [12] R. Hawileh, W. Nawaz, J. Abdalla, and E. Saqan, "Effect of flexural CFRP sheets on shear resistance of reinforced concrete beams," *Composite Structures*, vol. 122, pp. 468-476, 2015.
- [13] R. A. Hawileh, H. A. Rasheed, J. A. Abdalla, and A. K. Al-Tamimi, "Behavior of reinforced concrete beams strengthened with externally bonded hybrid fiber reinforced polymer systems," *Materials and Design*, vol. 53, pp. 972-982, 2014.
- [14] O. B. Hwan, J. Y. Cho, and D. G. Park, "Failure Behavior and Separation Criterion for Strengthened Concrete Members with Steel Plates," *Journal of Structural Engineering*, vol. 129, no. 9, pp. 1191-1198, 2003.
- [15] M. Hussain, A. Sharif, I. A. Basunbul, M. H. Baluch, and G. J. Al-Sulaimani, "Flexural Behavior of Precracked Reinforced Concrete Beams Strengthened Externally by Steel Plates," *Structural Journal*, vol. 92, no. 1, pp. 14-23.
- [16] S. Aykac, I. Kalkan, B. Aykac, and S. Karahan, "Strengthening and Repair of



- Reinforced Concrete Beams Using External Steel Plates," *Journal of Structural Engineering*, vol. 139, no. 6, pp. 929-939, 2013.
- [17] N. Attari, S. Amziane, and M. Chemrouk, "Flexural Strengthening of Concrete Beams using CFRP, GFRP and Hybrid FRP Sheets," *Construction and Building Materials*, vol. 37, pp. 746-757, 2012.
- [18] R. Gao, Q. Cao, F. Hu, Z. Gao, and F. Li, "Experimental Study on Flexural Performance of Reinforced Concrete Beams Subjected to Different Plate Strengthening," *Composite Structures*, vol. 176, no. 15, pp. 565-581, 2017.
- [19] R. Kotynia, H. A. Baky, K. W. Neale, and U. A. Ebead, "Flexural Strengthening of RC Beams with Externally Bonded CFRP Systems: Test Results and 3D Non-linear FE Analysis," *Journal of Composites for Construction*, vol. 12, no. 2, pp. 190-201, 2008.
- [20] J. A. Abdalla, R. A. Hawileh, W. Nawaz, and A. Mohammed, "Reinforced concrete beams externally strengthened in flexure using hybrid systems," in *2018 Advances in Science and Engineering Technology Int. Conf. (ASET)*, 2018, pp. 1-5.
- [21] E. C. Karam, R. A. Hawileh, T. E. Maaddawy, and J. A. Abdalla, "Experimental investigations of repair of pre-damaged steel-concrete composite beams using CFRP laminates and mechanical anchors," *Thin-Walled Structures*, vol. 112, pp. 107-117, 2017.
- [22] A. Salama, R. Hawileh, and J. Abdalla, "Performance of externally strengthened RC beams with side-bonded CFRP sheets," *Composite Structures*, vol. 212, pp. 281-290, 2019.
- [23] P. Saxena, H. Toutanji, and A. Noumowe, "Failure Analysis of FRP-Strengthened RC Beams," *Journal of Composites for Construction*, vol. 12, no. 2, pp. 2-14, 2008.
- [24] B. Fu, X. Tang, L. Li, F. Liu, and G. Lin, "Inclined FRP U-jackets for enhancing structural performance of FRP-plated RC beams suffering from IC debonding," *Composite Structures*, vol. 200, no. 15, pp. 36-46, 2018.
- [25] B. Yalim, A. S. Kalayci, and A. Mirmiran, "Performance of FRP-Strengthened RC Beams with Different Concrete Surface Profiles," *Journal of Composites for Construction*, vol. 12, no. 6, pp. 626-634, 2008.
- [26] S. V. Grelle and L. H. Sneed, "Review of Anchorage Systems for Externally

Bonded FRP Laminates," International Journal of Concrete Structures and Materials, vol. 7, no. 1, pp. 17-33, 2013.

[27] R. Hawileh, A. Salameh, and J. A. Abdalla, "Strengthening of reinforced concrete beams in flexure with side-bonded CFRP laminates," in Proc. 5th Int. Conf. Durability Fiber Reinforced Polymer (FRP) Composites for Construction and Rehabilitation Structures (CDCC 2017), Sherbrooke, Canada, July 2017, pp. 1-5.

[28] F. Ceroni, M. Pecce, S. Matthys, and L. Taerwe, "Debonding strength and anchorage devices for reinforced concrete elements strengthened with FRP sheets," Composites Part B: Engineering, vol. 39, no. 3, pp. 429-441, 2008.

[29] L. C. Bank and D. Arora, "Analysis of RC Beams Strengthened with Mechanically Fastened FRP (MF-FRP) Strips," Composite Structures, vol. 79, no. 2, pp. 180-191, 2007.

[30] A. J. Lamanna, D. W. Scott, and L. C. Bank, "Flexural Strengthening of Reinforced Concrete Beams Using Fasteners and Fiber-Reinforced Polymer Strips," Structural Journal, vol. 98, no. 3, pp. 368-376.

[31] A. J. Lamanna, L. C. Bank, and D. W. Scott, "Flexural Strengthening of Reinforced Concrete Beams by Mechanically Attaching Fiber-Reinforced Polymer Strips," Journal of Composites for Construction, vol. 8, no. 3, pp. 203-210, 2004.

[32] C. N. Rosner and S. H. Rizkalla, "Bolted Connections for Fiber-Reinforced Composite Structural Members: Experimental Program," Journal of Materials in Civil Engineering, vol. 7, no. 4, pp. 223-231, 1995.

[33] C. G. Papanicolaou, T. C. Triantafyllou, M. Papathanasiou, and K. Karlos, "Textile reinforced mortar (TRM) versus FRP as strengthening material of URM walls: out-of-plane cyclic loading," Materials and Structures, vol. 41, no. 1, pp. 143-157, 2008.

[34] J. A. Abdalla, F. H. Hraib, R. A. Hawileh, and A. M. Mirghani, "Experimental investigation of bond-slip behavior of aluminum plates adhesively bonded to concrete," Journal of Adhesion Science and Technology, vol. 31, no. 1, pp. 82-99, 2017.

[35] J. A. Abdalla, A. Abu-Obeidah, and R. A. Hawileh, "Behaviour of Shear Deficient

Reinforced Concrete Beams with Externally Bonded Aluminum Alloy Plates," in The 2011 World Cong. Advances in Structural Engineering and Mechanics (ASME), Seoul, South Korea, September 2011, pp. 18-23.

[36] A. Abu-Obeidah, R. A. Hawileh, and J. A. Abdalla, "Finite Element Modeling of Shear Deficient Beams Bonded with Aluminum Plates," in Proc. 11th Int. Conf. Computational Structures Technology, Civil-Comp Press, Stirlingshire, UK, September 2012, pp. 4-9.

[37] M. R. Esfahani, M. R. Kianoush, and A. R. Tajari, "Flexural Behaviour of Reinforced Concrete Beams Strengthened by CFRP Sheets," Engineering Structures, vol. 29, no. 10, pp. 2428-2444, 2007.

[38] ACI Committee 440, Guide for the Design and Construction of Externally Bonded FRP Systems for Strengthening Concrete Structures. ACI, 2008.

[39] HILTI. "HILTI Corporation". Internet. [Online]. Available: <https://www.hilti.group/content/hilti/CP/XX/en.html> [Accessed: December 4, 2018].

[40] MAPEI. "Mapei-adhesives, sealants, chemical products for building". Internet. [Online]. Available: <https://www.mapei.com/> [Accessed: January 16, 2019].

[41] ANSYS Academic Research Mechanical, Mechanical APDL Documentation. ANSYS Inc., 2017.

[42] Gulf News. "Dubai, the City of Towers". Internet. [Online]. Available: <https://gulfnews.com/business/property/dubai-the-city-of-towers-1.880098> [Accessed: September 24, 2018].

[43] R. Hawileh, W. Nawaz, J. Abdalla, and E. Saqan, "External Strengthening of Shear Deficient Reinforced Concrete Beams with Flexural CFRP Laminates," in Response Structures under Extreme Loading, Proc. 5th Int. Workshop Performance, Protection and Strengthening Structures under Extreme Loading (PROTECT 2015), East Lansing, Michigan, June 2015, pp. 368-373.

[44] J. K. McKenna and M. A. Erki, "Strengthening of Reinforced Concrete Flexural Members using Externally Applied Steel Plates and Fibre Composite Sheets - A Survey," Canadian Journal of Civil Engineering, vol. 21, no. 1, pp. 16-24, 1994.

[45] B. H. Oh, J. Y. Cho, and D. G. Park, "Static and Fatigue Behavior of Reinforced Concrete Beams Strengthened with Steel Plates for Flexure," Journal of Structural Engineering, vol. 129, no. 4, pp. 527-535, 2003.

[46] R. Swamy, R. Jones, and J. Bloxham, "Structural Behavior of Reinforced Con-

crete Beams Strengthened by Epoxy-Bonded Steel Plates," *The Structural Engineer* (London), vol. 65, no. 2, pp. 59-68, 1987.

[47] H. Rahimi and A. Hutchinson, "Concrete Beams Strengthened with Externally Bonded FRP Plates," *Journal of Composites for Construction*, vol. 5, no. 1, pp. 44-56, 2001.

[48] A. Ashour, S. El-Refaie, and S. Garrity, "Flexural Strengthening of RC Continuous Beams using CFRP Laminates," *Cement and Concrete Composites*, vol. 26, no. 7, pp. 765 - 775, 2004.

[49] H. Saadatmanesh and M. R. Ehsani, "RC Beams Strengthened with GFRP Plates. I: Experimental Study," *Journal of Structural Engineering*, vol. 117, no. 11, pp. 3417-3433, 1991.

[50] H. C. Biscaia, C. Chastre, and M. A. Silva, "A Smeared Crack Analysis of Reinforced Concrete T-beams Strengthened with GFRP Composites," *Engineering Structures*, vol. 56, no. 1, pp. 1346-1361, 2013.

[51] F. Taheri, K. Shahin, and I. Widiarsa, "On the parameters influencing the performance of reinforced concrete beams strengthened with FRP plates," *Composite Structures*, vol. 58, no. 2, pp. 217-226, 2002.

[52] M. Arduini and A. Nanni, "Behavior of Precracked RC Beams Strengthened with Carbon FRP Sheets," *Journal of Composites for Construction*, vol. 1, no. 2, pp. 63-70, 1997.

[53] J. Dong, Q. Wang, and Z. Guan, "Structural Behaviour of RC Beams with External Flexural and Flexural-Shear Strengthening by FRP Sheets," *Composites Part B: Engineering*, vol. 44, no. 1, pp. 604-612, 2013.

[54] A. K. Al-Tamimi, R. Hawileh, J. Abdalla, and H. A. Rasheed, "Effects of Ratio of CFRP Plate Length to Shear Span and End Anchorage on Flexural Behavior of SCC RC Beams," *Journal of Composites for Construction*, vol. 15, no. 6, pp. 908-919, 2011.

[55] T. Norris, H. Saadatmanesh, and M. R. Ehsani, "Shear and Flexural Strengthening of R/C Beams with Carbon Fiber Sheets," *Journal of Structural Engineering*, vol. 123, no. 7, pp. 903-911, 1997.

[56] S. T. Smith and J. G. Teng, "Shear-Bending Interaction in Debonding Failures of FRP-Plated RC Beams," *Advances in Structural Engineering*, vol. 6, no. 3, pp. 183-199, 2003.

[57] H. B. Pham and R. Al-Mahaidi, "Prediction Models for Debonding Failure Loads

of Carbon Fiber Reinforced Polymer Retrofitted Reinforced Concrete Beams," *Journal of Composites for Construction*, vol. 10, no. 1, pp. 48-59, 2006.

[58] R. Al-Amery and R. Al-Mahaidi, "Coupled Flexural-Shear Retrofitting of RC Beams using CFRP Straps," *Composite Structures*, vol. 75, no. 1, pp. 457-464, 2006.

[59] A. A. R. Khan and T. Ayub, "Effectiveness of U-Shaped CFRP Wraps as End Anchorage in Predominant Flexure and Shear Region," in *Advances in FRP Composites in Civil Engineering*, 2011, pp. 533-536.

[60] M. Chellapandian, S. S. Prakash, and A. Sharma, "Experimental and Finite Element Studies on the Flexural Behavior of Reinforced Concrete Elements Strengthened with Hybrid FRP Technique," *Composite Structures*, vol. 208, no. 15, pp. 466-478, 2019.

[61] B. Fu, J. G. Teng, J. F. Chen, G. M. Chen, and Y. C. Guo, "Concrete Cover Separation in FRP-Plated RC Beams: Mitigation Using FRP U-Jackets," *Journal of Composites for Construction*, vol. 21, no. 2, pp. 401-414, 2017.

[62] B. Fu, G. Chen, and J. Teng, "Mitigation of Intermediate Crack Debonding in FRP-Plated RC Beams using FRP U-Jackets," *Composite Structures*, vol. 176, pp. 883-897, 2017.

[63] A. Sharif, I. A. Basunbu, M. H. Baluch, B. N. Ghaleb, and G. J. Al-Sulaimani, "Strengthening of Initially Loaded Reinforced Concrete Beams Using FRP Plates," *Structural Journal*, vol. 91, no. 2, pp. 160-168, 1994.

[64] R. Kalfat, J. Gadd, R. Al-Mahaidi, and S. T. Smith, "An Efficiency Framework for Anchorage Devices used to Enhance the Performance of FRP Strengthened RC Members," *Construction and Building Materials*, vol. 191, no. 10, pp. 354-375, 2018.

[65] A. Ali, J. Abdalla, R. Hawileh, and K. Galal, "CFRP Mechanical Anchorage for Externally Strengthened RC Beams under Flexure," *Physics Procedia*, vol. 55, pp. 10-16, 2014.

[66] N. Eshwar, T. J. Ibell, and A. Nanni, "Effectiveness of CFRP Strengthening on Curved Soffit RC Beams," *Advances in Structural Engineering*, vol. 8, no. 1, pp. 55-68, 2005.

[67] M. Fagone, G. Ranocchiali, C. Caggegi, S. B. Bati, and M. Cuomo, "The Efficiency of Mechanical Anchors in CFRP Strengthening of Masonry: An Experimental

Analysis," Composites Part B: Engineering, vol. 64, no. 1, pp. 1-15, 2014.

[68] F. Ceroni and M. Pecce, "Evaluation of Bond Strength in Concrete Elements Externally Reinforced with CFRP Sheets and Anchoring Devices," Journal of Composites for Construction, vol. 14, no. 5, pp. 521-530, 2010.

[69] H. M. Elbakry and S. M. Allam, "Punching Strengthening of Two-Way Slabs using External Steel Plates," Alexandria Engineering Journal, vol. 54, no. 4, pp. 1207-1218, 2015.

[70] D. J. Oehlers, "Development of Design Rules for Retrofitting by Adhesive Bonding or Bolting Either FRP or Steel plates to RC Beams or Slabs in Bridges and Buildings," Composites Part A: Applied Science and Manufacturing, vol. 32, no. 9, pp. 1345-1355, 2001.

[71] T. A. El-Maaddawy, "Mechanically Fastened Composites for Retrofitting Corrosion-Damaged Reinforced-Concrete Beams: Experimental Investigation," Journal of Composites for Construction, vol. 18, no. 2, pp. 1-14, 2014.

[72] R. Hawileh, J. A. Abdalla, M. Z. Naser, and M. Tanarslan, "Finite Element Modeling of Shear Deficient RC Beams Strengthened with NSM CFRP Rods Under Cyclic Loading," American Concrete Institute (ACI) Special Publication (SP-301): Modeling of FRP Strengthening Techniques in Concrete Infrastructure, vol. 130, pp. 1-18, 2014.

[73] R. A. Hawileh, J. A. Abdalla, and M. Z. Naser, "Modeling the shear strength of concrete beams reinforced with CFRP bars under unsymmetrical loading," Mechanics of Advanced Materials and Structures, vol. 26, no. 3, pp. 1-8, 2018.

[74] R. A. Hawileh, J. A. Abdalla, M. H. Tanarslan, and M. Z. Naser, "Modeling of nonlinear cyclic response of shear-deficient RC T-beams strengthened with side bonded CFRP fabric strips," Computers and Concrete, vol. 8, no. 2, pp. 193-206, 2011.

[75] ACI Committee 318, Building Code Requirements for Structural Concrete and Commentary. ACI, 2014.

[76] ASTM C109/C109M-16a, Standard Test Method for Compressive Strength of Hydraulic Cement Mortars (Using 2-in. or [50-mm] Cube Specimens). West Conshohocken, PA: ASTM International, 2016.

[77] ASTM A370-18, Standard Test Methods and Definitions for Mechanical Testing

- of Steel Products. West Conshohocken, PA: ASTM International, 2018.
- [78] ASTM E8/E8M-16a, Standard Test Methods for Tension Testing of Metallic Materials. West Conshohocken, PA: ASTM International, 2018.
- [79] HILTI, "HST-3 Expansion Anchor Technical Datasheet," HILTI Ltd., Germany, Europe, Tech. Report, 2018.
- [80] MAPEI, "Adesilex PG2 SP Two-Component Thixotropic Epoxy Adhesive for Structural Bonding," Mapei Far East Pte Ltd, Tuas West Road, Singapore, Tech. Report, 2008.
- [81] ACI Committee 546, Concrete Repair Guide. ACI, 2008.
- [82] A. Abu-Obeidah, R. Hawileh, and J. Abdalla, "Finite element analysis of strengthened rc beams in shear with aluminum plates," Computers and Structures, vol. 147, no. 1, pp. 36 - 46, 2015.
- [83] R. Hawileh, "Finite element modeling of reinforced concrete beams with a hybrid combination of steel and aramid reinforcement," Materials and Design (1980-2015), vol. 65, no. 3, pp. 831 - 839, 2015.
- [84] E. Hognestad, N. Hlanson, and D. McHenry, "Concrete Stress Distribution in Ultimate Strength Design," in ACI Journal Proc., vol. 12, 1955, pp. 455-479.
- [85] K. J. Willam and E. D. Warnke, "Constitutive Model for the Triaxial Behavior of Concrete," in Proc. Int. Association for Bridge and Structural Engineering, vol. 19, Bergamo, Italy, 1975, p. 174.
- [86] R. Hawileh, M. Naser, W. Zaidan, and H. Rasheed, "Modeling of insulated CFRP-strengthened reinforced concrete T-beam exposed to fire," Engineering Structures, vol. 31, no. 12, pp. 3072 - 3079, 2009.
- [87] X. Lu, J. Teng, L. Ye, and J. Jiang, "Bond-slip models for FRP sheets/plates bonded to concrete," Engineering Structures, vol. 27, no. 6, pp. 920-937, 2005.

127

1 Appendix A: Predicted Nodal Vertical Deflection Plots for FE Models

NODAL SOLUTION  
 -17.0011  
 -14.9724  
 -12.9437  
 -10.9151  
 -8.88638  
 -6.85771  
 MX  
 -4.82904  
 MN  
 -2.80037  
 -.771696

1.25698

Figure 6-100: Predicted nodal vertical deflection for CB model.

1NODAL SOLUTION

MAR 23 2019

17:19:15

-18.2191

-16.0467

-13.8742

-11.7018

-9.52936

-7.35692

MX

-5.18448

-3.01204 MN

-.839599

Debonding action

1.33284

1

-18.2191

-16.0467

-13.8742

-1 1.7 01 8-9.52936

-7.35692

-5.18448

-3.01204

-.839599

1.33284

Figure 6-101: Nodal vertical deflection and debonding action for CBE model.

128

1

-36.0044

-31.7207

-27.4369

-23.1531

-18.8693

-14.5856

MX

-10.3018

-6.01803 MN

-1.73426

2.5495

1 Figure 6-102: Predicted nodal vertical deflection for BEM10H model.

-15.9652

-14.0582

-12.1511

-10.2441

-8.33701

-6.42995

MX

-4.52289



-2.61583 MN  
-.708772  
1.19829  
1 Figure 6-103: Predicted nodal vertical deflection for BEM10L model.

-21.536  
-18.9711  
-16.4062  
-13.8414  
-11.2765  
-8.71159  
MX  
-6.14671  
-3.58183 MN  
-1.01695  
1.54794

Figure 6-104: Predicted nodal vertical deflection for BM10H model.

129  
1

-14.9947  
-13.2047  
-11.4146  
-9.62462  
-7.83459  
-6.04456  
MX  
-4.25453  
-2.4645 MN  
-.674469  
End-Debonding Action  
1.11556

1  
-14.9947  
-13.2047  
-11.4146  
-9.62462  
-7.83459

4.2 445545 63  
-2.4645  
-.674469  
1.11556  
MN

Figure 6-105: Predicted nodal vertical deflection for BEM10E model.

1NODAL SOLUTION  
-18.7055  
-16.4727  
-14.2399  
-12.0071  
-9.7743  
-7.5415

MX  
-5.30871  
-3.07592 MN  
-.843134  
1.38966

Figure 6-106: Predicted nodal vertical deflection for BEM12H model.

130  
1  
-15.6703  
-13.7985  
-11.9267  
-10.0549  
-8.18306  
-6.31125

MX  
-4.43943  
-2.56762 MN  
-.695807  
1.17601

Figure 6-107: Predicted nodal vertical deflection for BEM12L model.

1  
-18.8871  
-16.6339  
-14.3808  
-12.1277  
-9.87456  
-7.62143

MX  
-5.3683  
-3.11518 MN  
-.862049  
1.39108

Figure 6-108: Predicted nodal vertical deflection for BM12H model.

131  
1  
-19.2328  
-16.9347  
-14.6366  
-12.3385  
-10.0404  
-7.74233

MX  
-5.44423  
-3.14613 MN  
-.848037 End-Debonding action  
1.45006 1  
-19.2328  
-16.9347  
-14.6366  
-12.3385

-7.74233

MN

-5.44423

-3.14613

-.848037

Figure 6-109: Predicted nodal vertical deflection for BEM12E model.

132

1 Appendix B: Predicted Nodal First Principal Stress Plots for FE Models

2.15879 MN

15.6778

29.1968

42.7158

56.2348

69.7538

83.2728

96.7918

MX

110.311

Tensile Stress Contribution.

123.83

Figure 6-110: Predicted nodal first principal stress for CBE model.

1

.151591

27.084

54.0164

80.9488 MN

107.881

134.814

161.746

188.678

215.611

242.543

Stress Concentration at Bolt Locations (Leff). MX

Figure 6-111: Predicted nodal first principal stress for BEM10H model.

133

1

-2.08176

27.1799

56.4415

85.7031

114.965

144.226

173.488

202.75 MN

232.011

261.273

MX

Tensile Stress Contribution (Leff).

Figure 6-112: Predicted nodal first principal stress for BEM10L model.

1

-22.301

43.7075 MMNX  
109.716  
175.725  
241.733  
307.742  
373.75  
439.759  
505.767

Stress Concentration at Bolt Locations (Leff). 571.776

Figure 6-113: Predicted nodal first principal stress for BM10H model.

134

1

.489059  
19.0298  
37.5705  
56.1113

MN

74.652

MX

93.1927  
111.733  
130.274  
148.815

Tensile Stress Contribution (Leff).

167.356

Figure 6-114: Predicted nodal first principal stress for BEM10E model.

1

-.706491  
24.9029  
50.5123  
76.1217

101.731

127.34

152.95

178.559 MN

204.169

229.778

Stress Concentration at Bolt Locations (Leff). MX

Figure 6-115: Predicted nodal first principal stress for BEM12H model.

135

1

-.568747

28.3222

MN

57.2131

86.104

114.995

143.886

172.777

201.668

230.559

259.449

MX

Stress Concentration at Bolt Locations (Leff).

Figure 6-116: Predicted nodal first principal stress for BEM12L model.

1

-17.1999

34.3048 MX

MN

85.8096

137.314

188.819

240.324

291.828

343.333

394.838

446.343 Stress Concentration at Bolt Locations (Leff).

Figure 6-117: Predicted nodal first principal stress for BEM12H model.

136

1

.198047

17.804

35.41

53.0159

MN

70.6219

MX

88.2278

105.834

123.44

141.046

Tensile Stress Contribution (L

158.652 eff).

Figure 6-118: Predicted nodal first principal stress for BEM12E model.

137

Appendix C: Predicted Nodal Shear Stress Plots in Bolts

1

-221.51

-174.17

End of Plate.

-126.829

-79.4891

-32.1489

15.1913

62.5316

109.872

157.212

204.552

Figure 6-119: Predicted nodal shear stress plots in bolts for BEM10H model.

1

-255.801

End of Plate

-200.878

-145.955

-91.0321

-36.109  
18.814  
73.7371  
128.66  
183.583  
238.506 MX

Figure 6-120: Predicted nodal shear stress plots in bolts for BEM10L model.

138  
1  
-188.647  
-158.015  
-127.382 End of Plate.  
-96.7499  
-66.1175  
-35.485 MX  
-4.85258  
25.7799  
56.4123  
87.0447 MN

Figure 6-121: Predicted nodal shear stress plots in bolts for BM10H model.

1  
MN  
-116.814  
-94.4724  
-72.131  
End of Plate.  
-49.7896  
-27.4482  
-5.10681  
17.2346  
39.576  
61.9174  
MX  
84.2588

Figure 6-122: Predicted nodal shear stress plots in bolts for BEM10E model.

139  
1  
-195.007  
-153.949  
End of Plate.  
-112.89  
-71.8318  
-30.7734  
10.285  
51.3434  
92.4018

133.46  
174.519

Figure 6-123: Predicted nodal shear stress plots in bolts for BEM12H model.

1  
-254.658  
-200.499  
-146.339 End of Plate.  
-92.1799  
-38.0204  
16.1391  
70.2985  
124.458  
178.617  
232.777  
MX

Figure 6-124: Predicted nodal shear stress plots in bolts for BEM12L model.

140  
1  
-188.647  
End of Plate  
-158.015  
-127.382  
-96.7499  
MX  
-66.1175  
-35.485  
-4.85258  
MN  
25.7799  
56.4123  
87.0447

Figure 6-125: Predicted nodal shear stress plots in bolts for BM12H model.

1  
-108.484  
-90.3735  
MXMN End of Plate.  
-72.2628  
-54.152  
-36.0413  
-17.9306  
.18011  
18.2908  
36.4015  
54.5123

Figure 6-126: Predicted nodal shear stress plots in bolts for BEM12E model.

141

Appendix D: Predicted Nodal Third Principal Strain for FE Models

-.006034

-.005363

-.004693

-.004023

MX

-.003352

-.002682

MN

-.002011

-.001341

-.670E-03

.292E-09

Figure 6-127: Predicted nodal third principal strain for CB model.

1

-.0044

-.003911

-.003422

-.002933 MN

-.002444

-.001955

MX

-.001467

-.978E-03

-.489E-03

.301E-08

Figure 6-128: Predicted nodal third principal strain for CBE model.

142

1

-.020845

-.018529

-.016213

-.013897

-.011581

-.009265

MX

-.006948

-.004632 MN

-.002316

.264E-08

Figure 6-129: Predicted nodal third principal strain for BEM10H model.

-.0155

-.013778

-.012056

-.010333

-.008611



-.006889 MX  
-.005167  
MN  
-.003444  
-.001722  
.283E-08  
1

Figure 6-130: Predicted nodal third principal strain for BEM10L model.

-.041943  
-.037283  
-.032622  
-.027962  
-.023302  
-.018641

MX  
-.013981  
MN  
-.009321  
-.00466  
.275E-08

Figure 6-131: Predicted nodal third principal strain for BM10H model.

143  
1  
-.015553  
-.013825  
-.012097  
-.010369  
-.00864  
-.006912

MX  
-.005184  
MN  
-.003456  
-.001728  
.280E-08

Figure 6-132: Predicted nodal third principal strain for BEM10E model.

-.019998  
-.017776  
-.015554  
-.013332  
-.01111  
-.008888

MX  
-.006666  
-.004444 MN  
-.002222  
.281E-08

1 Figure 6-133: Predicted nodal third principal strain for BEM12H model.

-.038062  
-.033833  
-.029604  
-.025375  
-.021146  
-.016916  
MX  
-.012687  
MN  
-.008458  
-.004229  
.260E-08

Figure 6-134: Predicted nodal third principal strain for BEM12L model.

144  
1  
-.026348  
-.02342  
-.020493  
-.017565  
-.014638  
-.01171  
MX  
-.008783  
MN  
-.005855  
-.002928  
.237E-08

Figure 6-135: Predicted nodal third principal strain for BM12H model.

1  
-.026808  
-.023829  
-.020851  
-.017872  
-.014893  
-.011915 MX  
-.008936  
MN  
-.005957  
-.002979  
.172E-10

Figure 6-136: Predicted nodal third principal strain for BEM12E model.

145  
1 Appendix E: Predicted Crack Pattern for FE Models  
CRACKS AND CRUSHING  
STEP=14  
SUB =24 The appendix could include copies of surveys, experimental  
results, software  
TIME=14.1988

programs, data and other supporting information.

1

CRACKS AND CRUSHING

STEP=30 Figure 6-137: Predicted crack patterns of the CB model. MAR 23 2019

SUB =24 20:02:28

TIME=14.8512

1

Figure 6-138: Predicted crack patterns of the CBE model.

Figure 6-139: Predicted crack patterns of the BEM10H model.

146

1

1

CRACKS AND CRUSHING

STEP=30 MAR 23 201 9

SUB =24 20:06:29

TIME=32.757

Figure 6-140: Predicted crack patterns of the BEM10L model.

1

Figure 6-141: Predicted crack patterns of the BM10H model.

1

Figure 6-142: Predicted crack patterns of the BEM10E model.

1

Figure 6-143: Predicted crack patterns of the BEM12H model.

Figure 6-144: Predicted crack patterns of the BEM12L model.

147

1

Figure 6-145: Predicted crack patterns of the BM12H model.

1

Figure 6-146: Predicted crack patterns of the BEM12E model.

148

Vita

Omar Raed Abuodeh was born in 1994, in Pocatello, Idaho, in the United States

of America. In 2001, he moved to the United Arab Emirates where he studied for 12 years in Dubai International School and graduated fifth amongst his classmates. Afterwards, Mr. Abuodeh pursued a Bachelors degree in Civil and Environmental Engineering from the University of Sharjah, where he partook in various academic competitions and resarch projects and graduated with a CGPA of 3.55 in June 2016.